October 2018

MEASURED CAPILLARY FORCES ON SPHERES AT LIQUID INTERFACES AND THE MECHANICS OF INTERFACIAL PARTICULATE ASSEMBLIES

Wei He

MEASURED CAPILLARY FORCES ON SPHERES AT LIQUID INTERFACES AND THE MECHANICS OF INTERFACIAL PARTICULATE ASSEMBLIES

A Dissertation will be Presented

by

WEI HE

Submitted to the Graduate School of the
University of Massachusetts Amherst in partial fulfillment
of the requirement for the degree of

DOCTOR OF PHILOSOPHY

September 2018

Department of Physics

MEASURED CAPILLARY FORCES ON SPHERES AT LIQUID INTERFACES AND THE MECHANICS OF INTERFACIAL PARTICULATE ASSEMBLIES

A Dissertation Presented

by

WEI HE

Approved as to style and content by:

_____
Anthony D. Dinsmore, Chair

_____
Benny Davidovitch, Member

_____
Gregory M. Grason, Member

_____
Menon Narayanan, Member

_____
Menon Narayanan, Department Head

ACKNOWLEDGEMENTS

This dissertation would not have been possible without the consistent advice and support of many people. First and foremost, I would like to extend great gratitude to my advisor, Professor Anthony D. Dinsmore for his constant encouragement and patient instruction throughout my Ph. D. years. I was fortunate enough to have the chance to work with him, and I am grateful for all the things that I have learned from him. No less appreciation goes to my committee members, Professor Benny Davidovitch, Professor Gregory Grason and Professor Narayanan Menon. I would like to express my thanks to them for their valuable contributions on my research.

I sincerely acknowledge the close collaboration with the research group of Professor S. Thai Thayumanavan. I am grateful for his suggestions and feedback on the project. Also the stimulating discussions with Thameez Mohammad Koyasseril Yehiya and Ziwen Jiang are deeply appreciated.

I would also like to acknowledge all the members in Dinsmore Research Group for all formal and informal discussions on various of topics, which make our work fun and fruitful together. I also greatly appreciate the support provided by Physics Department.

Finally, I would like to thank my family and friends for their unconditional support. This journey would not be possible without them.

ABSTRACT

MEASURED CAPILLARY FORCES ON SPHERES AT LIQUID INTERFACES AND THE MECHANICS OF INTERFACIAL PARTICULATE ASSEMBLIES

SEPTEMBER 2018

WEI HE

B.S. SHANGHAI UNIVERSITY

M.S. UNIVERSITY OF MASSACHUSETTS AMHERST

PH.D. UNIVERSITY OF MASSACHUSETTS AMHERST

Directed by: Professor Anthony D. Dinsmore

Particle-laden interfaces have promising potentials in many fields because the particulate nature can endow the surface with physical properties that are not readily obtained from molecular-scale surfactants. In this dissertation, we first focus on measuring capillary forces on particles at fluid interfaces in order to assess the key parameters that yield effective stabilizing particles. In experiment, the force and the displacement of a millimeter-scale particle passing through a liquid interface were recorded. We find that the peak force needed to detach a particle from an interface crowded with other particles is consistently smaller than the force at a clean interface. By ruling out other possibilities, we attribute the force reduction to the perturbation of interface shape due to the constraints imposed by free particles. Then we study the mechanics of particulate assemblies by measuring the force response under a normal indentation. We find that there exist two linear regions with different slopes. The small-slope regime starts at the beginning and persists over a range of indentations much less than capillary length. Once the system entered the higher plateau region, it has the same stiffness as a pure liquid interface. Further, from top-view

images, we showed that, as long as the indenter was larger than the size of a single particle, the azimuthal compression can be relaxed through the in-plane rearrangement of particles. These features are independent of the difference in fluid mass densities, the radius of the indenter and the species of particles. Although the presence of floating particles at an interface does not change its capillary nature under a wide range of poking depth, we show that the existence of the particle raft makes the original interface tougher in terms of both the maximum force it can sustain and the largest indentation an indenter can reach. These results provide an important step toward understanding the mechanics of particulate assemblies at interfaces.

Finally, we study the formation of organic 2D material in aqueous media for the purpose of potential applications in passivating objects in suspension. We optimized the conditions for the self-assembly of bola-amphiphilic molecules, and directly observed 2D sheets in optical microscope under dark-field illumination. We find that stacking is not preferred by sheets because of the likely electrostatic repulsion. Our method provides an effective way to better understand the properties of those sheets.

TABLE OF CONTENTS

APPENDICES

LIST OF FIGURES

Figure Page

CHAPTER 1

INTRODUCTION

In the past century, a great deal of attention has been focused on particles at the interface of two immiscible liquids or a liquid and air [1-5]. By adsorbing particles onto the interface, the free energy of the system is reduced through the change of surface energy [6]. The resulting particle-laden interfaces occur naturally and are widely used in many fields ranging from fundamental science to engineering applications [7-10]. This makes it important to understand the adsorption, structure and mechanical properties of particles at liquid interfaces.

In this dissertation, we discuss capillary forces on particles at fluid interfaces, the mechanics of the interfacial monolayer and the formation of two dimensional structure via the self-assembly of molecules in water. In the remainder of this chapter, we describe the background information about surface energy, interface shape, capillary forces and intermolecular interactions. This chapter closes with a brief summary of the remaining chapters of the dissertation.

1.1 Contact between three phases

1.1.1 Surface energy

A liquid flows readily with a constant volume, yet it can conform to the shape of its container. In the bulk of a liquid phase, each molecule is subject to the same type of pairwise intermolecular interactions with all its neighbors. However, at the surface of a liquid, due to the exposure to a second phase, those molecules lose some of their cohesion energy, and therefore are not in an favorable state. If the liquid is in equilibrium with its vapor phase, then the associated free energy per unit area is known as the surface tension, γ. If a liquid is in contact

with a second fluid, then the energy per unit area is known as the interfacial tension (also called γ).

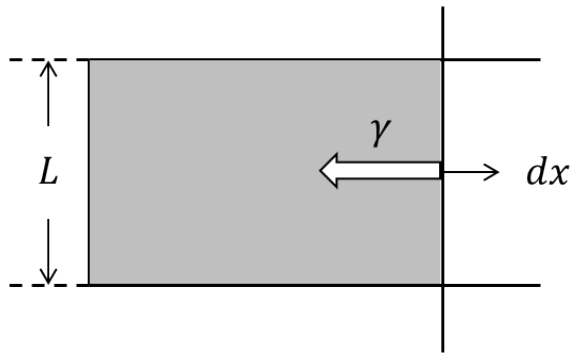

Figure 0.1 Schematic of a rectangular frame with one movable side hold a soap film.

Surface tension can also be interpreted in terms of force per unit length. This force is illustrated in Figure 1.1, a rectangular frame with one movable side is holding a soap film. In order to minimize the total area, the surface tension will pull the movable side to the left, and the work done for a displacement of dx is

$$dw = Fdx = 2\gamma Ldx \quad (1.1)$$

where a factor of 2 is added because the film has two surfaces (both in the plane of the page). Hence γ can be expressed as $F/2L$.

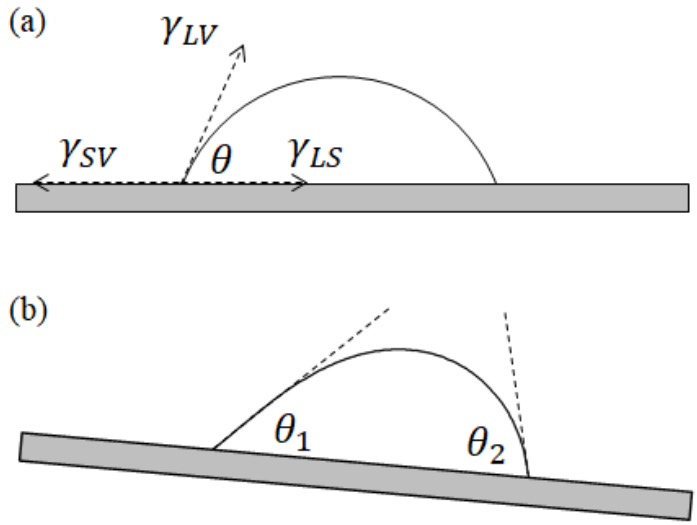

Figure 0.2 (a) Schematic of a liquid droplet sitting on top of a rigid solid substrate. (b) The same droplet sitting on a tilted substrate.

1.1.2 Wetting of a solid surface

Wetting is the ability of a liquid to maintain contact with another surface [11]. Let us first consider the situation, in which the substrate is a rigid solid. The degree of wetting is determined by the competition of adhesive and cohesive intermolecular forces. In the continuum level, however (when the object sizes are much greater than molecular scale), these forces can be described using the interfacial tensions. As shown in Figure 1.2 (a), there are three interfaces we need to consider: liquid-vapor, liquid-solid and solid-vapor interfaces with their corresponding surface tension γ_{LV}, γ_{LS} and γ_{SV}. If $\gamma_{LS} + \gamma_{LV} < \gamma_{SV}$, in order to minimize its surface energy, the liquid would spread to cover as much area as possible. Such a situation is known as total wetting. If $\gamma_{LS} + \gamma_{LV} > \gamma_{SV}$, the liquid droplet remains stuck in a certain area, and is in a partial wetting state. In equilibrium, the force balance at the contact between three phases requires

$$\gamma_{LV} \cos\theta = \gamma_{SV} - \gamma_{LS}. \quad (1.2)$$

The angle θ is called the Young-Dupre contact angle. However, in practice, Young-Dupre contact angle is hardly observed. The measured contact angle (Figure 1.2(b)) can take any value in between the receding and advancing angle, which are defined as the minimum and maximum angle a liquid droplet can achieve on a certain substrate. The difference of the two is known as contact angle hysteresis [12]. Experimentally, the contact angle hysteresis is usually measured by the sessile drop method, in which liquid is pumped into and out of the droplet sitting on a substrate to obtain advancing and receding angles. Apart from sessile drop, tilted plate and Wilhelmy method are also widely used due to their simple realization.

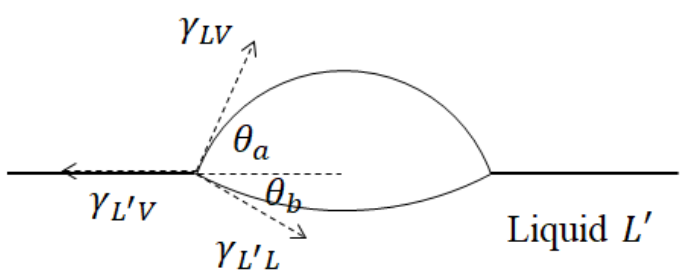

Figure 0.3 Schematic of a liquid droplet sitting on an immiscible liquid substrate.

1.1.3 Wetting of a liquid surface

Now let us make a change to the system discussed in the previous section. We replace the rigid solid substrate with a semi-infinite liquid L', which is immiscible with the droplet. In equilibrium, we have the force balance equations in both horizontal and vertical directions as follows

$$\gamma_{L'V} = \gamma_{LV} \cos\theta_a + \gamma_{L'L} \cos\theta_b, \quad (1.3)$$

$$\gamma_{LV} \sin\theta_a = \gamma_{L'L} \sin\theta_b. \quad (1.4)$$

The emergence of the second equation is due to the fact that the energy cost to deform the substrate is now comparable to the surface energy. In other words, the substrate is deformable under capillary forces. In this situation, if the liquid-vapor surface tensions is known, the rest two are uniquely determined by solving the above equations. However, under the Young-Dupre contact condition for partial wetting of a solid surface, only the difference between γ_{SV} and γ_{LS} is fixed with the extra piece of information on γ_{LV}. The disparity originates from the difference between solid-like and liquid-like bodies.

1.1.4 Curvature of surfaces and Laplace pressure

Perfectly flat surfaces are rarely seen in our daily life. In most cases, surfaces are curved in one way or another. As shown in Figure 1.4, an arbitrary curved surface can be described by two principal curvatures (k_1 and k_2), which are defined as the maximum and minimum curvature at a given point on a surface. The planes in which the two principal curvatures lie are called planes of principal curvatures, which are perpendicular to each other.

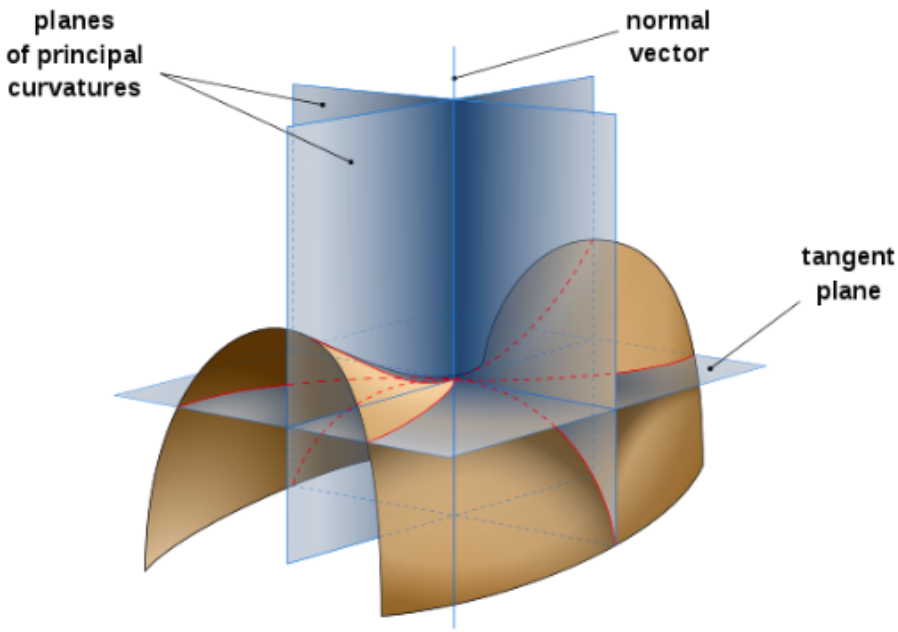

Figure 0.4 Saddle surface with normal planes in directions of principal curvatures. (Image from Wikipedia entry: Gaussian Curvature)

Apart from using k_1 and k_2 directly, curved surfaces are often characterized by different combinations of the two curvatures due to their nice interpretations in discrete world. These combinations include (i) the mean curvature, H, which is defined as the arithmetic mean of two principal curvatures; (ii) the Gaussian curvature, K, which is the square of geometric mean of k_1 and k_2; (iii) the deviatoric curvature, $D = (k_1 - k_2)/2$. For example, a spherical surface with a radius of R has $H = 1/R$, $G = 1/R^2$ and $D = 0$, while a cylindrical surface with the same radius has $H = 1/2R$, $G = 0$ and $D = 1/R$.

From fluid dynamics, we know that in mechanical equilibrium the pressure on the two sides of a perfectly flat surface is the same. However, if the surface is curved, then a discontinuity in pressure, which is induced by the interfacial tension, would appear across the surface. As a simple example, let us consider a spherical droplet with a radius of R. If its surface undergoes an infinitesimal displacement δr, then the work necessary to bring about the change in

volume is $\Delta p \pi R^2 \delta r$, and the energy cost associates with the change of area is $-\gamma 8\pi R \delta r$ to the leading order of δr. Since the condition of equilibrium requires the sum of two equals zero, we have

$$\Delta p = \frac{2\gamma}{R}. \quad (1.5)$$

More generally, the relation between the pressure difference and the shape of interface is described by the Young-Laplace equation

$$\Delta p = 2\gamma H. \quad (1.6)$$

In Cartesian coordinates, the mean curvature, H, can be written as

$$2H = \nabla \cdot \frac{\nabla z(x,y)}{\sqrt{1 + |\nabla z(x,y)|^2}}, \quad (1.7)$$

where $z(x,y)$ is the out-of-plane deformation. Under the assumption that $|\nabla z(x,y)| \ll 1$, we have the Young-Laplace equation for the quasi-flat interface

$$\frac{\Delta p}{\gamma} = \nabla^2 z(x,y). \quad (1.8)$$

This equation will be used later in this chapter in cases where there is a second contribution to pressure, which is the weight of the fluids. In these cases, the competition between gravity (which prefers planar, level surfaces) and surface energy (which prefers minimal surface area) gives rise to a characteristic length, called the capillary length.

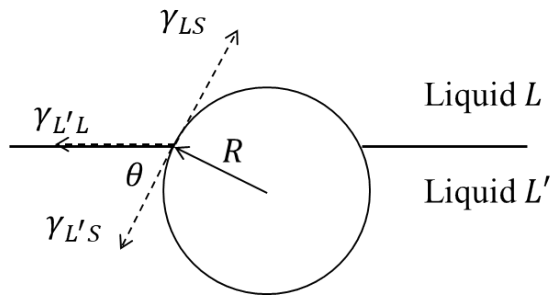

Figure 0.5 A spherical particle sitting in between two liquid phases.

1.2 Particles at liquid interfaces

1.2.1 Particles absorb to interfaces

Particles have a strong affinity for interfaces, because the adsorption of a particle can reduce the total surface energy [6, 8]. Figure 1.5 shows a spherical particle with a radius, R, sitting in between two liquid phases. For the sake of simplicity, we assume the interface is flat around the particle, and along the contact line the Young-Dupre contact angle is maintained. Before reaching the interface, the particle is entirely immersed in liquid L'. In the adsorption process the spherical cap is wetted by the upper liquid L. Hence the change in surface energy is

$$\Delta E = 2\pi R^2(1 - cos\theta)\gamma_{LS} - 2\pi R^2(1 - cos\theta)\gamma_{L'S} - \pi R^2 sin^2\theta\gamma_{L'L}, \quad (1.9)$$

where the first two terms describe the energy cost of being exposed to different liquids; the last term corresponds to the removing of a circular piece of liquid/liquid interface. According to Equation 1.2, we have

$$\gamma_{L'L}\cos\theta = \gamma_{LS} - \gamma_{L'S}. \quad (1.10)$$

By substituting $\gamma_{LS} - \gamma_{L'S}$ with $\gamma_{L'L}\cos\theta$ in Equation 1.7, we get

$$\Delta E = -\pi R^2(1 - cos\theta)^2\gamma_{L'L} < 0. \quad (1.11)$$

Here we emphasize that this equation assumes that the interface was initially planar, that there is no contact-angle hysteresis, and that the interactions between the binding particle and other

particles can be ignored. Later chapters of this dissertation will show that these assumptions are not always correct, and that interactions among multiple particles can have a big effect on the binding energy.

In terms of energy, interfaces always benefit from having particles bind onto it if the particle forms a real, finite contact angle. Apparently, $|\Delta E|$ depends on both contact angle, θ, and the radius of particle, R. They set the energy barrier for the desorption of particles. If the particle has strong preference for either of the two liquid phases or the size of the particle is very small, then the binding will be unstable. For micron-sized particles with a contact angle of $90°$ and a radius of $1\,\mu m$ at water-air interfaces, we have typical values of $|\Delta E| \sim 10^7 kT$; but for nanoparticles, $|\Delta E|$ is comparable to kT [13].

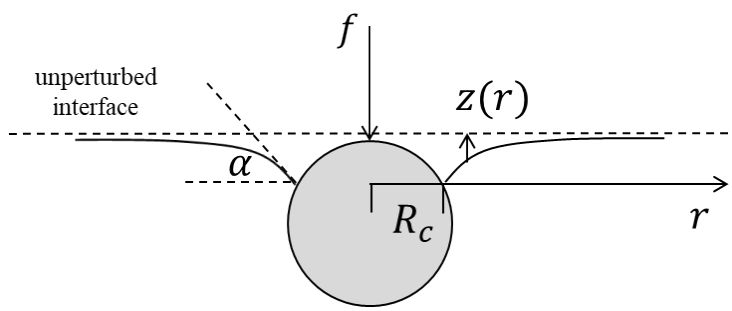

Figure 0.6 A spherical particle deforms the interface around it.

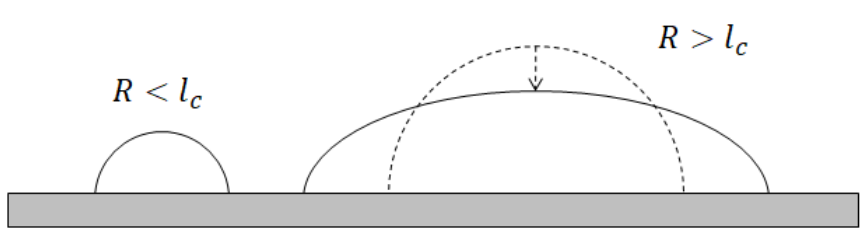

Figure 0.7 Two droplets with different sizes sitting on top of a solid substrate.

More generally, when there exist some external forces, the interface around the particle is no longer flat. As illustrated in Figure 1.6, the interface deforms to balance the vertical force, *f*. In the presence of gravity, the pressure difference across the interface is caused by the density mismatch of the two liquid phases. Rewrite Equation 1.8 in cylindrical coordinates, we have the homogeneous Helmholtz equation that governs the shape of liquid interface

$$\nabla^2 z = \frac{1}{r}\frac{\partial}{\partial r}\left(r\frac{\partial z}{\partial r}\right) + \frac{1}{r^2}\left(\frac{\partial^2 z}{\partial \varphi^2}\right) = \frac{\Delta\rho g z(r)}{\gamma}, \quad (1.12)$$

where $z(r)$ is the distance between the deformed and the unperturbed interfaces. Considering the system has no angle dependence, we have

$$\frac{1}{r}\frac{\partial}{\partial r}\left(r\frac{\partial \mathrm{z}}{\partial r}\right) = \frac{\mathrm{z}}{l_c^2}. \quad (1.13)$$

We further assume that the interface is infinitely large, and the particle is force balanced. These two assumptions naturally lead to the following boundary conditions

$$\mathrm{z}(\infty) = 0 \quad (1.14)$$

$$f = 2\pi R_c \gamma \frac{d\mathrm{z}}{dr}|_{r=R_c} \quad (1.15)$$

Combining Equation 1.13-1.15, we have

$$\mathrm{z}(r) = \frac{f}{2\pi\gamma\frac{R_c}{l_c}}\frac{K_0\left(\frac{r}{l_c}\right)}{K_1\left(\frac{R_c}{l_c}\right)} \quad (1.16)$$

where $K_n(x)$ is the modified Bessel function of second kind. l_c is the capillary length, which is defined as $\sqrt{\gamma/\Delta\rho g}$, where γ is the interfacial tension and Δρ is the density mismatch of the two fluids. It tells us how important the effect of gravity is comparing to that of surface tension. As depicted in Figure 1.7, the droplet on the left side has a radius that is smaller than l_c. Therefore

surface tension dominates, and the droplet maintains a shape of spherical cap which minimized the total area. On the other hand, if the droplet size is larger than l_c, then gravity will play the role of flattening the spherical cap to reduce the potential energy.

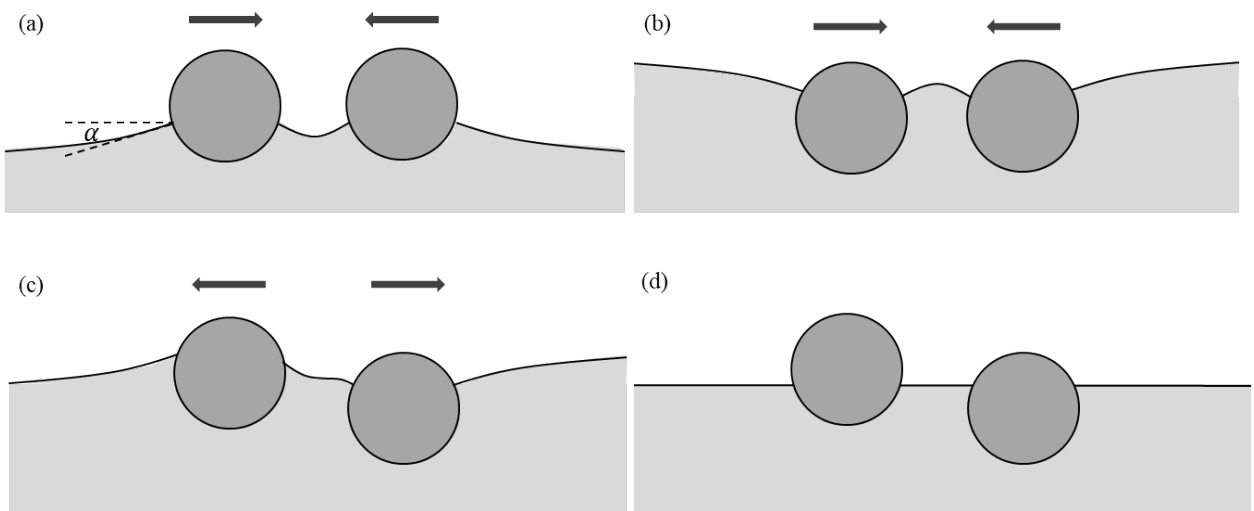

Figure 0.8 The interaction between two spherical particles at interfaces. α is the inclination angle; it is positive for upward meniscus and negative for downward meniscus. (a) (b) Particles that have same type of meniscus attract each other. (b) Particles with different kind of meniscus repel each other. (d) There is no interaction if the interface is flat.

1.2.2 Capillary interactions among particles

It is well known from both scientific experiments and practical experience that floating particles at liquid/liquid or liquid/gas interfaces interact with each other. Those interactions may come from different sources. For example, for charged particles sitting at a flat interface of a polar solvent and a non-polar solvent, the electrostatic force is significant; when the interface is highly curved, the capillarity dominates, and the lateral component of the capillary force drives the motion of particles. In this section, we focus on the capillary interaction, which originates from the deformation of liquid interface around particles. When the distortion of interface produced by different particles overlap, they will either experience an attractive force or a

repulsive one. The sign of the force depends on the shape of meniscus on both particles. To quantify the lateral capillary force among particles, the inclination angle α is introduced to characterize the slope of meniscus at the contact. For upward meniscus, α is positive, while for downward meniscus α is negative. Further, capillary charge of a particle can be defined as

$$Q = r_c sin\alpha. \quad (1.17)$$

According to the theory [14-17], the lateral capillary force between two particles separated by a center-to-center distance L is

$$F = 2\pi\gamma Q_1 Q_2 q K_1(qL), \quad (1.18)$$

where $q = l_c^{-1}$. Q is called capillary charge because the above equation is similar to the Coulomb's law in electrostatics, and Q plays the same role as a point charge. As illustrated in Figure 1.8, if both of the particles have the same type of meniscus around them, then the product of capillary charges is positive, which results in an attractive force. Contrarily, particles with meniscus curved to different directions repel each other.

Apart from gravity and external forces discussed in the previous section, perturbation of the interface shape can also be induced by contact line undulation on the particle, which is due to surface roughness and/or chemical inhomogeneity and/or particle shape. In analogy to the multipole expansion in electrostatics, the undulated contact line can be decomposed into multipole moments, which contribute to the interaction energy independently. Typically, the leading order mode for a micron-sized particles is quadrupole, which corresponds to a deformation of $\cos(2\varphi)$ symmetry, where φ is the azimuthal angle. Recent research shows that for colloidal particles with a spatial separation of several microns, even a deviation on the order

of several tens of nanometer may result in an interaction energy that is on the order of $10^4 kT$ [18, 19].

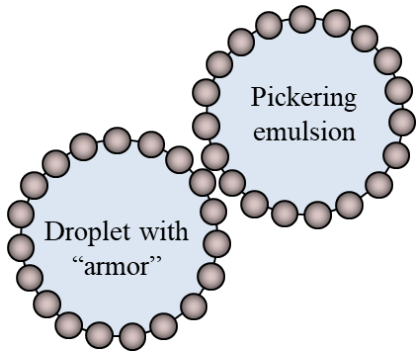

Figure 0.9 Schematic of particle-stabilized droplets, for example oil droplets in water. A suspension of particle-stabilized droplets is called a Pickering emulsion.

1.2.3 Particle-laden interfaces

With the help of attractive forces, particles at interface spontaneously aggregate and form clusters. The resulting particle-laden interfaces are of great importance in many fields ranging from crude oil recovery to drug delivery because the particulate nature can endow the surface with physical properties that are not readily obtained from molecular-scale surfactants [1, 4, 20-22]. A prominent example is the Pickering emulsion, in which small solid particles rather than surfactants are used as emulsifiers. As shown in Figure 1.9, those particles sitting in between the two liquid phases prevent the spontaneous coalescence of droplets. The network of particles offers a mechanical protection for the liquid encapsulated in it.

Depending on the concentration of particles at interface, the surface monolayer exhibits different properties. At low coverage, the system is in the fluid state because it behaves like a viscous liquid characterized by surface tension. As the concentration of interfacial particles increases, in analogy to the glass transition in 3D colloidal suspension, the surface monolayer will also experience a transition from liquid to an elastic soft solid. During the process, more and more constraints are

imposed on the rearrangement of particles, which contributes to the elasticity of the interface. Once the jamming state is reached, the shape of interface may not be easily described by the Young-Laplace equation. In other words, shapes with non-minimal areas can be stabilized by the jamming of particles, which supports anisotropic stresses. If the surface monolayer is further compressed, then out-of-plane deformation can be observed [23-26], and the system is in the buckling state. Since the energy cost to deform hard spheres is much higher than that of bending the particle layer, out-of-plane deformation is a natural solution under high compression. Consequently, the bending rigidity of the interfacial monolayer can be obtained by analyzing the wrinkle patterns [23]. In addition to compression, surface wave propagation is another method to extract bending modulus, in which an oscillating plate is used to generate waves [27]. Due to the presence of particles, the experimental dispersion relation is different from a pure fluid system, and hence the contribution from the interfacial monolayer can be derived by comparing the two. Further, other interesting phenomena, such as the wrinkle-to-fold transition and cascading of wrinkles, have also been observed [26, 28]. They suggest the amazing richness of physics related to the interfacial monolayer.

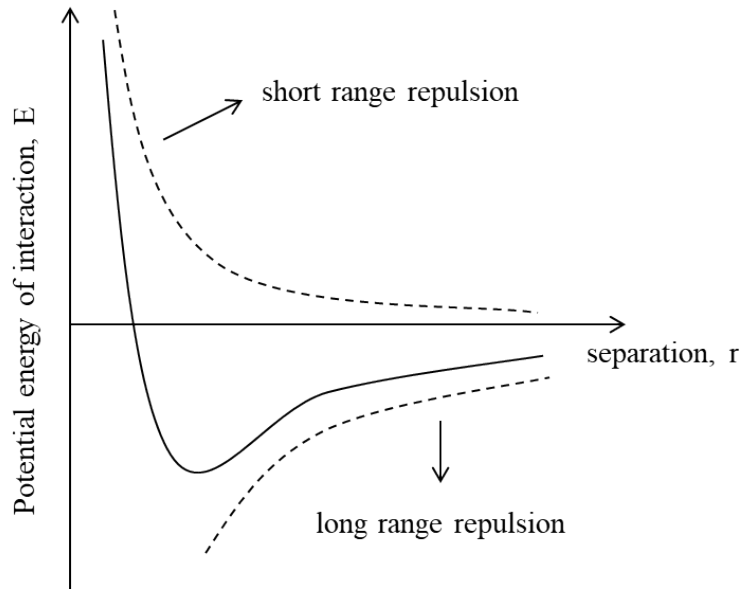

Figure 0.10 Sketch of potential energy between two molecules as a function of their separation.

1.3 Intermolecular forces

Ultra-thin sheets can also bind onto interface, modify interfacial properties, wrap and protect liquids. These sheets can be prepared in large quantity by self-assembly of molecules in suspension, which requires careful control of intermolecular forces. In this section, we introduce basic types of interactions between molecules, and in Chapter 4 more details about the formation of two dimensional material in aqueous media will be discussed.

Intermolecular forces, as indicated by the name itself, are the interactions among neighboring molecules. Although those forces are weaker than intramolecular forces (e. g. ionic bond, covalent bond and metallic bond), they have significant impact on physical properties, such as melting point, evaporation and viscosity, of materials. Generally speaking, the intermolecular ordering is determined by the balance between the long range attraction and the short range repulsion. Figure 1.10 shows a typical curve (solid line) of potential energy, E, as a function of the separation, r, of two molecules. The attractive force dominates for large r. But

when the two molecules get close to each other, the repulsive force increases quickly which counter balance the attractive force. The competing results in an equilibrium distance, at which the minimum potential energy is reached.

Common attractive forces include Van der Waals force, hydrogen bonding interaction, hydrophobic effect and pi-pi stacking. Van der Waals force is the generic name for forces originate from dipole-dipole interactions [29]. A dipole consists of a pair of oppositely charged poles separated by a certain distance. Because of the differences in electronegativity of the atoms, polar molecules can have a net dipole moment in equilibrium. The interaction between such permanent dipoles is known as Keesom force [30]. Different from polar molecules, non-polar molecules do not have permanent dipoles owing to their symmetrical arrangements of polar bonds. However, in the presence of an electrical field, an induced dipole may appear in non-polar molecules due to the rearrangement of electrons. Thus when a polar molecule approaches a non-polar one, it experiences a force (Debye force) coming from the permanent dipole and the induced dipole interaction. Finally, even for two non-polar molecules, there still exists a weak interaction, which is caused by the fluctuation of charge densities. This attractive component is called London or dispersion force [29].

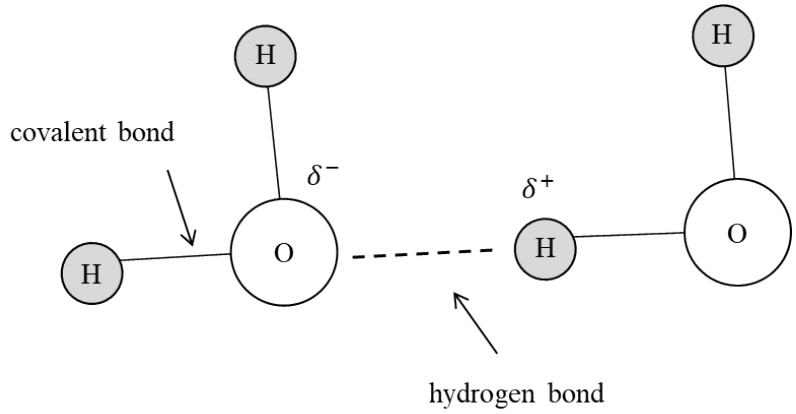

Figure 0.11 Illustration of hydrogen bond.

Hydrogen bonding is another source of attraction among molecules [31]. When a hydrogen atom is covalently bound to a more electronegative atom, it becomes partially positively charged, because the hydrogen nucleus is not strong enough to localize the electron, which also makes the other atom partially negatively charged. Thus adjacent molecules will reorient themselves to allow the formation of bonding between the hydrogen atom and the strongly electronegative atom. Although this type of interaction is call hydrogen bond, it is much weaker than typical chemical bonds. As an example, Figure 1.11 shows the hydrogen bonding interaction between two water molecules. The solid line is the covalent bond, while the dashed line corresponds to the hydrogen bond that links the two molecules.

The hydrophobic effect describes the phenomena that non-polar molecules spontaneously aggregate in aqueous phase [32]. The reason for their low solubility in water is that non-polar molecules cannot participate in hydrogen bonding, and therefore introduce an additional requirement on the ordering of nearby water molecules. Such an additional ordering is entropically unfavorable. In order to minimize the total area exposed to water molecules, attractive forces drive non-polar molecules move towards each other.

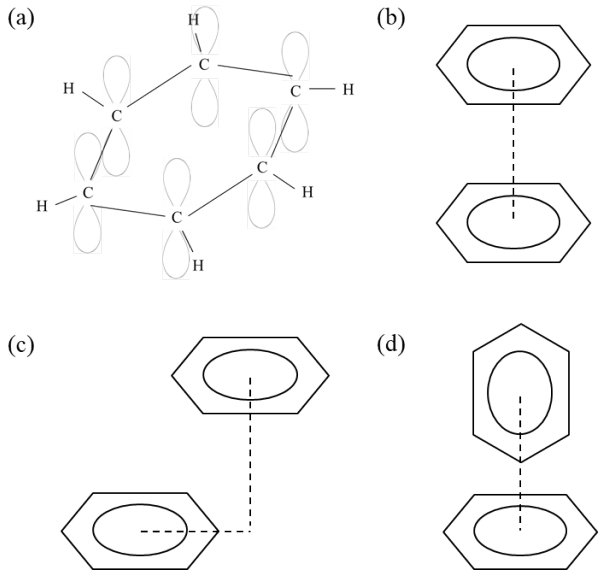

Figure 0.12 (a) Illustration of the structure of an aromatic ring. (b)-(d) Three different stable constructions of two aromatic rings: face-to-face perfect alignment, parallel displaced and T-shaped. (Schematic according to Wikipedia entry: Stacking (chemistry))

π- π stacking is an attractive and non-covalent interaction between aromatic rings. Owing to the side-to-side overlap of p atomic orbitals (Figure 1.12 (a)), the electron rich π systems can interact with each other. There are three stable structures: face-to-face perfect alignment, parallel displaced and T-shaped (Figure 1.12 (b)-(d)). The main energetic contribution comes from both the electrostatic force and the Van der Waals force. Although π- π stacking has been proved to be important in stabilizing complex structures (e. g. long chain helical structures), there is still no unified description of the whole picture of the interaction.

Different from those long range attractive forces, repulsive interactions increase dramatically when molecules are getting closer to each other. In general, there are two types of repulsive forces: the electron-electron repulsion, which is a result of electrostatic interaction, and the steric repulsion, which arises from the Pauli exclusion principle [33].

1.4 Structure of the dissertation

The background information about surface energy, interface shape, capillary forces and intermolecular interactions has been introduced in Chapter 1 in an overview of previous studies on the topic. Chapter 2 describes original experiments of the capillary force on a single spherical particle as it is pushed through an interface that is crowded with other particles. The effect of surrounding particles on the target sphere was studied, and the energy needed to detach a particle from interface was calculated and compared to the prediction of the Pieranski model described above. Chapter 3 explores the mechanical property of particulate assemblies by means of indentation. Interfacial systems with different combinations of liquids and particles were prepared. The force response of the particle raft along with the in-plane movement of particles were discussed in detail. Chapter 4 discusses the protocol of the formation of organic two dimensional material in aqueous media for the purpose of potential applications in passivating objects in suspension. The behavior of 2D sheets in water was explored by optical microscope.

CHAPTER 2

MEASURED CAPILLARY FORCES ON SPHERES AT FLUID INTERFACES

In this chapter, we discuss the measurement of capillary forces on particles at fluid interfaces in order to assess the key parameters that yield effective stabilizing particles. In our experiments, a millimeter-scale particle is attached to a cantilever, which is used to pull the particle perpendicular to the interface. Simultaneously, we image from the side to measure the cantilever's deflection and thus the pulling force, as well as the height of the particle and the shape of the interface. We find that the peak force on a particle at an interface crowded with other particles is consistently smaller than the force at a clean interface. This result is independent of the difference in fluid mass densities, the material of the target sphere, and the capillary charge of the free particles. We attribute the force reduction to the perturbation of interface shape due to the constraints at the boundaries of the free particles. The results provide new insights beyond the single-particle Pieranski model and should be helpful in designing particles to stabilize droplets in new oil dispersants or in other applications.

The results of this study were previously reported in He, W., Senbil, N. & Dinsmore, A. D.; "Measured Capillary Forces on Spheres at Particle-Laden Interfaces." Soft Matter 11, 5087-5094, (2015). DOI: 10.1039/c5sm00245a

2.1 Introduction

With the potential for particles to stabilize droplets established a century ago, surfactant-free particle-stabilized (Pickering) emulsions are now widely used in many fields such as biomedical, food products and oil-spill cleanup [5-9, 20, 34-36]. In the formation of a Pickering

emulsion, solid particles absorb onto the interface between the two phases and therefore prevent the coalescence of droplets. Emulsion stability largely depends on the behavior of those particles bound at interfaces. This makes it important to understand the fundamental physics of the capillary interaction on particle-laden interfaces. The understanding of the adsorption and desorption of particles at fluid interfaces paves the way to the design of optimal particulate dispersants that could efficiently stabilize emulsions. Early progress on this problem came from a geometric model, by Koretsky and Kruglyakov [37] and Pieranksi [6], of the binding energy for individual spheres at a clean, planar interface assuming that the contact angle is given by the equilibrium Young–Dupré value. Later work showed how the adsorption can be controlled by the fluid interfacial tension and by properties of the individual particles such as shape, roughness, and surface chemistry [21, 38-42]. Pitois and co-workers showed that hysteresis in the contact angle leads to a different force for inserting and withdrawing a sphere at an interface [43]. They also pointed out that the stability of Pickering emulsions should depend on the work to remove a bound particle (the work of detachment) rather than the equilibrium binding energy. The preceding studies, however, leave out the fact that particle-stabilized droplets may be packed with many particles, leaving open the question of whether the binding energy or work of detachment depends on the presence of other particles at an interface.

In experiments, tensiometry is the classical technique to measure the capillary force, in which small solid bodies are pulled through a fluid interface vertically. The most commonly used bodies are the (du Nouy) ring, the (Wilhelmy) plate and the sphere [11, 44-48]. After the invention of the atomic force microscope, the behavior of microscopic colloidal particles at interfaces was investigated by attaching the particle to the probe. In this way, capillary forces were measured and contact angles extracted from these data [49, 50]. This approach has been

used to measure how particle shape and surface roughness affect capillary forces [41, 42], which in turn affects emulsion stability [39]. More recently, forces were measured at the same time that interface shape and contact angle were obtained directly from the experiment [43]. This method will be essential for progress on the remaining questions about the role of interface shape and many-particle interactions.

In this chapter, we report measurements of the force on a sphere as it is withdrawn from or inserted into an interface between two immiscible fluids. For the case of individual spheres at an initially planar interface, we find that the results agree quantitatively with theory and we verify that the receding contact angle is constant during the withdrawal process. When freely floating particles are added to the interface, however, we find that the force-displacement curve changes. In particular the peak force needed to extract the sphere decreases by as much as 39%. We repeat the measurements under various conditions of the mass density of the fluids and of the particle; these results show that the peak-force reduction arises not from gravity or buoyancy, but rather from the capillary force itself. We conclude that fluid-interface-contact conditions around the free-floating particles alter the shape of the interface and thereby reduce the capillary force acting on the target sphere and the work needed to detach it from the interface. We discuss how these results should apply for particles that are micron- or nanometer-sized.

2.2 Experiment

2.2.1 Material and sample preparation

In most of experiments, spherical particles were used. They were all purchased from McMaster Carr: Borosilicate glass (1/8'' radius, cat. no. 8996K22, manufactured by Winsted Precision Ball Company), acrylic (R = 1/16" radius, cat. no. 1383K42), high-impact polystyrene

(1/16” and 5/64” radius, cat. no. 9374K21 and 9374K23), PTFE (3/64” and 1/16” radius, cat. no. 9660K12 and 9660K13), and chemical-resistant polypropylene (1/16” radius, cat. no. 1974K2). In some experiments, to find the shape of liquid interface, we used pieces of glass coverslips (#11/2, 22 mm square, VWR cat. no. 48366-227) as floating objects.

All particles except acrylic were cleaned before each set of experiments by sonicating in methanol for 2 min, rinsing in deionized water for 10 min, and then drying in air for 12 h. Acrylic particles washed in deionized water for 10 min, then dried in air for 12 h. Glass coverslips were first cut into small pieces, which have sizes ranging from 5 mm to 20 mm. Then those pieces were cleaned by sonicating in acetone and then methanol for 2 min respectively, rinsing in deionized water for 10 min, and drying in oven at temperature 75 °C for 2 h.

In order to minimize the effect of contact angle hysteresis, we coated glass spheres with polydimethylsiloxane (PDMS) to provide a smooth contact line and consistent contact angle. Borosilicate glass spheres were treated using the following procedure: glass spheres were first cleaned by soaking in a sulfuric acid and NoChromix® solution for 12 hours and then immersed in deionized water for 6 hours (water was changed every 30 minutes). Once dried, the spheres were functionalized by immersing them in polydimethylsiloxane using 20 mL disposable scintillation vials, baking in an oven for 24 h at 150 °C, then rinsing in toluene (1 h), acetone (1 h) and deionized water (2 h) [51].

The liquids used in the experiments were deionized water (Milli-Q plus) with a tabulated surface tension of 72 mN/m, two different types of silicone oil with density of 0.96 g/mL and 1.05 g/mL respectively (from Sigma-Aldrich, cat. no. 146153 and 175633) and squalane with density of 0.81 g/mL (Sigma-Aldrich, cat. no. 234311). Fluids were held in a glass crystallizing dish (KIMAX, cat. no. 23000; used for water–squalane experiments), a centrifuge tube (VWR

cat. no. 82018-052; used for water–silicone oil experiments) or a polystyrene tissue culture dish (BD Biosciences cat. no. 353002; used for water–air experiments). The diameters of these dishes were much larger than the capillary length l_c, which minimized the effect coming from the boundary of the container.

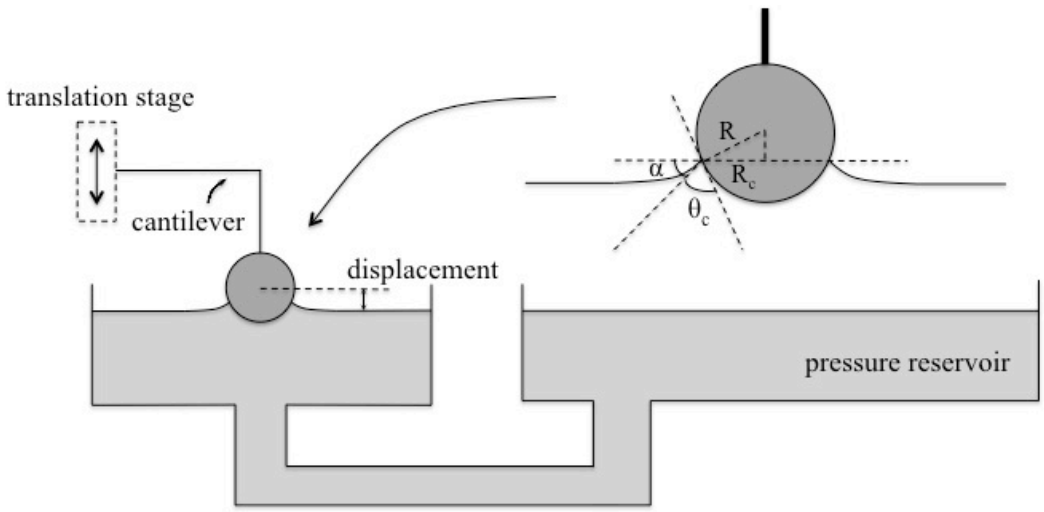

Figure 0.1 Schematic of the setup used for force-displacement measurements. Here, R is the sphere radius, R_c is the contact radius, θ_c is the contact angle, and α is the angle between the horizon and the interface at the contact line.

2.2.2 Apparatus and procedure

Figure 2.1 shows the schematic of the experimental setup used to insert or withdraw a sphere while measuring the force and imaging the interface shape. To fix the hydrostatic pressure at a certain displacement, the liquid bath was connected to a large liquid reservoir with a diameter of 100 mm. Both of the two containers were filled with same kind of liquid. The target sphere was linked to a force-measuring cantilever, and the cantilever was attached to a translation stage (Newport High-performance linear stage series 423), which provides fine control of the position of the target particle. We found that capillary tubing (Polymicro Technologies, cat. no. TSP020375) works well as the cantilever. Its stiffness was obtained by

calibration measurements, in which sections of metal wire of known weight were placed at the end of the cantilever and the deflection was measured. The deflection was captured by a digital camera (Nikon D3200 with a Nikon AF-S 18-55 mm lens and 68mm extension tubes) aimed perpendicular to the cantilever with a precision of 15 μm. Figure 2.2 shows the result for a typical calibration measurement, in which the deflection was found to be linear with weight in the range of 0 to 0.28 g (7 data points were used in analysis). The stiffness of the cantilever was usually around 0.5 N/m.

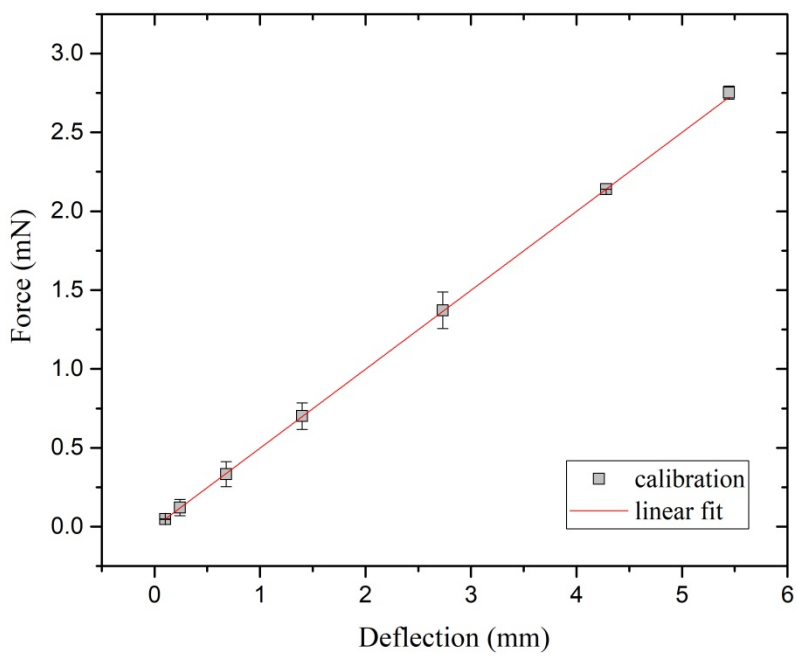

Figure 0.2 Measured forces of metal wires with known weights were plotted against their deflections. The solid red line is a linear fit to the data.

A typical experiment started with the target particle either hanging above the interface or being fully immersed in the lower liquid phase. Then the height of the target particle was adjusted manually in 0.2 mm increments (or decrements) using the translation stage. After each

displacement, the system was allowed to relax for 15 s, after which we saw no additional changes, and then side-view images of the particle region were captured by a digital camera. In some cases, another camera was placed above the setup to take top-view images (the inset of Figure 2.3).

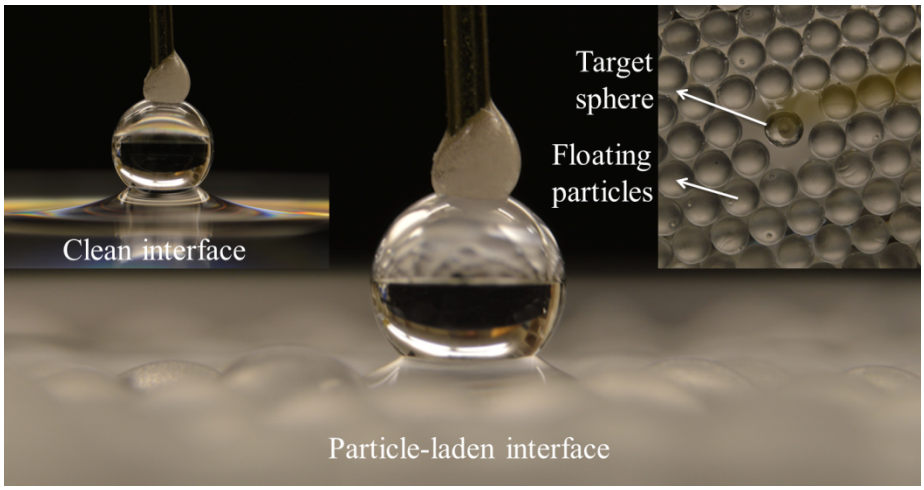

Figure 0.3 Side-view and top-view images of a PDMS-coated glass sphere at clean and particle-laden water-air interfaces respectively.

The force applied by the cantilever was calculated from the deflection of the end that is attached to the target sphere. Deflection was measured with a precision of 15 μm by analysis of the images using ImageJ [52]. With this approach, we obtain a typical force resolution of 8 μN. In all cases, we subtracted the weight of the target sphere so that measured $F = 0$ for a sphere in air. The vertical displacement (d) of the target sphere is defined as the distance between its mass center and the unperturbed interface. When the mass center is above the interface, $d > 0$. Displacement was measured with a precision of 15 μm by image analysis.

To study the effect of free-floating particles, we placed either spheres or pieces of glass coverslips on the interface. The spheres were bound to the interface and formed a two-dimensional hexagonal lattice owing to inter-particle attraction from the Cheerios effect [53].

Floating particles were characterized by their capillary charge, which is defined as the vertical component of capillary force, $f_{vertical}$. If $f_{vertical}$ is pointing from the lower liquid phase to the upper liquid phase, then the capillary charge is positive; otherwise negative. The lattice had a circular shape, and its size was much larger than the capillary length. As shown in Figure 2.3, several particles were removed from the center of the lattice to create a hole that was slightly larger than the target sphere. Hence there was no direct contact between the target sphere and the others throughout the measuring process, so that their effect on the target sphere was only by means of the fluid interface. Likewise, there was no direct contact between the target sphere and pieces of glass coverslips.

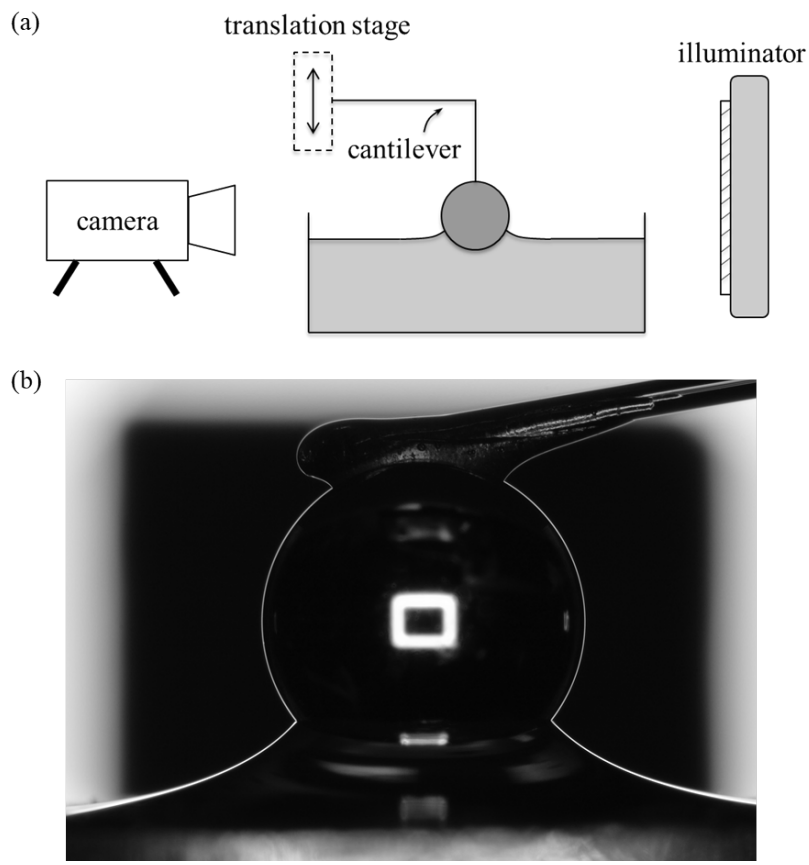

Figure 0.4 (a) Schematic of the setup used for contact angle measurements. (b) A typical image of a PDMS coated glass sphere with a radius of 1.6 mm being lift up from a water-air interface.

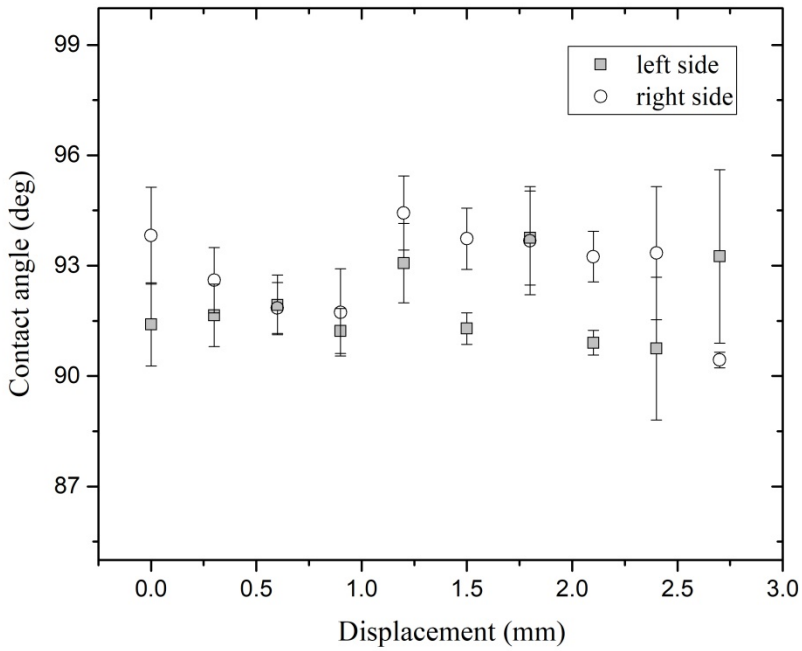

Figure 0.5 Measured contact angle on both sides *vs.* displacement for a PDMS coated glass sphere at a clean water-air interface.

2.2.3 Measurements of contact angle

Considering contact line pinning has a big effect on the force measurement, in some experiments, PDMS-coated glass spheres were used as target particles. The PDMS layer made the surface of glass smooth, which led to repeatable measurements and made it easy to calculate the force as well. Once borosilicate glass spheres were coated with PDMS following the procedure described in Section 2.2.1, their contact angle was measured by using the setup in Figure 2.4(a). A digital camera was used to take side-view images, while a partially blocked illuminator served as the light source. The target sphere was placed in between the camera and the light source, and its vertical position was controlled by a translation stage. By blocking the center region of the illuminator, the light captured by camera mainly came from scattering, and

therefore the edge of the particle and the liquid interface would be sharp, as shown in Figure 4(b).

Figure 2.5 shows the measured contact angle vs. displacement for a PDMS coated glass sphere at a clean water-air interface. The contact angle was obtained by using ImageJ [52]. We first fit a circle to the sphere, and drew a tangent line to it, which passed through the contact point. Then we drew a second line that was parallel to the meniscus near the sphere. The angle in between the two straight lines was the contact angle. The particle was initially immersed in water, and then we lift it up and let it pass through the interface. Since it was difficult to visualize the interfacial shape when the particle was below the surface, only apparent receding angles were recorded when the meniscus around was curved upward. Further the measurement only focused on two side points which were in the plane that was perpendicular to the camera. As we can see from Figure 2.5, the contact angle on both sides of a PDMS coated glass sphere at a clean water-air interface was close to each other throughout the pulling-up process, and fluctuated around 92.4°.

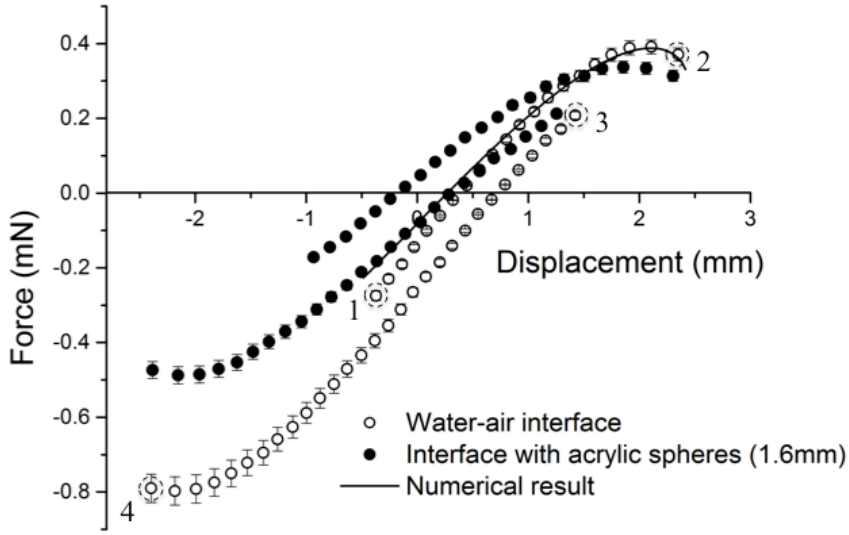

Figure 0.6 Measured force vs. displacement for the PDMS coated glass sphere at a clean interface (○) compared to the particle-laden interface (●). For each case, the upper (lower) trace shows the results for raising (lowering) the sphere.

2.2.4 Measurements of force

Figure 2.6 shows the results of a typical experiment, in which we measured *F(d)* on a PDMS-coated glass sphere at a clean air–water interface (open circles in Figure 2.6). Beginning with the particle immersed in water, we raised it in 0.2 mm steps. When the sphere touched the interface, the interface jumped downward to meet the sphere (position 1 on the plot). In this configuration the interface applied an upward force; to balance it the measured force, F, was negative. As the particle was raised further, the contact angle reached a steady value. The interface became less deformed and F increased toward zero, then became positive. As the target sphere was withdrawn into the upper air phase ($d > 0$), the interface became more strongly deformed until F reached a peak value. The force then decreased until the fluid bridge ruptured (position 2 on the plot). After this point, the sphere was in air and $F = 0$ (data not shown).

After leaving the sphere in the air phase for several minutes to allow the water on the sphere evaporate, we lowered the target sphere back through the interface. As soon as the sphere touched the interface ($d = R = 1.59$ mm), the interface rose to meet the sphere and applied a downward force (hence $F > 0$; position 3 on the plot). In this case, the fluid interface advanced across the surface of the sphere, so that the advancing contact angle was formed, which was larger than the receding angle. These data are shown by the lower sequence of open circular points in Figure 2.6. The *F(d)* curves for pulling out and pushing in were parallel to each other and the gap between them was caused by contact-angle hysteresis.

When the positive displacement is large, these data accurately fit the theory of Zhang et al. using the measured receding contact angle and known values of particle size, fluid densities, and interfacial tension [47]. However, near the beginning of the withdrawal process, the measured force was smaller than the theory because the contact angle had not reached its receding value. The actual contact angle was larger than the receding angle, which led to a smaller vertical component of capillary force. In the insertion process, the meniscus around the target sphere was below the surface. Such a situation made it difficult to measure the advancing contact angle and thus we did not compare the corresponding force curve with the theory.

We then added free-floating acrylic spheres on the interface and repeated the experiment with the same target sphere. The interface was packed with the spheres of positive capillary charge (Figure 2.3) except for the hole around the target sphere. The data show the same general trend as before, but the shape of the *F(d)* curve was altered and the value of the peak force was significantly reduced both on the air side ($d > 0$) and the water side ($d < 0$). In particular, the magnitude of the peak force fell by 14% when raising the sphere and by 39% when lowering it. Both of these changes are repeatable and exceed our measurement uncertainty. In the following

discussion, we will focus on the peak force because it is well-defined, easily measured, and independent of error in measuring the displacement (*d*) of the target sphere. We emphasize that, as in all of our particle-laden-interface experiments, the size of the hole was always larger than the diameter of the target sphere, and the target sphere was not in contact with any other spheres. Hence the effect on F was by means of the interface itself.

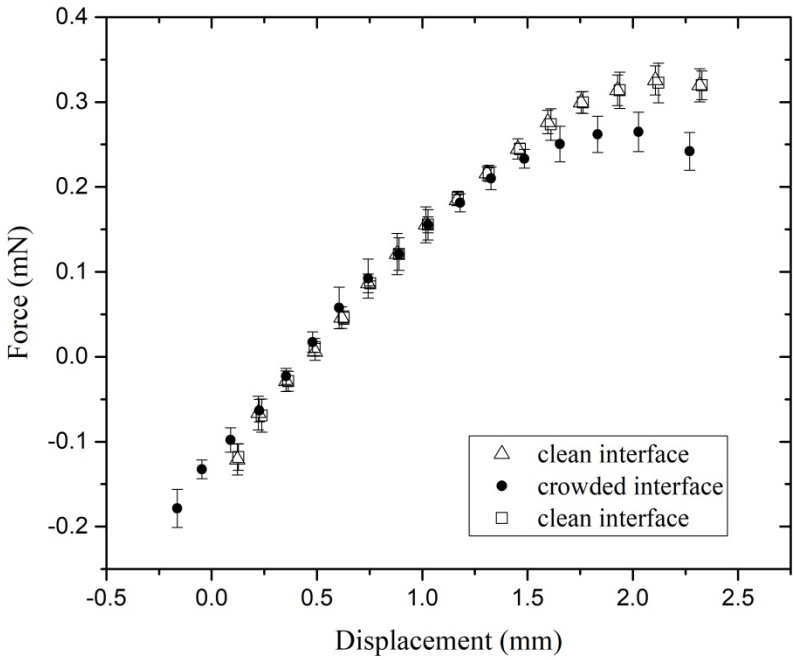

Figure 0.7 Measured force vs. displacement on a water-air interface with and without floating glass cover slip pieces.

To check the reversibility, we first conducted an experiment on a clean water-air interface, and then the experiment was repeated with the presence of floating glass cover slip pieces. Finally, those floating pieces were removed, and the force was measured again on a clean interface. As we can see from Figure 2.7, those open square points are indistinguishable from the open triangular points. It indicates that after removing floating glass pieces the measured

forces went back to their initial values, and hence the experiment is reversible. Although only one example was shown here, the reversibility was tested several times for all water–air systems, and the results are consistent.

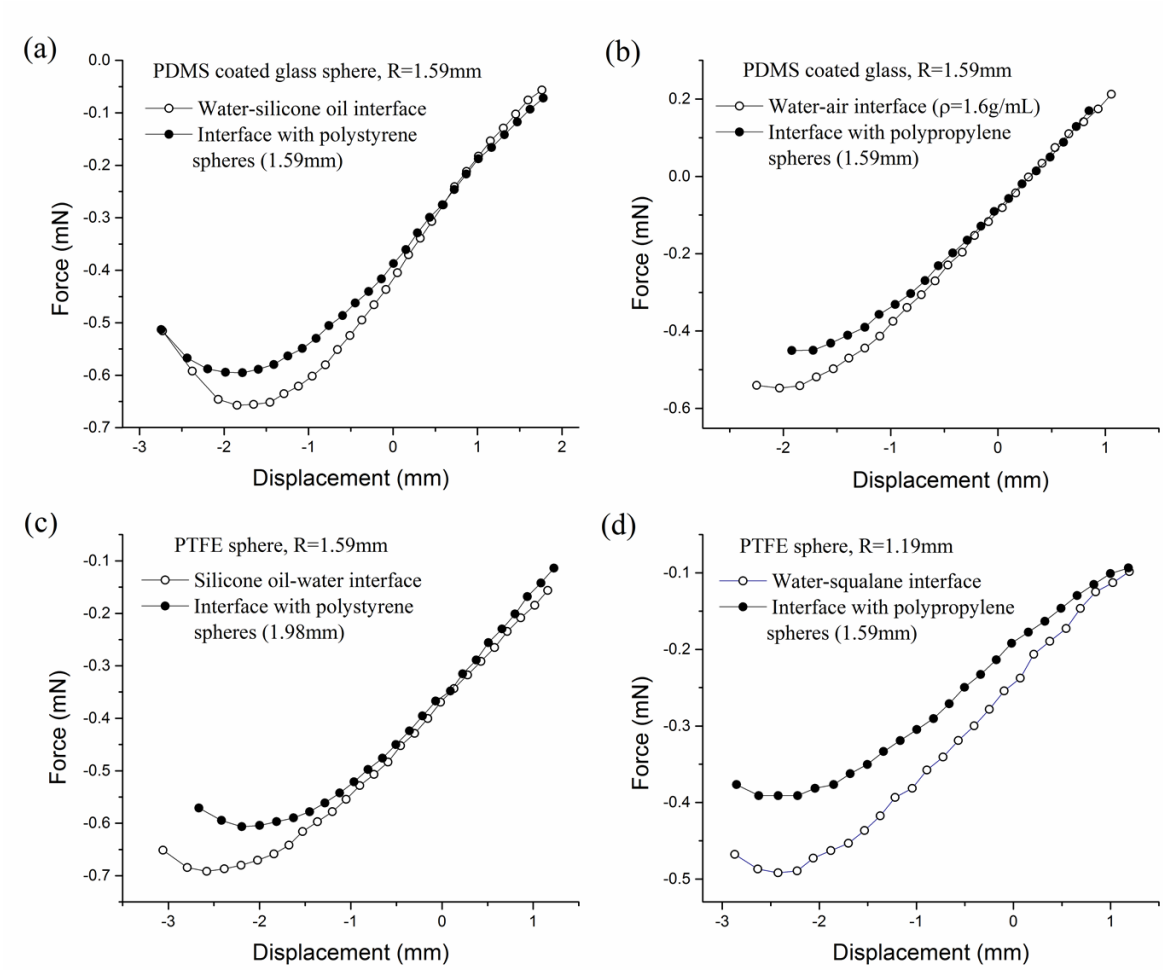

Figure 0.8 Measured force vs. displacement for different target spheres at different interfaces, providing examples with free spheres that are negatively buoyant (a), (c), positively buoyant (b), or nearly neutrally buoyant (d) free spheres, and with target spheres that are PDMS-coated glass (a), (b) or PTFE (c), (d). In each case, only the data for lowering the sphere is shown and the clean interface (○) is compared to the particle-laden interface (●).

We now turn to experiments using fluids and particles of different mass densities. Figure 2.8(a) shows measured *F(d)* curve for a PDMS-coated glass sphere at a water–oil interface. Here, the upper fluid phase is silicone oil ($\rho = 0.96\ g/mL$) and the lower fluid phase is deionized water

so that Δρ = 0.04 g/mL. For clarity, we show only the data for pushing the sphere downward (similar to the lower curves in Figure 2.6). As in the case of the water–oil interface, we compare the *F(d)* curves for an isolated sphere to the curves for a particle-laden interface (with polystyrene spheres of positive capillary charge, R = 1.59 mm). The resulting *F(d)* differs from the water–air experiments because of the different interfacial tension, contact angle and buoyancy. Nonetheless, we again find that the peak-force value is substantially reduced (here, by 9%) in the presence of the free spheres, despite the fact that the density mismatch of the two fluids was reduced by a factor of 25 compared to the water–air case. In this experiment, the calculated buoyant force acting on the sphere in the water and oil phases, respectively, is 0.164 mN and 0.158 mN, so that any change due to buoyancy could not affect the force by more than 6 μN, which is much smaller than the shift in force that we found.

Figure 2.8(b) shows the F(d) curve for pushing a PDMS-coated glass sphere (1.59 mm in radius) from air into water containing sodium polytungstate, added to raise the mass density to ρ = 1.6 g/mL. The higher mass density of the lower fluid caused the free-floating particles (here, polypropylene) to create upward-sloped menisci at the interface (capillary charge Q is negative). Once again, the interface that is laden with buoyant particles has a substantially lower peak force (by 18%) than the single-particle case for the same fluids.

So far, all target spheres used in experiments were PDMS-coated glass spheres. To extend the results to a more general case, we conducted experiments using different types of target spheres and floating particles. Figure 2.8(c) shows the measured force on a PTFE sphere (1.59 mm in radius) at a water–silicone oil interface. Here we used silicone oil with ρ = 1.05 g/mL, floating on water containing sodium polytungstate to achieve ρ = 1.05 g/mL. Hence, Δρ < 0.01 g/mL, which is at least 100× smaller than water–air. As floating particles, we use

polystyrene, which is also approximately density matched (ρ = 1.05 g/mL) and has slightly positive capillary charge. Once again, we found a substantial reduction of the peak force (by 12%) on the particle-laden interface.

Figure 2.8(d) shows the measured F(d) on a small PTFE sphere (1.19 mm in radius) at the interface between water and squalane (ρ = 0.81 g/mL). Polypropylene spheres were used as floating particles. These particles have a density between that of water and squalane and they are approximately neutrally buoyant; the interface around a single polypropylene bead had no measurable deformation (capillary charge Q is zero). Once again, the details of F(d) differ from the water–air case but the particle-laden interface has a smaller peak force (by 21%).

In all these cases, the data show a systematic reduction of the peak force in the presence of free-floating particles, irrespective of whether the particles deform the interface upward, downward, or not at all; whether the target sphere is a PDMS-coated glass or solid PTFE; and whether the two fluids are of different density or similar density. The results indicate that the force reduction does not arise from gravity acting on the fluids or particles.

This conclusion is not limited to the above-mentioned five cases. As target spheres, we also tested clean (non-functionalized) glass, nylon, polystyrene, polypropylene and acrylic spheres of different sizes. In those experiments, floating objects were nylon, polystyrene, polypropylene, acrylic spheres or small randomly shaped pieces of glass coverslips. All these combinations led to a force reduction.

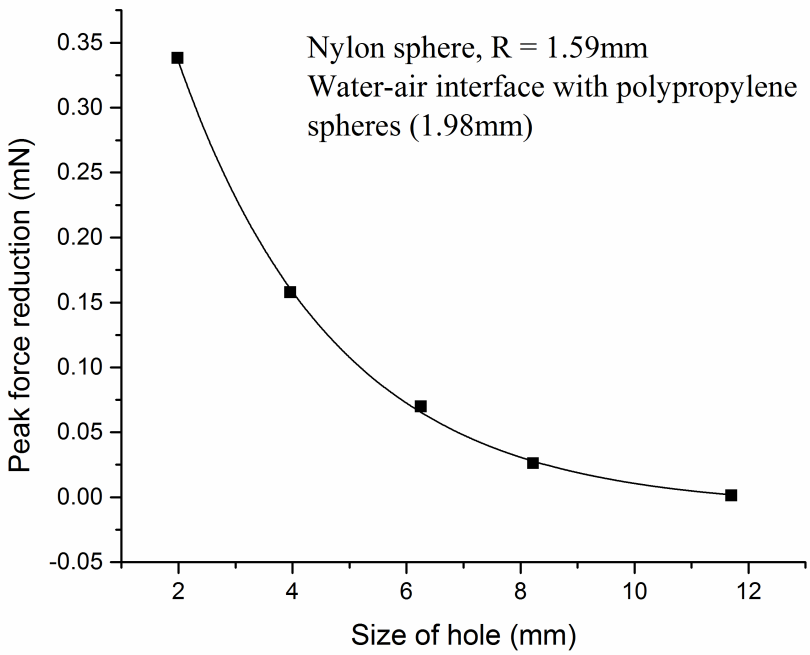

Figure 0.9 Plot of the measured reduction of the peak force as a function of the hole size in the array of free-floating spheres. The solid curve shows the best fit to an exponential with a decay length of 2.8 mm.

2.3 Results and discussions

2.3.1 Distance scaling

In Figure 2.9, we show how the size of the hole in layer of free-floating particles affects the change in the peak force (ΔF_{peak}). In this case, we used a nylon sphere as the target and polypropylene spheres as the free spheres. The peak force was measured for withdrawing the sphere from an air–water interface. The hole size was defined as the shortest distance between the center of the hole and the edge. As expected, when the size of the hole approaches the size of the dish (i.e. there is only a double ring of particles far away), these particles have no discernible effect on the target sphere. We fit the data to an exponential curve, $\Delta F_{peak} = Cexp(-a_h/\xi)$, where C and ξ are fit parameters and a_h is the size of the hole. We found a best fit for C = 0.8

and ξ = 2.8 mm; the latter is close to the calculated capillary length for water–air ($\sqrt{\gamma/\Delta\rho g}$ = 2.7 mm). Hence, it appears that the free-floating particles only affect the peak force when they are close enough to affect the interface shape. This result indicates that the reduced force is mediated by an altered interface shape.

2.3.2 Interface shape

By what mechanism do the free-floating particles alter the force on the target sphere? To address this question, we first point out that the measured force applied by the cantilever must balance a sum of five forces acting on the target sphere: (i) the capillary force, which comes from the fluid–fluid interface pulling around the ring of contact; (ii) the Laplace pressure acting on the surface of the target sphere that is exposed to the lower fluid; (iii) buoyancy of the particle (i.e., the force of gravity acting on the displaced fluid); (iv) the weight of the fluid that is pulled upward or downward in the meniscus; and (v) the "Cheerios" forces between the free-floating particles and the target particle [53, 54]. (In our experiments, the target sphere never came into contact with the free particles so there were no contact forces.) The second term, the Laplace pressure, was removed from consideration by keeping the pressure reservoir in contact with our system; in this way, the Laplace pressure at a given displacement is fixed irrespective of the shape of the interface. The third and fourth terms both depend on the difference of densities of the two fluids ($\Delta\rho$) and the data in Figure 2.8 show that the peak force is reduced even when ($\Delta\rho$) is smaller by 25× or 100×. The fifth term arises from the known fact that a free particle that creates a downward-sloped meniscus will attract (repel) a particle that a downward- (upward-) sloped meniscus; this is the pair-wise "Cheerios" force that pulls floating objects together. We showed in Figure 2.8 that the peak force is reduced whether the free particles pull the interface downward, upward or not at all; hence the pairwise capillary ("Cheerios") forces between the

free particles and the target particle cannot explain our data and we rule out (v) as the principal cause.

This leaves us with the first term, the capillary force arising from the fluid interface pulling at the contact ring on the target sphere. We point out that our setup ensures that the target particle touches only clean water–air or oil–water interface, so that the force per unit length acting on the contact ring (the interfacial tension) is the pure-fluid value in all cases. Hence the free-floating particles can only reduce the peak force via the shape of the fluid interface where it contacts the target sphere.

In previous experiments using PDMS-coated glass spheres, we found that the receding contact angle (θ_R) varies with the shape of the interface. Specifically, we found that θ_R decreased by approx. 10° when the deviatoric curvature, *D*, of the interface increased from 0 to 0.1 mm^{-1} [55]. (*D* is a measure of shape anisotropy, defined as half the difference between the two principal curvatures.) The advancing contact angle remained unchanged. In the present experiment, the free-floating particles perturb the planar interface so that D is non-zero, though still much smaller than 0.1 mm^{-1}. In any case, calculations show that a smaller θ_R would increase F, which contradicts our data. We conclude that the force reduction cannot be attributed to a change of receding or advancing contact angle.

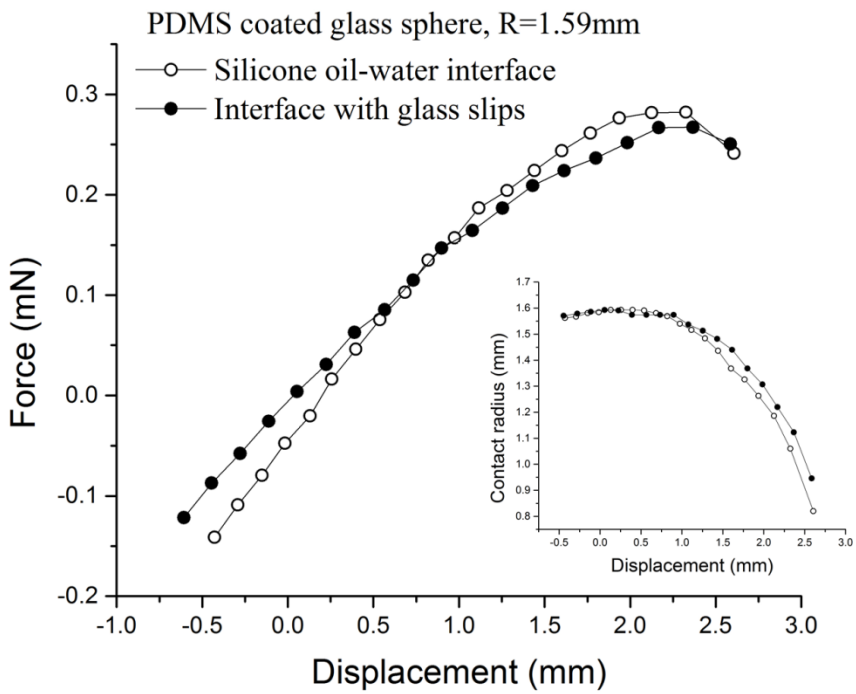

Figure 0.10 Measured force *vs*. displacement for a PDMS coated glass sphere at a water-air interface. Only the data for the raising process is shown. The inset is the corresponding contact radius as a function of displacement.

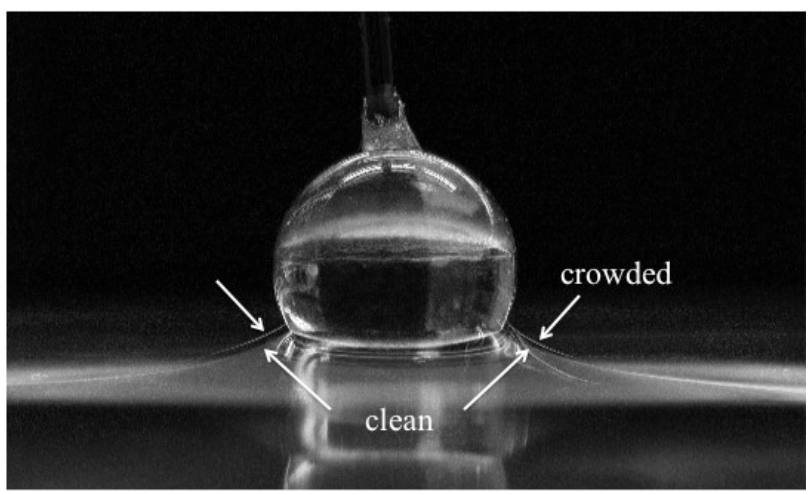

Figure 0.11 Overlay of an image of the PDMS-coated sphere at a clean interface (visible in the image) and at an interface crowded by glass coverslip pieces (white curve).

In the above experiments, the free-floating spheres obscured the interface so we could not see its shape clearly from the side. To image the interface shape, therefore, we used thin cover glass pieces (the square cover slips were cut into small irregular shape pieces) as the floating objects. Figure 2.10 shows the measured F(d) for a PDMS coated glass sphere (1.59 mm in radius) at the interface between water and air. Here only the raising process is shown in the plot, because the shape of the meniscus around the target sphere could only be captured when it rose above the background. The result is similar to what is shown in Figure 2.6: the peak force dropped by 6% on crowded interface.

Figure 2.11 is the overlay of two images: a PDMS coated sphere at a water-air interface, and the same sphere with the same displacement at an interface crowded by particles. From this side-view image, we found that the shape of the fluid interface changed in the presence of free particles: the contact ring on the target sphere changed from a circle to an undulating ring. To see how the altered contact-line shape by itself would affect the force in a general case, we numerically calculated the vertical component of the capillary force acting on the target sphere with a contact line that undulates with quadrupolar symmetry ($\sim\cos(2\emptyset)$ where $\emptyset$ is the polar angle in the plane of the interface). We assumed that the target sphere maintains a constant contact angle, which we find to be true for the clean interfaces. We found that the quadruploar term makes the vertical force slightly larger (on the order of several μN), presumably because of the greater length. The predicted difference is too small to be detected by our measurements and, of course, it contradicts our finding that the force decreases. Hence, the undulation of contact line is not a major factor leading to the force drop.

We observed in our experiments that, at a fixed displacement, the size of the contact ring around the target sphere in the particle-laden interface is greater than that at the clean fluid-fluid

interface, especially when the displacement is large (inset of Figure 2.10). The contact radius is defined as half the distance between left most and right most contact points in the image. To see how the capillary force is generically affected by a change in the contact-ring radius, we numerically calculated the vertical component of capillary force as a function of contact radius with fixed contact angle. The results indicate that the larger the contact radius is, the smaller the applied force is, which agrees with the measured $F(d)$. The reason for the larger contact radius on the crowded interface, however, is still not know.

As further evidence that the contact-ring size plays a role, we measured $F(d)$ on a PDMS-coated glass cylinder oriented perpendicular to the interface. As the cylinder was pulled upward, F increased slightly because of the decreased buoyant force. Adding free-floating particles to this interface had no measurable effect on the measured force.

2.4 Conclusion

In summary, we have experimentally proved that the presence of floating particles at an interface can reduce the peak force needed to remove the target sphere. The results were obtained using PDMS-coated glass spheres, which have uniform and smooth contacts, and also for PTFE and nylon spheres, where the contact rings are irregular but still have well-defined contact angles. We found that the peak force was consistently reduced whether the capillary charge of free-floating particles was positive, negative or zero, and when the difference in fluid mass densities ranged from 1.0 to 0.01 $\mathrm{g/mL}$. From these experiments, we ruled out gravity or buoyancy as the origin and instead concluded that the free-floating particles perturb the shape of the interface. This conclusion is supported by the images showing that the interface shape (especially the contact-ring size) are altered by the free-floating particles and also by our finding that the change in peak force decays as $exp(-a_h/l_c)$, where a_h is the distance between the free particles and the target particle and l_c is the

capillary length (Fig. 4). The force acting on a solid cylinder perpendicular to the interface was unaffected by the free-floating particles, consistent with the geometric fact that the cylinder has constant contact-line radius.

Not only does the peak force decrease, but the integrated work of removing the particle also changes. When a particle is ejected or removed from the interface by an external force, the work goes into changing the areas of the particle–fluid interfaces and of the fluid–fluid interface. (We neglect hydrodynamic dissipation because our forces are measured with stationary objects.) Once the particle snaps free of the interface, the energy stored in the excess fluid–fluid interface may be quickly dissipated as heat. Hence the work to remove a particle is larger than the binding energy. The total work to remove a PDMS coated glass sphere from the water–air interface, with its gravitational component ignored (obtained by a discrete integration of the measured F(d) of Figure 2.10) is 4.5×10^{-7} J, which is more than twice the predicted binding energy of 1.7×10^{-7} J. The integrated work to move a particle to the phase with lower contact angle at a particle-laden interface could be either larger (upper trace in Figure 2.6) or smaller (Figure 2.10) than the work at a clean interface. However, the work needed to push a particle into the phase with higher contact angle always decreases in the presence of free particles.

Although the experiments were performed on millimeter-scale particles, the fact that the results depend on interface shape and tension rather than gravity means that our results extend to micron- or nanometer-sized particles. In the latter cases, gravity and buoyancy are negligible and capillary effects predominate. In that limit, the peak force scales with interfacial tension and particle size. For the same relative particle sizes and inter-particle spacing, however, the relative change of peak force may be the same as reported here.

These results indicate that the stability of particle-laden droplets (as measured by the peak force or the work needed to remove a particle) is less than expected from single-particle measurements or theory. We attribute this effect to the fact that every free-floating particle introduces a constraint on the interface shape, and this network of constraints alters the interface shape (as shown in our experiments). These results demonstrate the need for a theory that describes effective interfacial tension or elasticity of a fluid interface crowded with particles.

CHAPTER 3

RESPONSE OF A RAFT OF PARTICLES TO A LOCAL MECHANICAL LOAD

3.1 Introduction

Fluid interfaces that are coated by a layer of adsorbed particles occur widely in insect colonies, in foods, in particle separation technologies and oil-spill cleanup, and suppression of water evaporation in reservoirs [5-10, 34-36, 56-59]. The basic ingredient that leads to wide utilization of particle-laden interfaces is their ability to keep interfaces apart and thereby prevent droplet coalescence. In some cases, the interfaces also confer rigidity, allowing non-spherical droplet shapes [60, 61]. In many of these examples, the mechanical response of the particle layer plays a crucial role in applications. For example, in concentrated Pickering emulsions, the storage and loss moduli are likely to be influenced by the mechanical response of individual particle-coated droplets. Meanwhile, it is also important to understand whether droplet breakup or coalescence are made easier or more difficult with particle-laden interfaces, compared to surfactant-coated interfaces.

A common method performed to assess the mechanical property of a material is indentation test. Supported by modern instruments such as atomic force microscopy (AFM), they can be carried out with extreme precision, and hence be used in characterizing even very small or soft materials such as graphene and biological cells [62, 63]. When applied to ultra-thin films resting on a substrate, wrinkle pattern and its evolution, which reveal the elasticity of the system, are observed as indentation advances [64, 65].

Although progress has been made in determining the elasticity of continuous films, the study for discrete systems is still in its early stage. Early progress on this problem came from the measure of

surface pressure-area isotherms by using a Wilhelmy plate in the Langmuir trough [24, 66, 67]. Through the compression-expansion cycles, this method successfully captures the transition from a fluid interface to an elastic interfacial monolayer due to the jamming of particles. However, it does not provide much information about the elasticity of the system. Later, more and more efforts have been devoted into understanding the buckling of particulate assemblies. Recent researches show that the bending modulus can be measured via static compression and propagation of surface waves [23, 27]. Moreover, in analogy to continuous sheets, both the wrinkle-to-fold transition and the cascading of wrinkles were also observed in particle rafts, which suggests the richness of phenomena associated with interfacial assemblies [26]. Further, the response of particle rafts to normal indentation was also reported recently. Although the presence of floating particles did not change the interfacial tension, they greatly enhanced the force an interface can bear [68].

Yet the response of the particle layer does not boil down to continuum elasticity. The rearrange of particles provides the raft with extra degrees of freedom to relax the dilation and compression induced by local mechanical loads. So far, it is still unclear how does the granular nature of the rafts attribute to the property of the interfacial monolayer.

In this chapter, we report the results of indentation tests on a particle raft sitting on liquid/gas or liquid/liquid interfaces. In experiments, both force and indentation were recorded simultaneously. Meanwhile, top view images were captured by camera to track the in-plane movement of particles. We used air, water and oil fluids to achieve capillary lengths (defined in Section 1.2.2) ranging from $2.72\ mm$ to $18.35\ mm$, and the size of the indenter was varied from $3\ mm$ to $10\ mm$. We found that the spring constant of the interfacial monolayer started with a small stable value at the beginning, then rose to a larger plateau, and decreased again for large indentation until the rupture of the interface. We repeated the measurements under various conditions of the liquids and of the particles;

by normalizing the measured force and indentation, all the results collapsed on to a single curve. Surprisingly, this curve matches the prediction of a purely capillary force arising from the fluid-fluid interfacial tension pulling on the boundary of the indenter. We conclude that when the indentation is not too large, the effect of floating particles is negligible and the force is determined by interfacial tension. This result may seem counterintuitive, but we show that particles move in the plane of the interface to accommodate the compression with low energy cost, so that the surface is dilated and the interactions between particles are weak. However, with the help of particles, the interfacial monolayer can sustain forces more than twice as large as that of a clean liquid/liquid interface. Also the depth that an indenter can reach on a particle laden interface is least doubled. Finally, we discuss how these results should apply for particles that are micron- or nanometer-sized. The results should be helpful in understanding the property of particle laden interface while both stretching and compression are present.

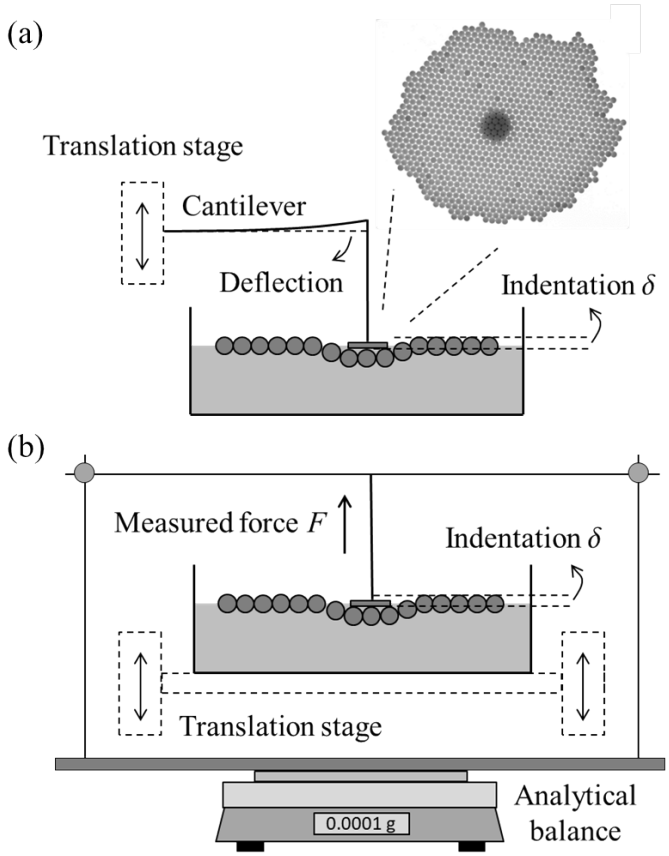

Figure 0.1 The schematic of experimental setup. (a) Cantilever based method. (b) Analytical balance based method.

3.2 Experiment

3.2.1 Apparatus and material

Figure 3.1 shows the schematic of the experimental setup used to determine the response of a particle raft to a local mechanical load. In most experiments reported here, we used the cantilever-based method, as shown in Figure 3.1(a), to measure the force acting on a flat bottom circular indenter. The indenter was attached by epoxy (ITW Devcon, no. 14277) to a metal needle, which was linked to a force-measuring cantilever. We found that plastic microscope slides (Fisherbrand, cat. no. S67112A) work well as the cantilever. Before each set of

experiments, the stiffness was obtained by calibration measurements described in Section 2.2.2. With this approach, we obtain a typical force resolution of 8 μN.

In some experiments, the force was directly recorded with a precision of 10 μN by using an analytical balance (METTLER Analytical balance AE100) as shown in Figure 3.1(b), in which the position of the indenter was fixed while the whole container was placed on a movable stage. In experiment, we moved the container up manually, and the contact force between the particle raft and the indenter was obtained from the change of the balance readout.

In all cases, the indentation (δ) of the indenter is defined as the distance between the bottom of the indenter and the top of unperturbed floating particles. For the cantilever based setup, δ was measured with a precision of 15 μm by image analysis, which was mainly affected by the resolution of the camera; for the case of using analytical balance, the vertical position of the container was controlled by a translation stage manually, and therefore the uncertainty came from the accuracy of translation stage, which is 5 μm.

The cantilever based setup has three main advantages. First of all, its precision of the force measurement depends on both camera resolution and stiffness of cantilever, and hence can be tuned for different experiments. Secondly, the method is not limited by the size of the particle-raft nor the size of container. Finally, if transparent contain were used in experiment, both top-down and bottom-up images can be obtained, which provide additional information about the in-plane movement of particles. However, a major drawback of cantilever based setup is the tilting of the indenter, which on one hand leads to more uncertainties in the measurement, on the other hand makes it easier to break the raft. Comparing to the cantilever based setup, the analytical balance approach provides greater control of the displacement of the probe as well as maintaining the indenter in a perpendicular

orientation. Due to the configuration of the balance, however, only small containers fit in the chamber and taking top-down or bottom-up images is not allowed.

We used polymer spheres to form rafts at liquid/air or liquid/liquid interfaces. These particles were all purchased from McMaster-Carr and Engineering Laboratories INC.: polymethyl-methacrylate (R = 1/16" radius, cat. no. 1383K42), high-impact polystyrene (R = 1/16", cat. no. 9374K21 and 9374K23), polytetrafluoroethylene (R = 1/16" radius, cat. no. 9660K13), chemical-resistant polypropylene (R = 1/16" radius, cat. no. 1974K2), polymethyl-methacrylate (R = 1/32"), polytetrafluoroethylene (R = 1/32") and polystyrene (R = 1/32"). All particles except acrylic were cleaned before each set of experiments by sonicating in methanol, rinsing in deionized water, and then drying in air. Acrylic particles were washed in deionized water, then dried.

The liquids used in the experiments were deionized water (Milli-Q plus) with a tabulated surface tension of 72 mN/m, two different types of silicone oil with density of 0.96 g/mL and 1.05 g/mL respectively (from Sigma-Aldrich, cat. no. 146153 and 175633), squalane with density of 0.81 g/mL (Sigma-Aldrich, cat. no. 234311) and hexadecane with density of 0.77 g/mL (from Sigma-Aldrich, cat. no. 105168). In some experiments, a mixture of silicone oil and hexadecane was used to minimize the density mismatch of two liquid phases. All experiments were performed at room temperature. Fluids were held in glass crystallizing dishes (KIMAX, cat. no. 23000 or PYREX, cat. no. 3140).

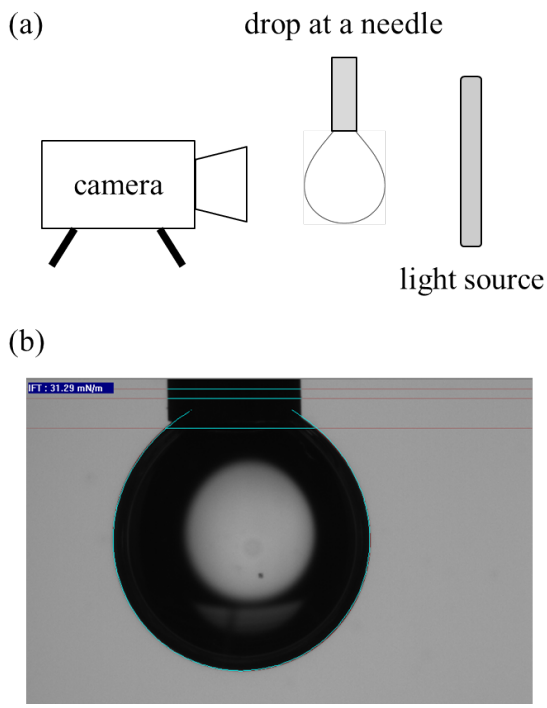

Figure 0.2 (a) The schematic of pendant droplet method. (b) A typical measurement for a silicone oil and hexadecane mixture droplet in water.

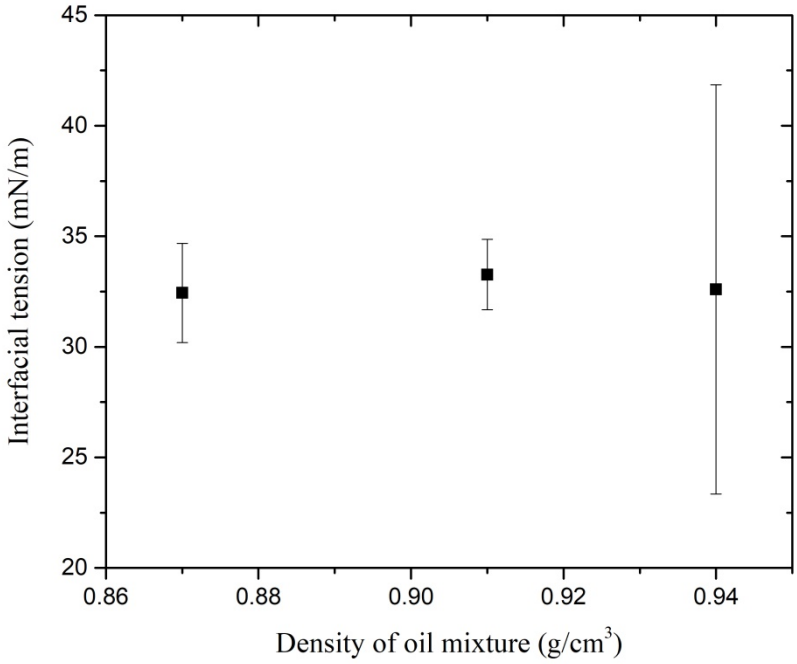

Figure 0.3 The measured interfacial tension of hexadecane/silicone oil mixtures with different densities (0.87 g/mL, 0.91 g/mL, and 0.94 g/mL).

3.2.2 Measurements of interfacial tension

For hexadecane/silicone oil mixtures, the interfacial tension was measured by using the pendant droplet method. Figure 3.2 (a) shows the schematic of the setup used to measure the interfacial tension. A droplet was placed in front of the light source, and its shape was captured by a digital camera. The profile of the droplet is determined by the competition between the surface tension, which tends to minimize the surface area and maintain the spherical shape, and the gravitation that aims to lower the potential energy and stretch the droplet from sphere to pear-shaped structure. The two competing terms are related to each other by Young-Laplace equation. By fitting the shape of pendant droplet obtained by the camera, the interfacial tension can be obtained accordingly. Figure 3.3 shows the measured interfacial tension of hexadecane/silicone oil mixtures with three different densities (0.87 g/mL, 0.91 g/mL, and 0.94 g/mL). We found that the interfacial tension didn't change much when the density varied from 0.87 g/mL to 0.94 g/mL. In the following experiment, we would assume the interfacial tension of hexadecane/silicone oil mixture is the average of three measurement, 32.8 mN/m.

3.2.3 Procedure

To study the effect of having free-floating particles, spheres were placed on the liquid/liquid or liquid/air interfaces by hand. Those spheres were bound to the interface and formed a two-dimensional hexagonal lattice owing to inter-particle attraction from the Cheerios effect described in Section 1.2.3 [53]. Then, to minimize the effect from the shape of particle raft, we manually rearranged the lattice to make the raft as circular as possible. Before each set of experiments, we made sure that there was no defect in the lattice. Also, to minimize the boundary effect from the edge of the sample container, we had the radius of the container to be much larger than the size of the particle raft.

To minimize the boundary effect from the edge of the sample container, we made sure that the edge of the container was at least 5×l_c away from the edge of the particle raft in all experiments.

Figure 3.4 (a) and (b) show the displacement of those particles near and underneath the indenter in the process of an experiment when δ was small (at the beginning of the experiment) and large (before the rupture of the raft) respectively. The displacement was computed by comparing the position of the same particle in different frames. In Figure 3.4, to better visualize the result, the magnitude of the displacement was magnified by a factor of 10. We noticed that two particles under the indenter had non-zero displacement in the plots. However, further analysis showed that the detected movement was due to the tracking error of particles. Apart from that, it is clear that particles beneath the indenter had no in-plane movement in a typical experiment, which indicates that the indenter provides a non-slippery contact before the rupture of the raft, and hence those particles sitting below could be regarded as a single, rigid piece.

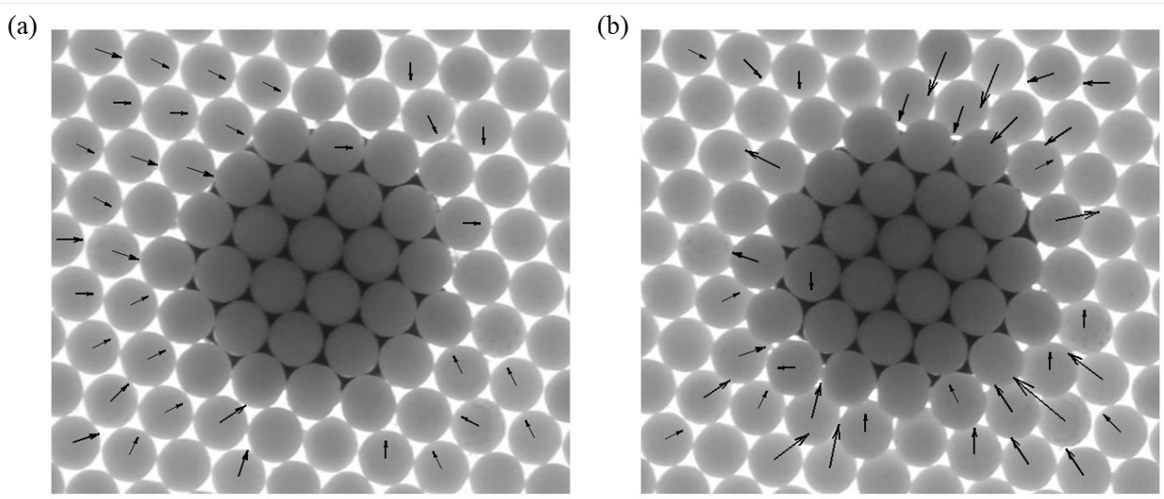

Figure 0.4 Displacement of PTFE particles underneath and near the indenter in a typical experiment performed on a water-air interface. (a) The displacement field when δ is small compared to l_c. (b) The displacement field for large δ.

In a typical experiment, starting with the indenter hanging above the raft, we gradually lowered it (or raised the container) by a certain distance. The height of the indenter (or the container) was adjusted manually by using the translation stage. After each displacement, the system was allowed to relax for 15 s, after which we saw no additional changes in the particle layer. In each experiment, the force, f, exerted by the indenter and the corresponding indentation, δ, were recorded simultaneously. Forces and indentations pointing downward are defined as positive. The starting point was chosen as the moment when the indenter first touched the particle raft. Then experiment continued until either the raft was broken or the indenter moved beyond the measuring range, whichever came first. Between each set of experiments, the indenter was cleaned and dried, and the raft was restored to its initial state manually. All experiments were performed at room temperature.

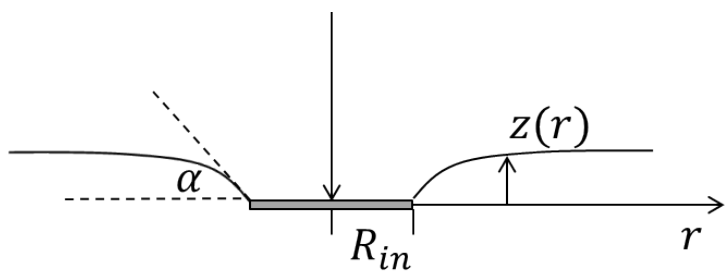

Figure 0.5 Interface deformed by a flat bottom indenter with a radius of R_{in}.

3.3 Shape of interface under different boundary conditions

The design of the above experiment is to determine the stiffness of the particle layer by analyzing its response under different mechanical loads. The contribution coming from those floating particles can be obtained by comparing F-δ curves to those of interfaces with and without particles. In this section, we discuss simplified models consisting of a clean fluid interface without particles, and then consider two ways to model the free-floating particles by using effective boundary conditions. These will be compared to the experimental results later.

To address the problem, we first derived the vertical force acting on a flat-bottom indenter, as shown in Figure 3.5, poking on a clean liquid/liquid interface without particles. Under the assumption that the contact line pins on the edge of the indenter and the deformation is zero infinitely far away, there are only two forces we need to consider: the hydrostatic force, which pushes up from the bottom of the indenter and the vertical component of capillary force, which pulls on the edge. The hydrostatic force, f_h, is a linear function of δ, and can be expressed by

$$f_h = \pi R_{in}^2 \gamma \Delta\rho g \delta = \pi \gamma \tilde{R}^2 \delta \quad (3.1)$$

where $\tilde{R} = R_{in}/l_c$. The indenter radius is R_{in} and the capillary length is l_c. The vertical component of the capillary force is given by

$$f_c = 2\pi R_{in} \gamma \sin(\alpha) \quad (3.2)$$

where α is the inclination angle between the tangent line of meniscus at $r = R_{in}$ and the horizon. To calculate the inclination angle, we need to find out the interfacial shape around the indenter. According to Section 1.2.2 and along with an extra condition

$$\mathrm{z}(R_{in}) = \delta \ (3.3)$$

we have

$$f_c = 2\pi\gamma\tilde{R}\frac{K_1(\tilde{R})}{K_0(\tilde{R})}\delta \quad (3.4)$$

where K is the modified Bessel function of second kind. Equation 3.4 shows that for a quasi-flat interface the vertical component of capillary force is also a linear function of δ. Finally, the total force acting on the indenter at a fluid-fluid interface is

$$f = f_h + f_c = \pi\gamma\tilde{R}^2\delta + 2\pi\gamma\tilde{R}\frac{K_1(\tilde{R})}{K_0(\tilde{R})}\delta. \quad (3.5)$$

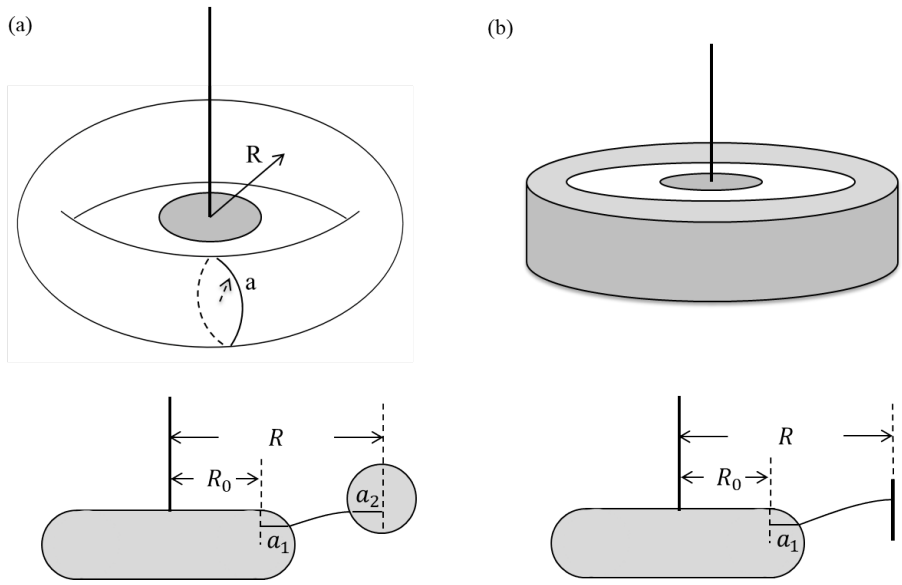

Figure 0.6 Schematic of simplified models with different boundary conditions. (a) Nearby particles are treated as a torus with a major radius of r and a minor radius of a. (b) A hollow cylinder sets the boundary near the indenter.

The above result holds for the situation that the interface is infinitely large and the contact line pins perfectly on the edge on the indenter. However, on a particle laden interface, the measured force might be different from Equation 3.5 due to the constraint imposed by floating particles. In order to explore the role of those particles, we now solve the Helmholtz equation under different boundary conditions. Considering the indenter provides a non-slippery contact, we first modeled those particles beneath the indenter as a pancake object with a major radius of R_0 and a minor radius of a. Further we approximated those nearby particles either as a torus (Figure 3.6(a)) or a hollow cylinder (Figure 3.6(b)). To simplify the calculation, we assume that the contact angle on all surfaces remains a constant, $\pi/2$.

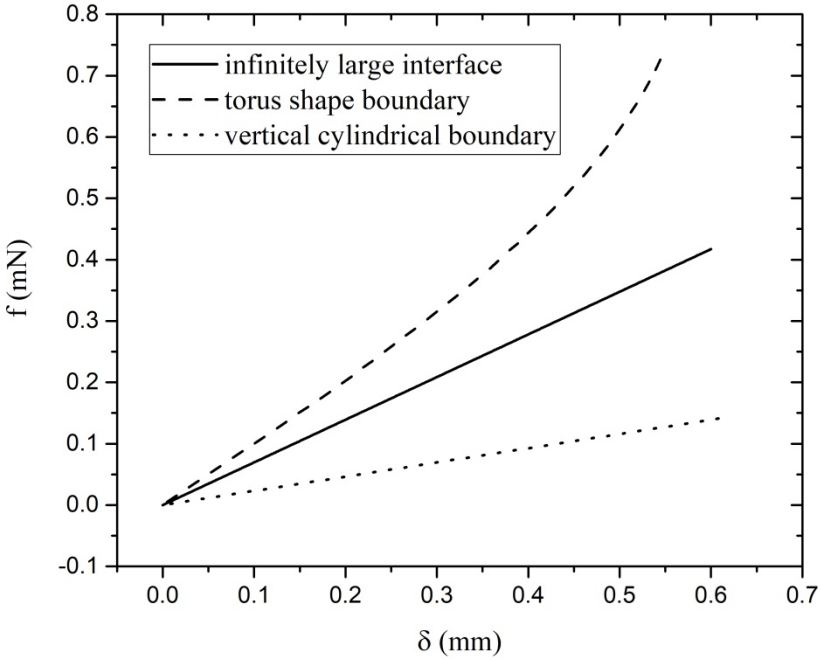

Figure 0.7 Numerical results for different boundary conditions.

For the torus case, we have the following boundary conditions:

$$\mathrm{z}(R) = \sqrt{a^2 - a_2^2} \quad (3.6)$$

$$\mathrm{z}(R_0 + a_1) = \delta - \sqrt{a^2 - a_1^2} \quad (3.7)$$

$$\frac{\partial \mathrm{z}}{\partial r}\Big|_{R-a_2} = \frac{\sqrt{a^2 - a_2^2}}{a_2} \quad (3.8)$$

$$\frac{\partial \mathrm{z}}{\partial r}\Big|_{R_0+a_1} = \frac{\sqrt{a^2 - a_1^2}}{a_1} \quad (3.9)$$

where a_1 and a_2 are the contact radius on pancake and torus respectively. By solving the Helmholtz equation, we have

$$\mathrm{z}(r) = \frac{l_c}{Q}\left[\frac{\sqrt{a^2 - a_2^2}}{a_2} K_1\left(\frac{R_0 + a_1}{l_c}\right) + \frac{\sqrt{a^2 - a_1^2}}{a_1} K_1\left(\frac{R - a_2}{l_c}\right)\right] I_0\left(\frac{r}{l_c}\right)$$

$$+ \frac{l_c}{Q}\left[\frac{\sqrt{a^2 - a_1^2}}{a_1} I_1\left(\frac{R - a_2}{l_c}\right) - \frac{\sqrt{a^2 - a_2^2}}{a_2} I_1\left(\frac{R_0 + a_1}{l_c}\right)\right] K_0\left(\frac{r}{l_c}\right) \quad (3.10)$$

where $Q = K_1\left(\frac{R-a_2}{l_c}\right) I_1\left(\frac{R_0+a_1}{l_c}\right) - K_1\left(\frac{R_0+a_1}{l_c}\right) I_1\left(\frac{R-a_2}{l_c}\right)$ and I is the modified Bessel function of first kind. In the above two equations, a_1, a_2 and δ are not independent to each other. They related to each other through the first two boundary conditions. In experiments, δ was measured directly, and hence a_1 and a_2 were uniquely determined.

For the case of hollow cylinder, by using boundary conditions

$$\mathrm{z}(R_0 + a_1) = \delta - \sqrt{a^2 - a_1^2} \quad (3.11)$$

$$\frac{\partial \mathrm{z}}{\partial r}\Big|_R = 0 \quad (3.12)$$

$$\frac{\partial \mathrm{z}}{\partial r}\Big|_{R_0+a_1} = \frac{\sqrt{a^2 - a_1^2}}{a_1} \quad (3.13)$$

we derived the shape of interface and the vertical component of capillary force as following

$$\mathrm{z}(r) = \frac{l_c}{Q'}\frac{\sqrt{a^2 - a_1^2}}{a_1}\left[K_1\left(\frac{R}{l_c}\right) I_0\left(\frac{r}{l_c}\right) + I_1\left(\frac{R}{l_c}\right) K_0\left(\frac{r}{l_c}\right)\right] \quad (3.14)$$

where $Q' = K_1\left(\frac{R}{l_c}\right) I_1\left(\frac{R_0+a_1}{l_c}\right) - K_1\left(\frac{R_0+a_1}{l_c}\right) I_1\left(\frac{R}{l_c}\right)$. Similar to the torus case, a_1 and δ are linked to each other through the first boundary condition.

Once we know the shape of interface, the vertical component of capillary force can be easily calculated. Figure 3.7 plots the numerical results of f as a function of δ for three different

sets of boundary conditions. Parameters were chosen as $R = 4\ mm, R_0 = 2.2\ mm, a = 0.8\ mm$ and $l_c = 2.72\ mm$. Comparing to the case of infinitely large interface, having a torus-shaped boundary leads to a larger $df/d\delta$, while the vertical cylindrical wall makes the force smaller at a fixed indentation.

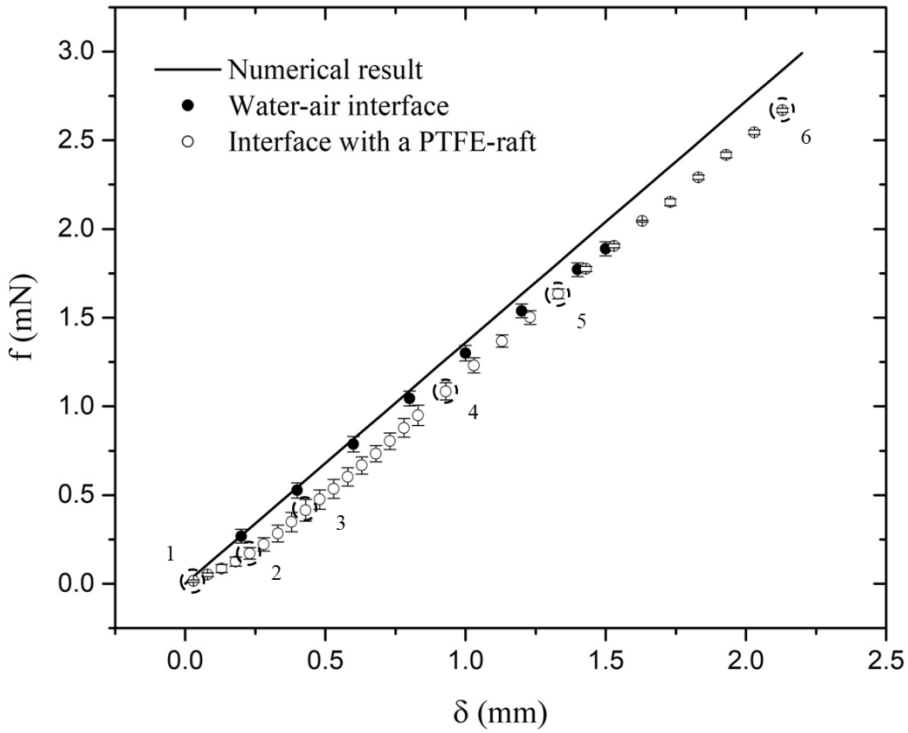

Figure 0.8 Measured force, f, *vs.* indentation, δ, for a 4 mm circular bottom indenter at a clean interface (●) comparted to a particle-laden interface (○).

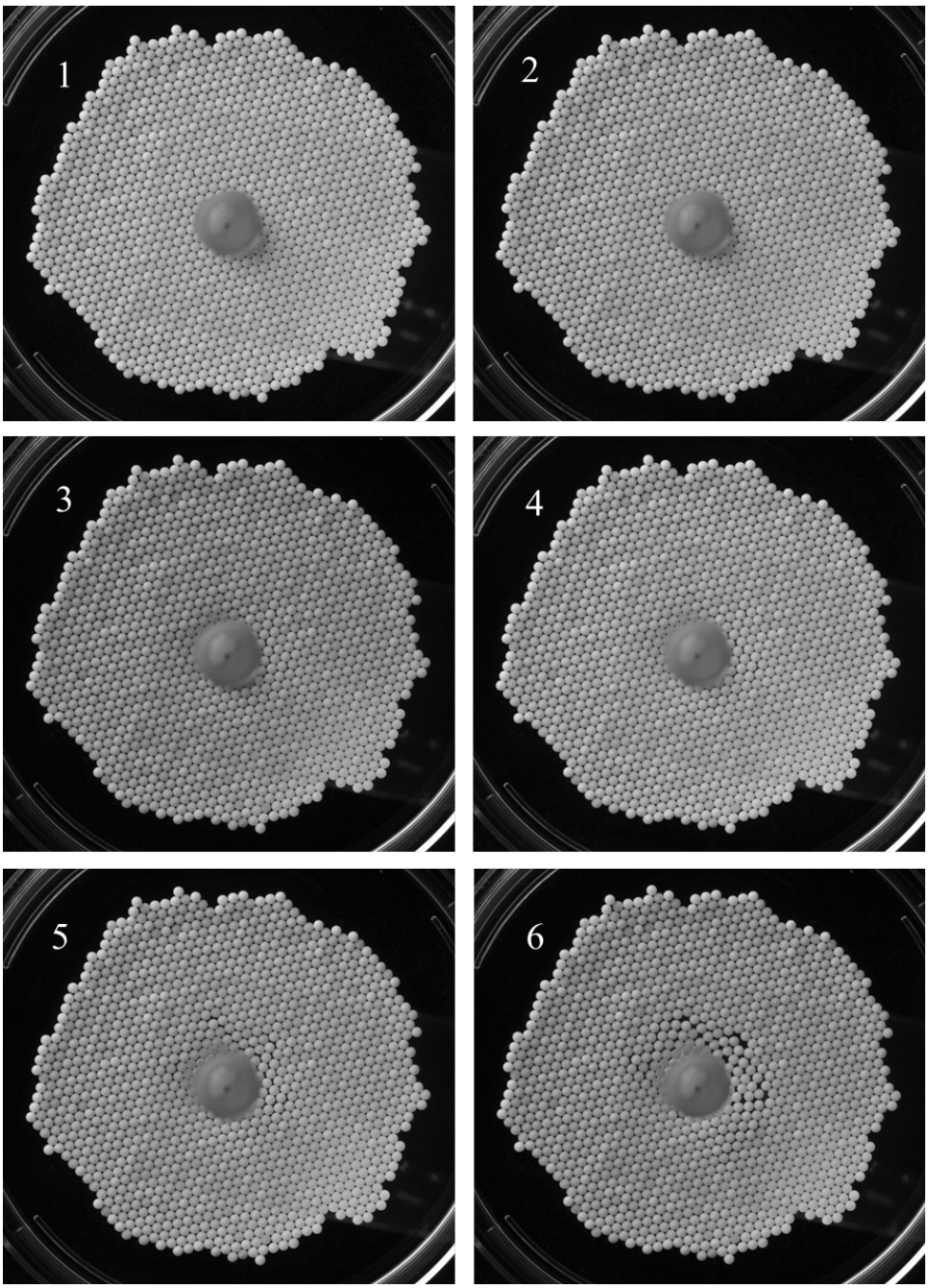

Figure 0.9 Top-view images of the particle raft at various indentations.

3.4 Results and discussion

Figure 3.8 shows the results for a typical experiment, in which we measured $f(\delta)$ on a 4 mm circular, flat-bottom indenter pushing through a clean water-air interface (solid circles in the

figure). As we can see, most of the data points fall on the black line in the plot, which is the numerical result from Equation 3.5. However, when δ was large, the measured force was smaller than its predicted value. There are two reasons for the deviation: firstly, the contact line could not perfectly pin on the edge of the indenter, and hence slipped upward, which reduced the tilt angle α and thus the vertical component of capillary force; secondly, the numerical result is based on the assumption that the interface is nearly flat, however it was not the case when δ was large.

After the control experiment, particles were added onto the interface, and the measurement was repeated for the same indenter poking on a particle raft floating on the water-air interface (open circles in the figure). The raft in this particular experiment was made up of Teflon spheres with uniform radius, a, 0.79 ± 0.05 mm. Starting from the moment that the indenter just touched the particle raft (the first point in the lower left corner), f increased in the positive direction as δ grew. At the beginning, the slope of f-δ curve was smaller than its clean interface counterpart. As shown in Figure 3.9 (picture 1 and 2), there was no noticeable in-plane movement of particles in top-view images. As δ was increased, the slope of the force curve increased initially, and after it reached a value that was approximately the same as coefficient of Equation 3.5, it remained there for a few millimeters. In this process, nearby particles were pulled towards the indenter. As an example, Figure 3.10 shows the displacement field at moment 5 in Figure 3.8 (the calculated strain field can be found in Appendix B). It is clear that only particles in certain directions were moving towards the indenter. Such movements were the origin of the star-shaped pattern developed in the raft. As the indenter kept moving downwards, the raft as further stretched in the radial direction, as shown in Figure 3.9 (picture 6).

The last data point in the plot was taken right before the rupture of the raft. Figure 3.11 shows the side-view image of moment 6. Since the indenter has a finite thickness, particles near

the edge rolled over the indenter when the interface was highly curved. It opened a gap so that water could sneak in and wet the indenter. Once touched by water, a meniscus formed immediately, which broke the integrity of the raft. The dramatic breakup of the raft when the indenter made direct contact with the fluids made it easy to distinguish from deformations caused by poking the raft.

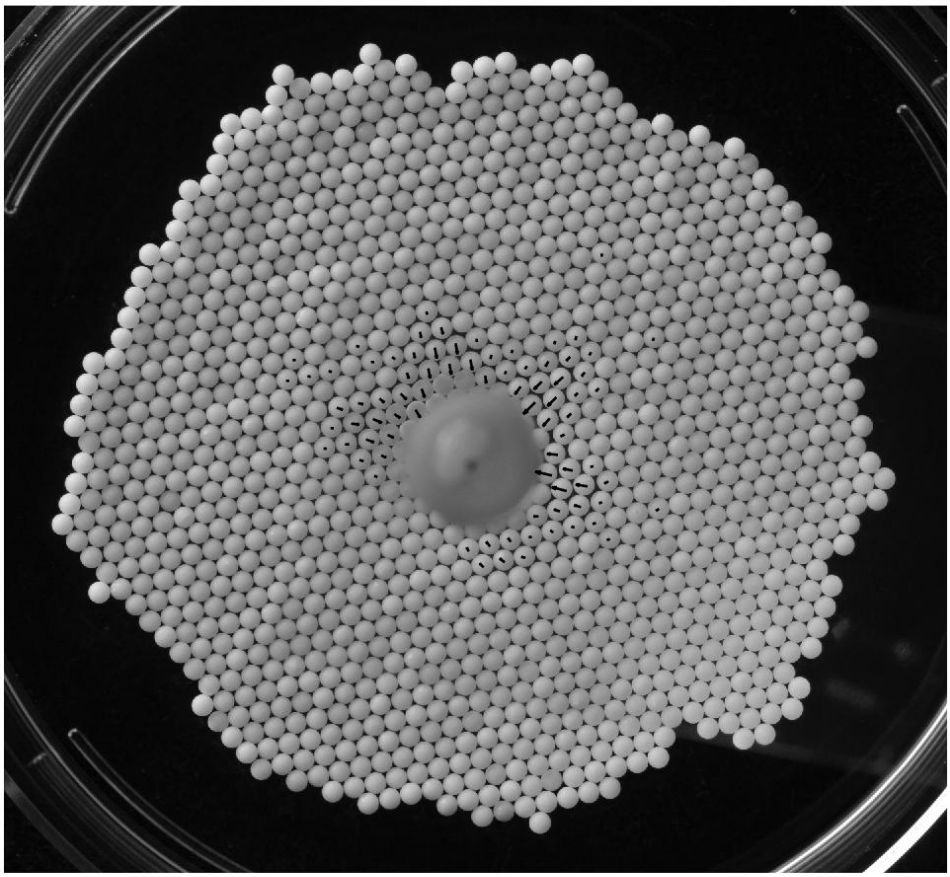

Figure 0.10 In-plane displacement field of Teflon particles at a water-air interface.

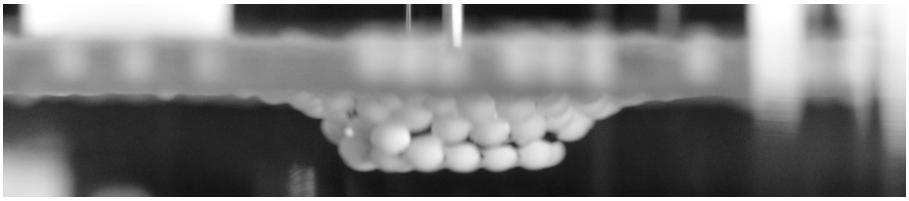

Figure 0.11 Side-view image for the last data point recorded.

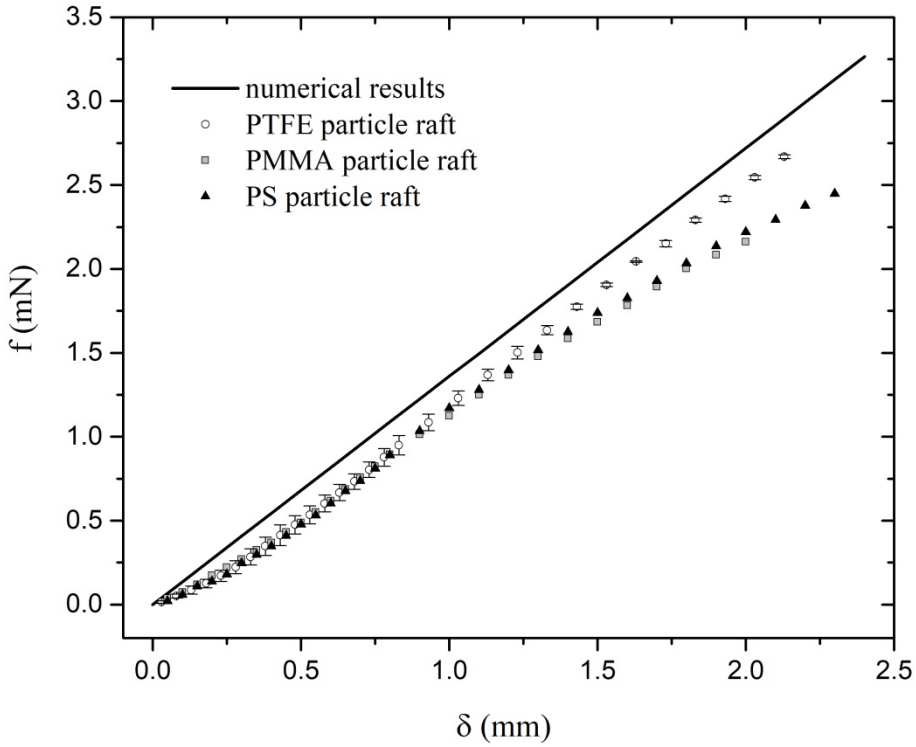

Figure 0.12 Measured force, *f*, versus indentation, δ, for different kinds of particle rafts.

To check how the f-δ curve depends on the species of particles, we conducted experiments by using the same 4 mm flat bottom circular indenter but with acrylic or polystyrene particle rafts. Those particles were of the same size as Teflon spheres in the previous experiment (a = 0.79 mm). Also we made sure that the radius of rafts was consistent from one measurement to the next so that the size effect could be minimized. Figure 3.12 plots the measured f against δ for rafts made up of different kinds of particles. The black straight line is again the numerical result from Equation 3.5. As we can see in the plot, when the indentation is smaller than 1 mm, there is almost no difference among the three curves. It suggests that all rafts behave similarly. However, when δ was large, acrylic and polystyrene particle rafts had a smaller force comparing to the Teflon raft at a fixed indentation. Such a force drop might be attributed to the difference in

hydrophobicity. Both acrylic and polystyrene are hydrophilic with contact angles of 77.5° and 89.2° respectively. Those contact angles were measured around a single particle sitting at a flat water-air interface. Hence comparing to Teflon particles, they are relatively easier to be forced into the aqueous phase without deforming the interface much.

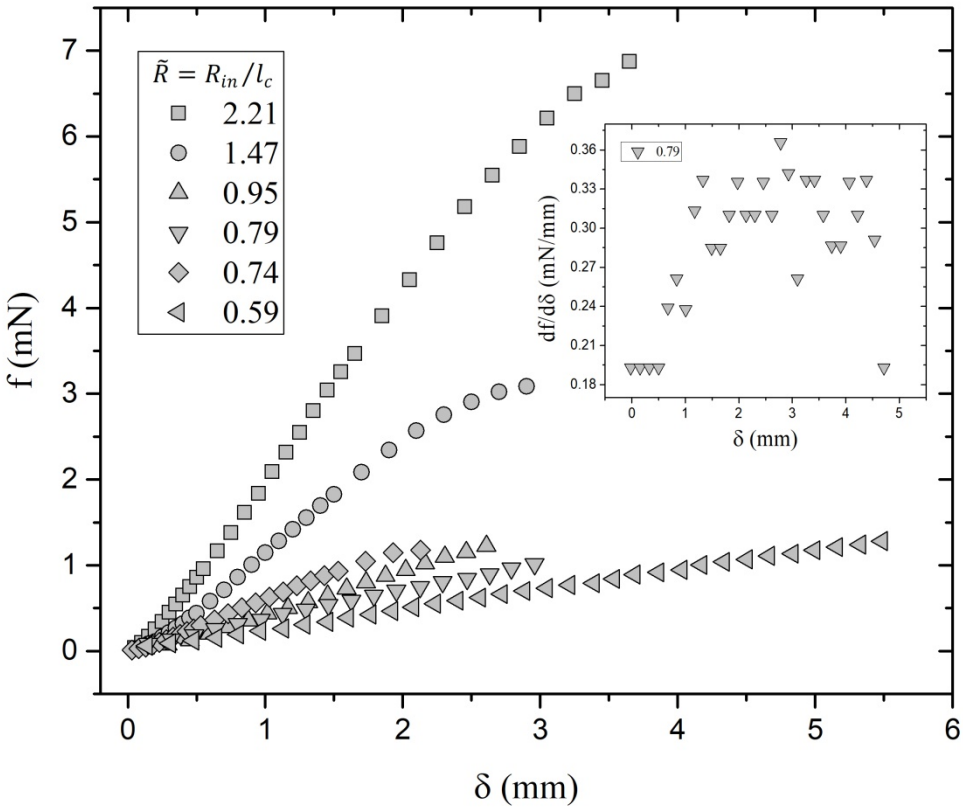

Figure 0.13 Measured force, f, versus indentation, δ, for different combinations of particles, liquids and indenters. Inset is the plot of $df/d\delta$ versus δ for an experiment on a water-silicone oil interface with $\tilde{R} = 0.79$. This plot shows a plateau at small δ and another plateau over a range of δ from approximately 1-4 mm.

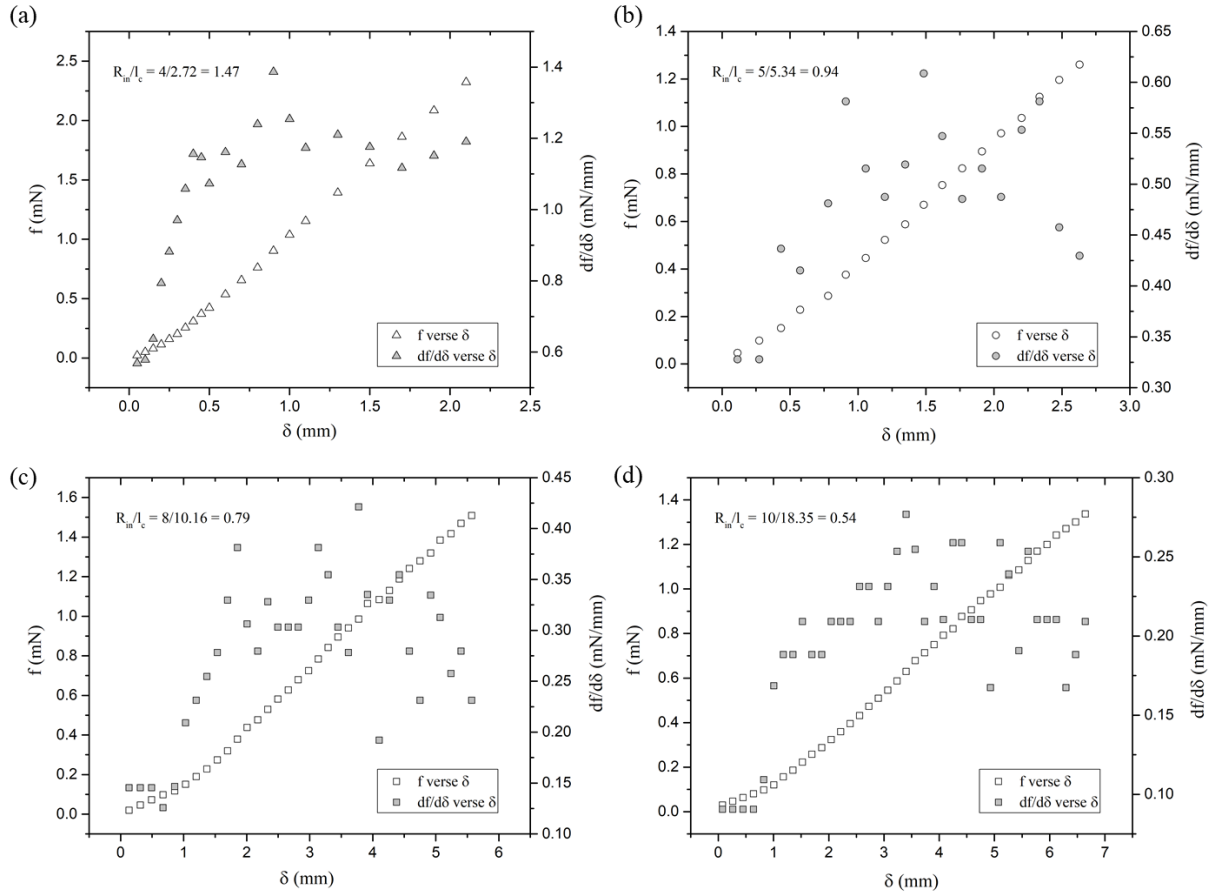

Figure 0.14 Measured force, f, versus indentation, δ, for different combinations of particles, liquids and indenters, and the corresponding plot of $df/d\delta$ versus δ.

We now turn to experiments performed on different kinds of liquid/liquid interfaces (water-air, water-squalane and water-silicone oil) with various ratios of indenter radius, R_{in}, and capillary length, l_c, ranging from 0.59 to 2.21. Particle rafts in those experiments were made up of spheres with same size a, 1.58 mm. In the experiments performed on a water-air interface, Teflon particles were used to form rafts; while in experiments with water-oil interfaces, rafts were composed of polystyrene particles. In Figure 3.13 measured forces were plotted against their indentations for six experiments with different combinations of parameters. Although some of the f-δ curves are close to straight lines, a close look shows that their slopes varied throughout

the experiment. To capture this nonlinear feature, we replotted the data in the form of $df/d\delta$ vs. δ. The inset of Figure 3.13 shows an example of $df/d\delta$ vs. δ curve measured for a polystyrene-particle-raft on a water-hexadecane/silicone oil mixture interface with an interfacial tension of $32.8\ mN/m$. More examples of $df/d\delta$ vs. δ curves for different combinations of particles, liquids and indenters were shown in Figure 3.14. They all have similar behaviors. At the beginning, $df/d\delta$ remained a constant over a range of δ which was much smaller than the capillary length. When δ became larger, the spring constant of the system also increased. After a short transition region, $df/d\delta$ entered a second plateau region, in which it fluctuated around a constant value. When the indenter kept moving downwards, the stiffness of the particle-raft dropped again.

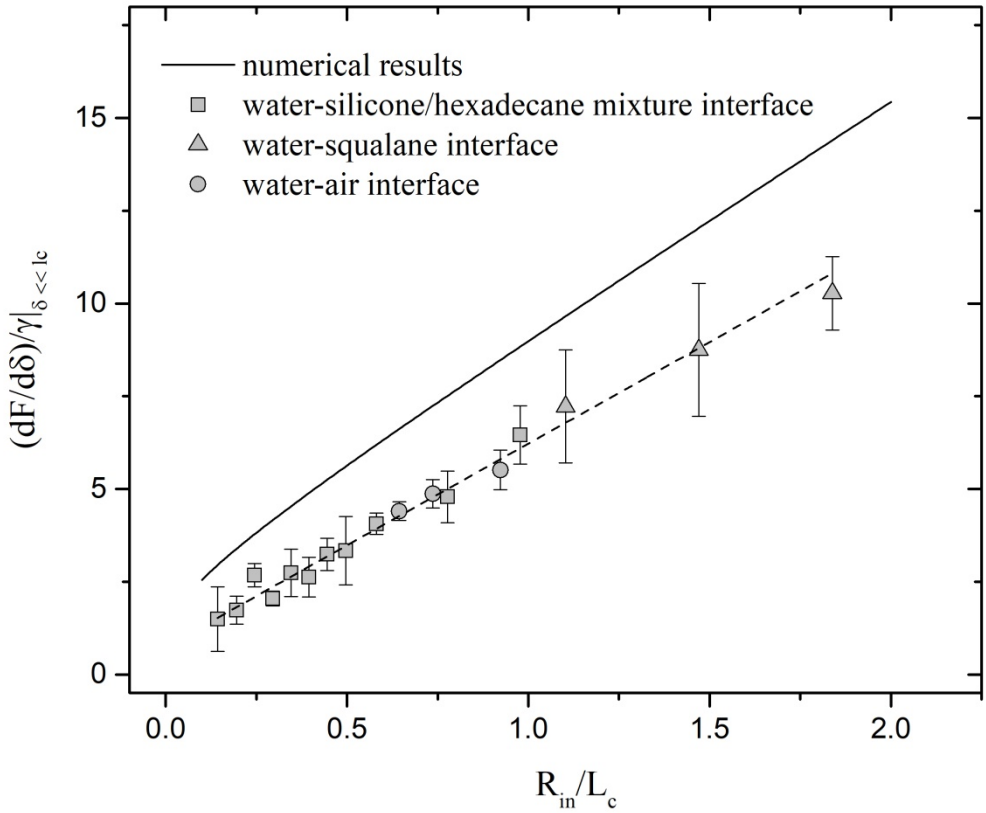

Figure 0.15 The derivative, dF/dδ, normalized by γ *vs*. R_{in}/l_c. These data are for the first plateau, when $\delta << l_c$. The solid curve is numerical result from Equation 3.4. The dashed line is a linear fit to the data.

We first focused on the lower plateau region in which the measured f was nearly a linear function of δ. Considering γ and l_c set the energy and length scale of the system respectively, we extracted the $df/d\delta$ values from different experiments, normalized by γ, and plotted them against R_{in}/l_c in Figure 3.15. The algorithm that we used to determine the $df/d\delta$ values is explained in Appendix A. It is clear that $(df/d\delta)/\gamma$ has a linear dependence on R_{in}/l_c. The dashed straight line in the figure is a linear fit to the data, which has a slope of 5.5 ± 0.3. To understand the linear relationship, we point out that the measured force applied by the indenter was balanced by the capillary and hydrostatic force. The first term comes from the fluid-fluid

interface pulling around the contact line on underneath particles; the second term is due to the pressure acting on the surface exposed to the lower fluid. The absence of quadratic component in Figure 3.15 suggests that it is the capillary force from those particles near the edge of the indenter that dominates the behavior of the system in the lower plateau region. Further by comparing to Equation 3.4 (solid curve in the figure), we found that measured slope on a particle raft was smaller than that of a clean interface with the same indenter. From top-view images, we know that when δ was small, the in-plane displacement of particles was negligible, and hence the change in $df/d\delta$ could not come from the rearrangement of particles and anyway it is not clear how rearrangement of particles in the raft could make the interface less stiff than the fluid interface. According to the calculation in Section 3.2.3, although we expect to have a smaller capillary force, if we modeled underneath particles as a pancake-shaped object subject to a boundary condition imposed by a cylindrical wall, such a geometry over simplified the real situation and thus is not a good approximation. A better way to model nearby particles is to represent the first ring of particles outside the indenter as a torus. However this would lead to an increase in the derivative of f with respect to δ, which contradicts with the experiment. It suggests that the boundary condition imposed by those nearby particles may not play a leading role in determining the behavior of system in the lower plateau region. In order to find out where the difference came from, we made a particle raft which had a size very similar to the size of the indenter, and repeated the measurement on the same water-air interface. Figure 3.15 shows that the f-δ curve for a small raft followed the same path of a large raft when δ was small. The result indicates that the network of contact line on the outermost particles under the raft was responsible for the small first-plateau value of $df/d\delta$.

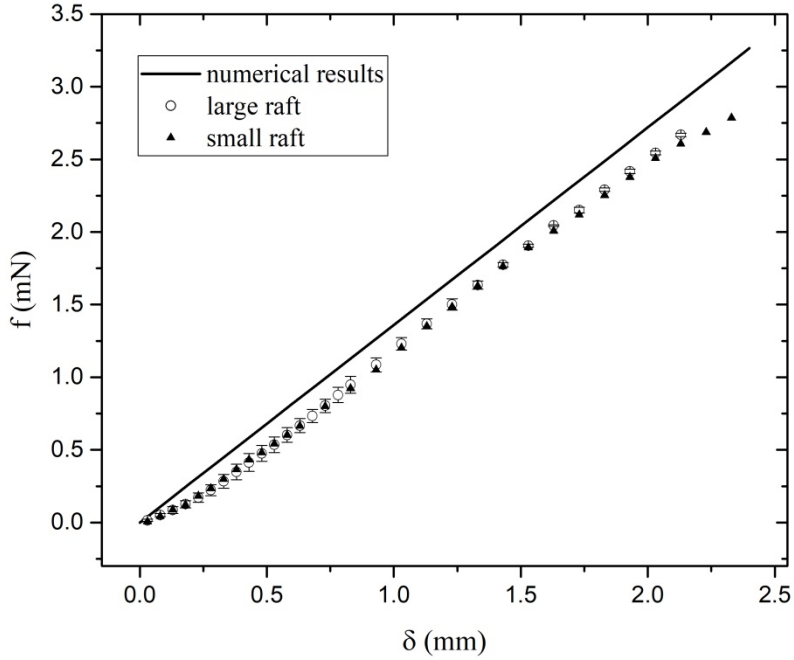

Figure 0.16 Measured force, f, versus indentation, δ, for particle rafts with different sizes. The small raft was similar in size to the indenter. The large raft was 60 mm in diameter, the size used for most of the experiments reported here.

A more interesting result Figure 3.16 reveals is that even for large δ, the presence of other floating particles made almost no change to the force curve. Moreover, the data points fall on a straight line that is parallel to the numerical results from Equation 3.5. It indicates that as long as the system reached the second plateau region, its response was dominated by capillary forces, and the effects associated with the elasticity of the lattice were negligible.

To further explore the stiffness of the rafts in the regime of intermediate δ, the average value of $df/d\delta$ in the upper stable region normalized by γ was plotted against R_{in}/l_c for different experiments in Figure 3.17. The solid curve in the plot is a polynomial fit to the data of order two. The coefficient of the quadratic term is 3.78 ± 0.5, which is close to π. From Equation 3.1, we know that the contribution coming from hydrostatic force is $\pi\gamma\tilde{R}^2\delta$, which is proportional to the square of $\tilde{R} = R_{in}/l_c$, and has a constant coefficient of π. It implies that the

quadratic term arises from attributed to the hydrostatic pressure, which equals the weight per unit area of liquid being displaced.

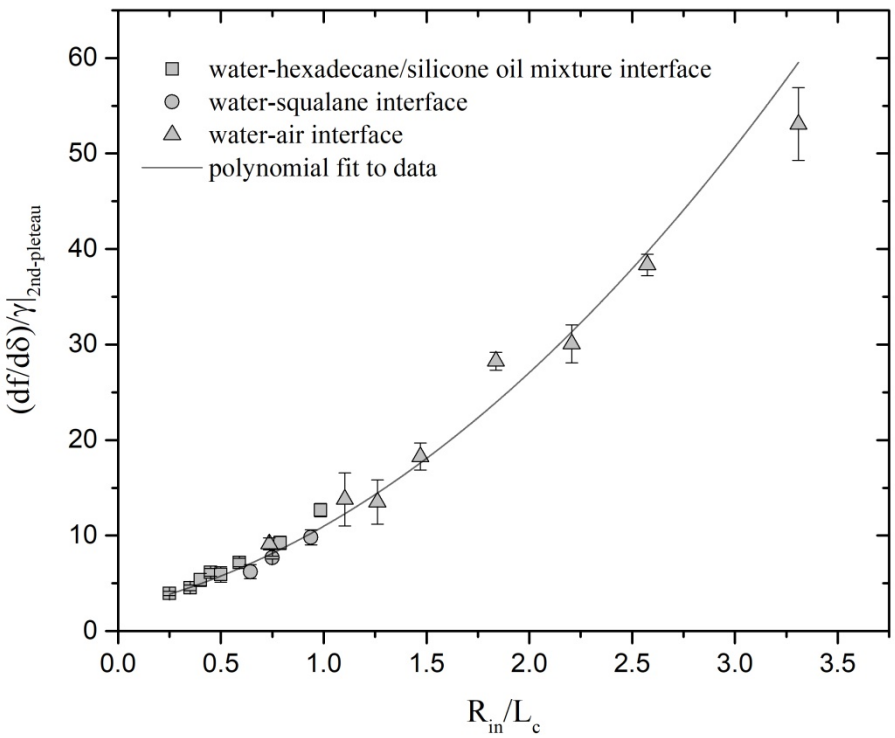

Figure 0.17 The derivative of the vertical component of force with respect to δ, normalized by γ *vs*. R_{in}/l_c for the second plateau region. The solid curve in the plot is a polynomial fit to the data of order two.

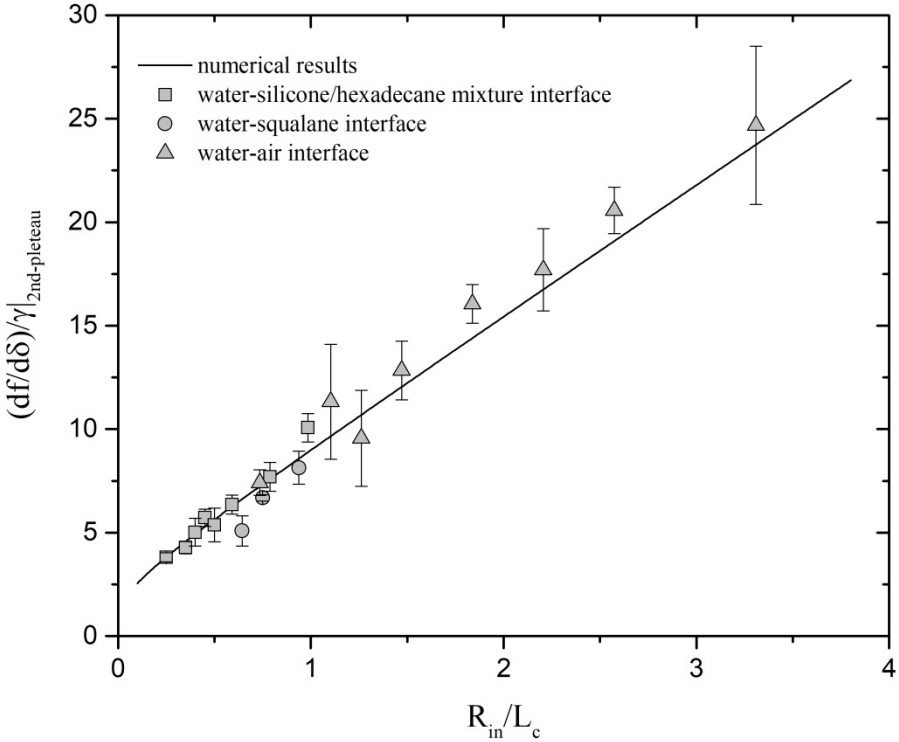

Figure 0.18 The derivative of the vertical component of force with respect to δ, normalized by γ *vs*. R_{in}/l_c for the second plateau region with hydrostatic effect subtracted. The solid curve in the plot is the numerical result from Equation 3.4.

To isolate forces at the interface, we subtracted the hydrostatic term $\pi\gamma\tilde{R}^2$, and replotted the data in Figure 3.18. The solid black curve is the numerical results from Equation 3.4. We find that most of the data points fall on the theoretical curve, which suggests that the particle raft behaves in a way that is indistinguishable from a capillary interface. In other words, the response of the system to a local mechanical load is fluid-like rather than solid-like. This is an important result of these studies.

The fact that the particle raft does not contribute to the stiffness of the interface may seem counterintuitive. Indeed, at the start of these experiments, we anticipated that the particles would make the interface stiffer owing to the forces between the particles. The rafts reported here are

cohesive, as shown by the fact that they maintain their size and shape when left alone at the interface. We therefore turn to the question of why a cohesive particulate layer would have no effect on the stiffness against poking.

As we mentioned earlier the deeper the indenter went, the more the interface was stretched in the radial direction. Owing to the lateral capillary force, all nearby particles tended to be pulled towards the center. From geometric considerations, we know that the projected circumference decreases when approaching the indenter. Hence there existed a finite azimuthal compression in the raft as a function of radial distance. Considering the huge cost of deforming particles, a possible way to relax the azimuthal compression is to form wrinkles as in an elastic sheet [64]. However, in all our experiments, no noticeable buckling of the particle raft was observed. Instead, from top-view images (Figure 3.9), we see that particles in certain directions would squeeze inward to make room for others, and hence allow azimuthal compression. This is because the cohesive energy to maintain the structure of the lattice is small comparing to the energy cost to bend the interfacial monolayer. Although the raft was initially in a jammed state, the radial stretching caused by indentation made it possible for particles to move around, and thus the behavior of the interfacial monolayer is dominated by capillary rather than elasticity.

Figure 19 shows how the separating the particles along the radial direction allows azimuthal compression. Consider an indenter that covers 7 particles, as in Figure 19(b). As these particles are pushed downward, the next row of particles gains some space in which to move. The six particles that have arrows drawn on them can freely move radially inward without approaching closer to their neighbor particles. Once these particles move, their neighbors can get closer to the origin and also move in the azimuthal direction (Figure 19(c)). Both of these motions result in compression in the azimuthal direction.

However, the above argument does not apply to the case when the size of the indenter was smaller than the diameter of a single particle. As illustrated in Figure 3.19(a), if only one particle was indented, we would punch a hole in the raft without affecting the structure of the lattice because of the jamming: none of the neighboring particles is free to move radially inward. In such situation, we would get a similar force curves as what was discussed in Chapter 2.

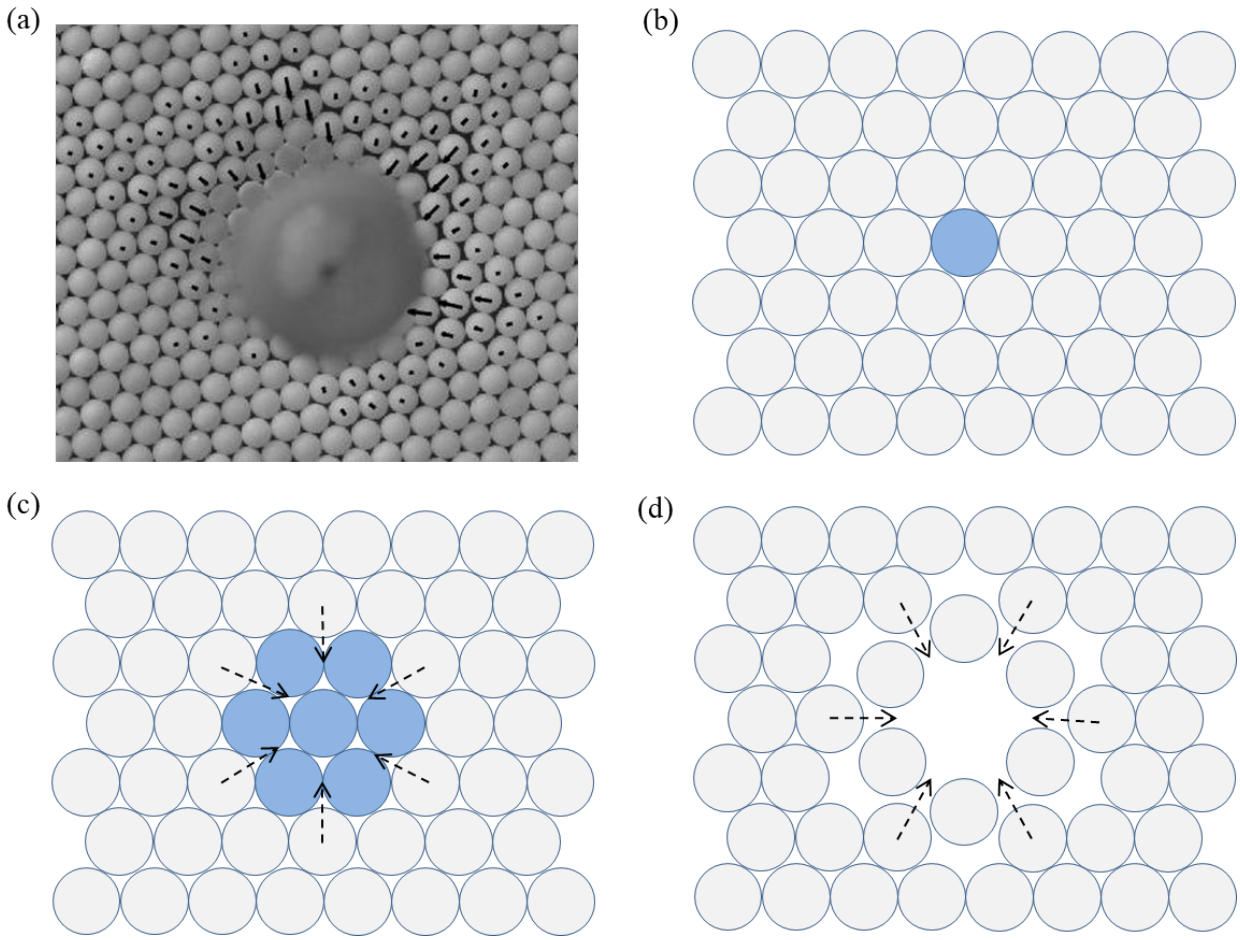

Figure 0.19 Image of PTFE particles with a = 0.79 ± 0.05 mm, R_{in} = 4 mm, and δ/l_c = 0.55 mm, which is in the second plateau regime (position #5 of Fig. S3). Superimposed on the image are the particle displacements relative to the initial lattice. Displacement magnitudes are shown magnified by 10×. (b) Illustration of poking a single particle. (b) Illustration of poking on seven particles, showing that six particles (arrows) can easily move. (d) With further displacement, other nearby particles can move freely to accommodate azimuthal compression.

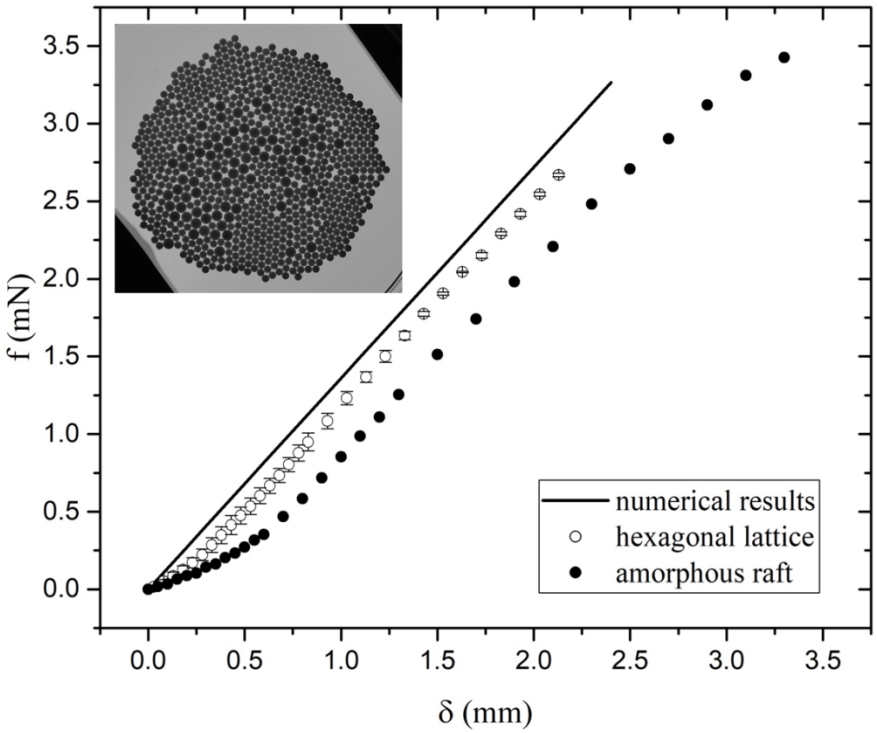

Figure 0.20 Measured force, f, versus indentation, δ, for a hexagonally packed lattice and an amorphous raft respectively. The inset is the top-view image of the amorphous raft.

The above experiments always started with a defect free hexagonal lattice. We now turn to tests of whether a perfect lattice structure is important in determining the behavior of the surface monolayer in the second plateau region. We prepared an amorphous raft by mixing Teflon spheres with two different sizes, and performed the experiment with the same indenter. Figure 3.20 shows the results of the force measurement, and its inset is the top-view image of the raft (different from the raft in the main panel of the figure because the raft had to be reconstructed after the indentation measurement). As expected, in a certain range of δ, the f-δ curve from an amorphous raft is parallel to that of a perfect lattice. Throughout the experiment no noticeable wrinkles were observed, and it is the radial dilation that accommodates the

azimuthal compression. The result indicates that the lattice structure plays no important role in the second plateau region. However, when δ is small, the two curves are quite different. This is because of the change of boundary conditions near the edge of the indenter. We repeated the measurement multiple times in different regions of the raft, and the shape of f-δ curves varied accordingly.

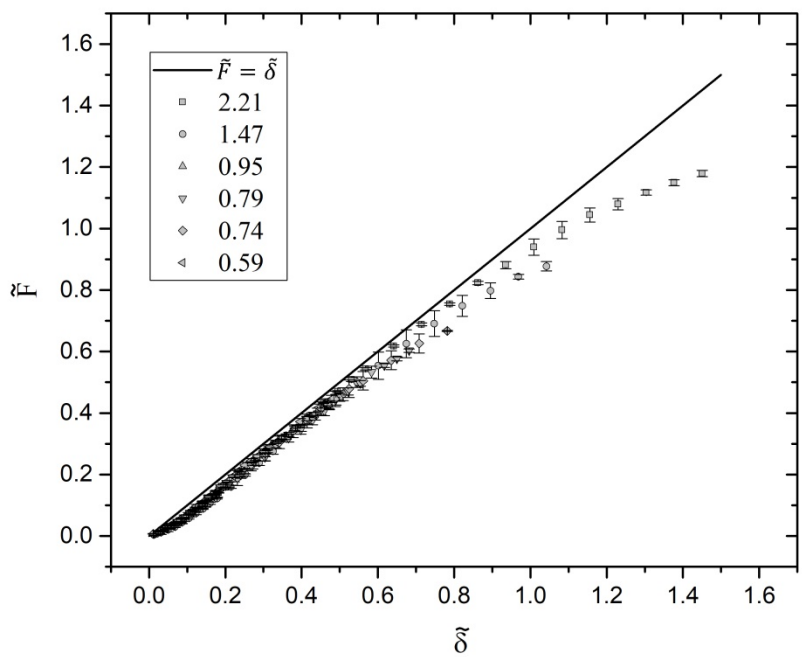

Figure 0.21 Normalized force-indentation curves for various experiments. The solid straight line is the numerical results from Equation 3.5, which has a slope of 1.

To further test the similarity of the measured force and the capillary force at a clean interface, we normalized f-δ curves in Figure 3.13 by using the coefficient of Equation 3.5 and l_c. The dimensionless force and indentation can be expressed as

$$\tilde{F} = \frac{K_0(\tilde{R})}{\pi\tilde{R}^2 K_0(\tilde{R}) + 2\pi\gamma\tilde{R}K_1(\tilde{R})}\frac{f}{\gamma l_c} \quad (3.15)$$

$$\tilde{\delta} = \frac{\delta}{l_c} \quad (3.16)$$

Figure 3.21 shows the resulting $\tilde{F}$ - $\tilde{\delta}$ curves. We find that data obtained from different experiments with various combinations of parameters collapsed onto a series of parallel curves when the indentation was not too large. But after the indenter moved beyond the second plateau region, the slope of force curves would decrease as $\tilde{\delta}$ increased. Such a deviation was caused by the discontinuity of the interface induced by the finite thickness of the indenter. When the curvature on the edge of the indenter was large, nearby particles rolled up onto the indenter. This change would make the interface rise up a little bit and therefore reduce the tilt angle α, and hence reduced the measured force.

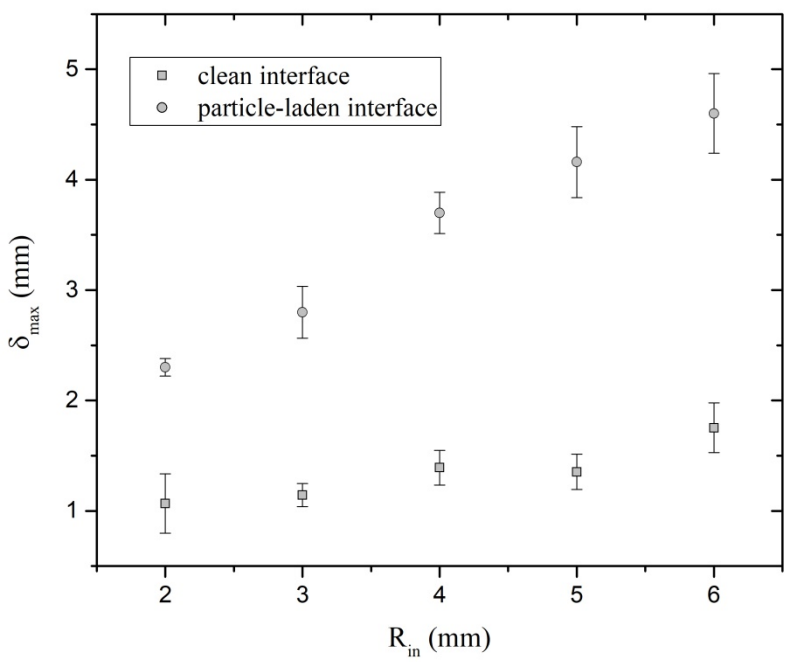

Figure 0.22 Maximum indentation before the rupture of the particle raft for different size of indenters at water-air interface.

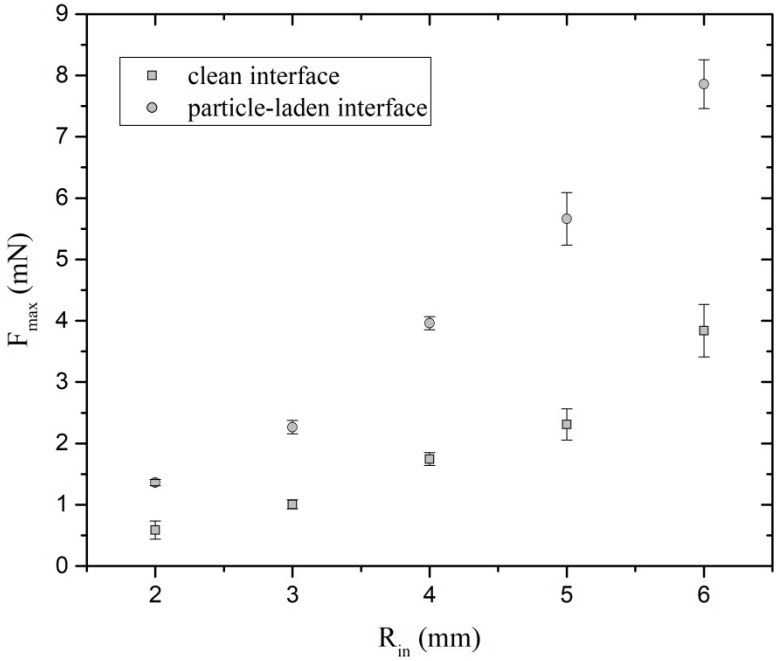

Figure 0.23 Maximum force before the rupture of the particle raft for different size of indenters at water-air interface.

Finally, we measured the maximum depth that the indenter could reach and the maximum force the raft could sustain before rupture. The measurements were obtained on water-air interface with a capillary length of 2.7 mm. In Figure 3.22 and 3.23, we plotted the maximum indentations and forces for different R_{in} on a Teflon particle raft. The results are plotted with the maximum indentation and force for the same indenter at a clean, particle-free interface. It is clear that in all situations, with the help of those particles, the interface was able to accommodate larger indentations and poking forces before rupture. In this way, the particle raft provides an effective mechanical protection to the interface.

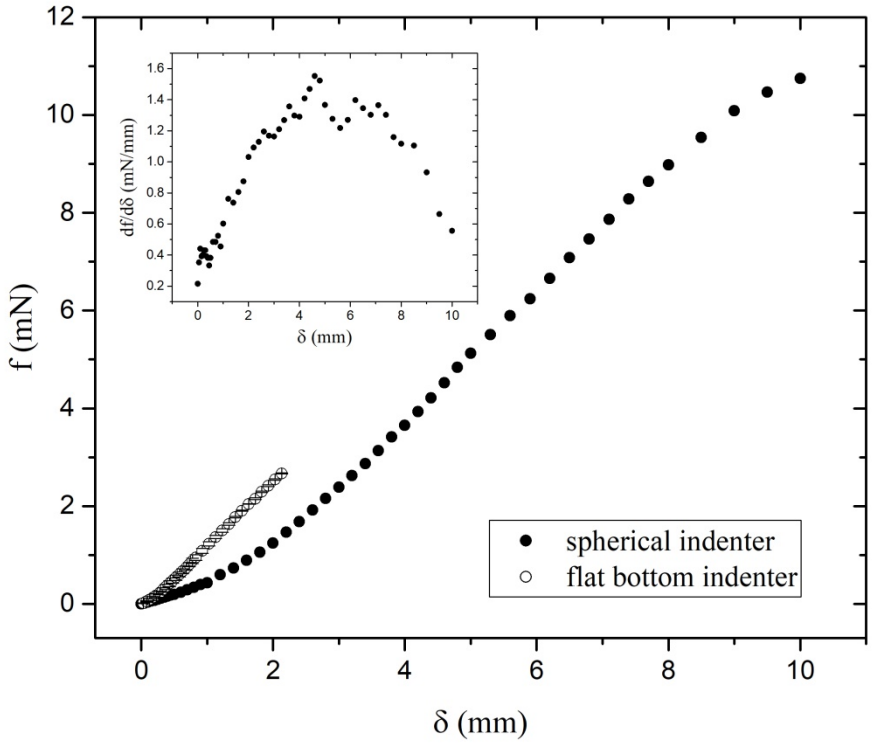

Figure 0.24 Measured force, *f,* verse indentation, δ, for a spherical indenter poking on a Teflon particle raft floating on a water-air interface.

3.5 Indentation with spherical indenters

In all the above experiments, flat bottom indenters were used to exert mechanical loads. It has the advantage of having fixed number of particles in non-slippery contact, which makes it easier to compare to theory. However, the major drawback is that the flat bottom breaks the raft at an early stage because of the discontinuity caused by the edge. On the contrary, the interface around a spherically indenter is smooth, and hence a much larger indentation can be reached before the rupture of the raft. As a tradeoff, the price we need to pay is that the number of contacts is changing throughout the experiment so that it may be more difficult to predict the f(δ) response.

Figure 3.24 shows the typical force measurement for a spherical indenter with a radius of $6.5\ mm$ poking on a Teflon particle raft floating on a water-air interface. The f-δ curve started with a small $df/d\delta$, and its stiffness kept increasing over a wide range of δ, which was presumably caused by the increasing number of particles in contact with the indenter. Then the f-δ curve entered a stable region, in which the slope was nearly a constant. This can be better visualized in the inset of Figure 3.24, which is a plot of $df/d\delta$ as a function of δ. Such a behavior suggests that there may exist an effective contact radius, and in this region the force response was not very different from its flat bottom counterpart. If δ kept increasing, the stiffness would drop again until the rupture of the particle raft. Different from the case of a flat bottom indenter, the rupture for a spherical indenter was usually caused by permeation of water through the gap among particles. As a comparison, those open circles are the results of a flat bottom indenter with a radius of $4\ mm$. It is clear that, without the constraint from the edge discontinuity, the spherical indenter can go far deeper than the flat bottom one with a same particle raft. Further, the two f-δ curves shared the same $df/d\delta$ in the second plateau region, which suggests the spherical indenter has an effective radius of $4\ mm$.

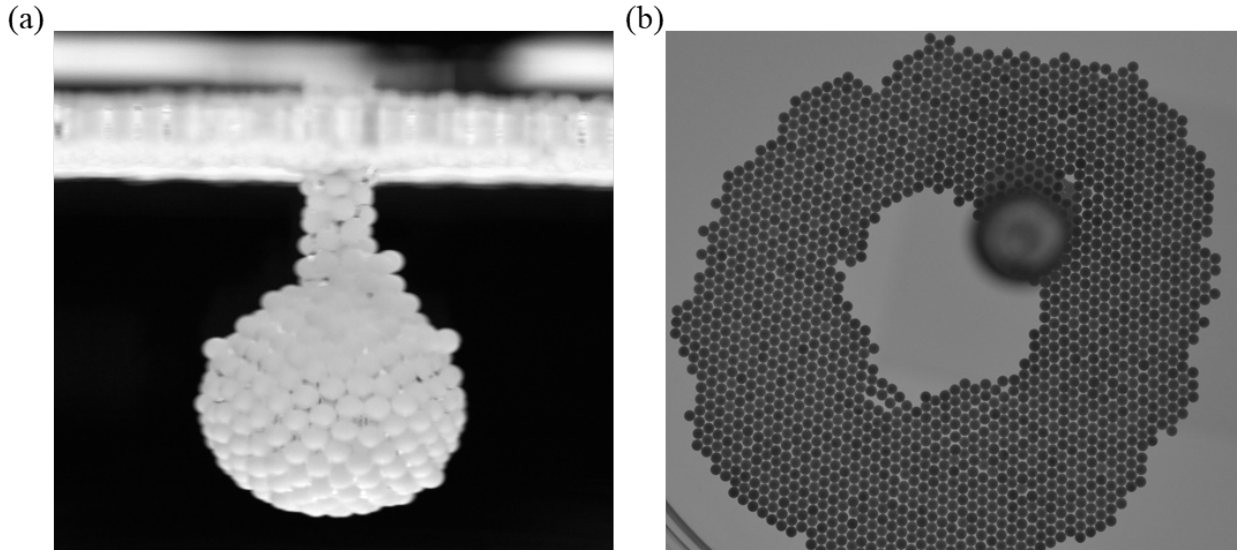

Figure 0.25 (a) A spherical indenter with a radius of 6.5 mm fully wrapped by Teflon particles. (b) Top-view image of the raft on a water-air interface.

In some experiments, it was even possible to wrap the entire sphere with particles. Figure 3.25 (a) shows a side-view image of an indenter coated by Teflon particles. The indenter has a radius of 6.5 mm, and was initially placed above the particle raft. In process of indentation, nearby particles were continuously pulled towards the center and wrapped the indenter, which left a hole in the original raft as shown in Figure 3.25 (b). This phenomenon raises an interesting question: what is the largest spherical indenter that can be fully wrapped by a particle raft.

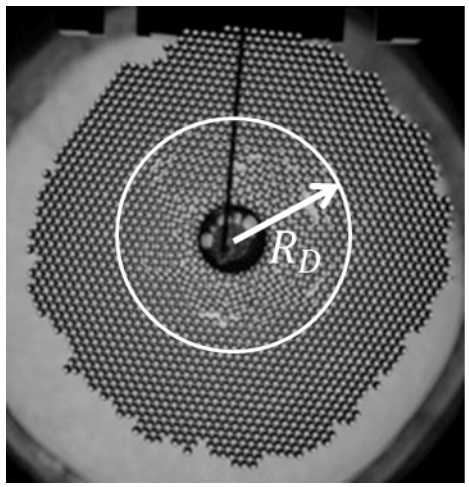

Figure 0.26 Illustration of the radius of the region, R_D, affected by indentation.

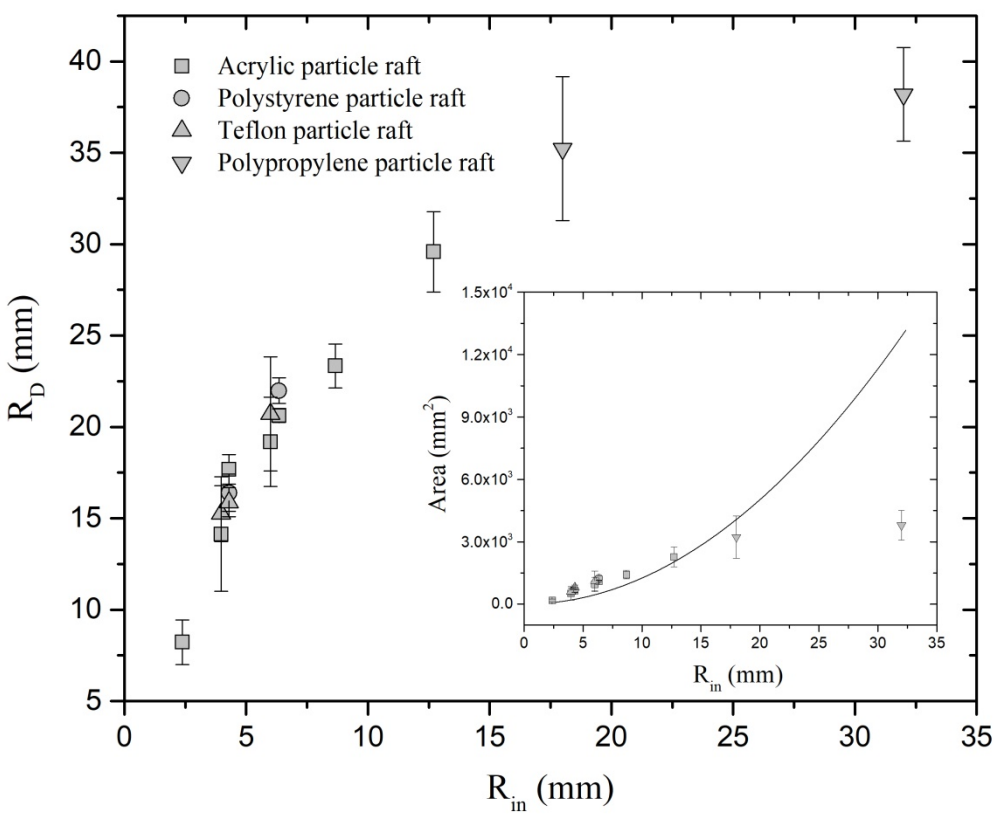

Figure 0.27 The radius of the region affected by indentation plotted against the radius of the indenter for different kinds of particle rafts. The inset is the area of affected region as a function of indenter radius.

To address the question, we measured the size of the region in which particles were pulled towards the center. Specifically, the radius of the this region, R_D, is defined as the distance from the center of the raft to the farthest particle beyond which the lattice structure is perfect (Figure 3.26). All experiments were performed on water-air interfaces but with different combinations of particle rafts and indenters. The radius of the indenter varies from 2.38 mm to 31.75 mm, and four different kinds of particles were used to make rafts: acrylic (a = 0.79 mm), polystyrene (a = 0.79 mm), Teflon (a = 0.79 mm) and polypropylene (a = 1.59 mm). Figure 3.27 plots the R_D, as a function of R_{in}. We find that for the same indenter, the difference caused by particle species was negligible. Also, as expected, R_D increased when R_{in} got larger. The inset of Figure 3.27 plots the area of affected region against R_{in}, and the solid curve is the surface area of the indenter. The existence of a crossover of the two curves suggests there is a limit for the size of the indenter that can be fully wrapped by a particle raft. However, these results are not fully understood yet (more details are covered in Appendix C). This remains an area for future investigations.

3.6 Summary

In summary, we measured force response of a particle raft floating on liquid/gas or liquid/liquid interfaces under a normal indentation. We showed that there exist two linear regions. When $\delta << l_c$, in the lower plateau region, the interfacial monolayer shows a reduced stiffness due to the boundary condition imposed by particles under the indenter. This low-stiffness regime persists over a range of indentations less than l_c. The stiffness is approximately $5.5\gamma(R_{in}/l_c)$ for all systems studied. in the higher plateau region, the particulate assembly has the same stiffness as a pure liquid interface, which suggests the fluid-like response under normal force. Further, from top-view images, we showed that, as long as the indenter was larger than the size of a single particle, the azimuthal

compression can be relaxed through the in-plane rearrangement of particles, and wrinkles were not observed in all our experiments. At still deeper indentation ($\delta \sim l_c$), the stiffness decreases owing to the particles moving up around the corner of the indenter, Overall, we found a non-intuitive result that the interface stiffness is equal to or less than that of a clean fluid interface. Although the presence of floating particles at an interface does not change its capillary nature under a wide range of poking depth, the existence of the particle raft makes the original interface tougher in terms of both the maximum force it can sustain and the largest indentation an indenter can reach. Although the experiments were performed on millimeter-scale particles, the fact that the results do not rely on gravity means that results can be applied to micron- or nanometer-sized particles.

CHAPTER 4

FORMATION OF TWO DIMENSIONAL SHEETS IN AQUEOUS PHASE

In this chapter, we discuss an approach to interfacial adsorption of particles for the purpose of repairing damaged surfaces or enwrapping droplets, cells, or other targets in suspension. Our approach relies on ultra-thin solid sheets suspended in an aqueous phase. Because these sheets are just a few nm thick, even a small volume concentration results in a large surface area per volume (more so than with spherical particles). If these sheets bind to an exposed liquid-liquid interface such as a droplet, then they could form an elastic film at the interface, which could make the interface impermeable and perhaps rigid. The inspiration for this work comes from recent experiments by other research groups at the University of Massachusetts Amherst in the Physics and Polymer Science and Engineering departments, showing that polymer films a few nm in thickness can effectively wrap droplets and lead to predictable and controlled shapes [69-71]. In the previous work, these sheets were made by spin coating. Here, we describe work on making sheets as thin as 4 nm in large quantity by means of a self-assembly process. Various molecular designs, protocols for driving the self-assembly of sheets, and images of the self-assembled sheets in suspension are described.

4.1 Introduction

Two dimensional materials are structures that have a thickness at atomic or molecular level, while the other two dimensions are much larger than the thickness [72, 73]. The success in exfoliation of graphene in 2004 by Novoselov and Geim proved that it is possible to have stable 2D crystals in experiments [74], and it triggered a proliferation of interests in related research.

Since then, a variety of 2D materials, such as transition metal-dichalcogenides and hexagonal boron-nitride, have been discovered [75]. Meanwhile, progress has also been made in fabrication [76, 77]. Commonly used methods include the mechanical exfoliation, chemical vapor deposition, templated synthesis, self-assembly and liquid-phase exfoliation.

Owing to their superior mechanical, optical and electrical properties, 2D materials have enormous potential in applications ranging from electronics and optoelectronics to biomedicine and biological engineering [78-80]. Although many efforts have been made towards designing special structures for different purposes, the research for organic 2D materials is still in its early stage [81, 82]. Comparing to inorganic 2D materials, the advantage of organic counterparts lie in their flexibility, which enables the fine tuning of certain properties to meet the requirement of applications in various field.

Recently, collaborators in the group of Professor S. Thayumanavan of the University of Massachusetts Amherst Chemistry department have reported a simple strategy to prepare smart organic 2D material in aqueous media [83]. They synthesize organic molecules that take advantage of multiple supramolecular (intermolecular) interactions in a collaborative fashion to form desired structures by non-interfacial assembly of molecules at room temperature. Owing to its molecular level of thickness, it is possible to suspend a large amount of surface area per unit volume in stable suspension, and hence has the potential for applications like crack repairing through adsorption and drug delivery via wrapping.

Various methods, such as transmission electron microscopy (TEM), high-resolution TEM (HRTEM), scanning electron microscopy (SEM), and atomic force microscopy (AFM), have been used to characterize the sample. The results confirmed the existence of 2D sheets, and showed that their thickness is on the single molecular level. However, all characterizations so far

were performed on dry samples that were attached to a substrate such as a TEM grid. This leaves open questions such as how do 2D sheets behave while suspended in aqueous phase, do they grow in suspension or at surfaces, and is the adhesion strong enough to wrap particles, and so on.

In this chapter, we show the possibility of direct observation of organic 2D sheet in aqueous phase through optical microscopy under dark-field illumination. This method provides an effective way to study and better understand the properties of those sheets. We also discuss the protocols for forming the sheets in solution. The work in this chapter was done in collaboration with T. M. K. Yehiya, Z. Jiang and S. Thayumanavan.

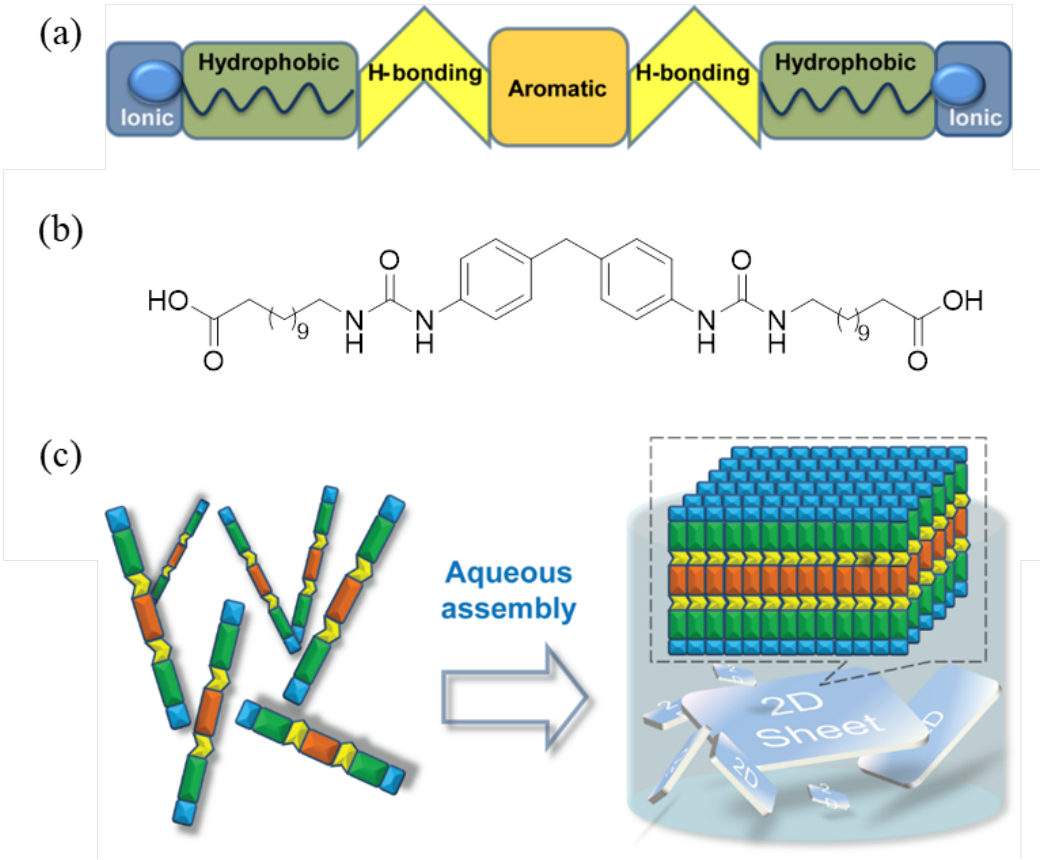

Figure 0.1 (a) Illustration of the molecular design containing four complementary intermolecular interactions. (b) Chemical structure of a bola-amphiphilic molecule. (c) Illustration of the formation of organic two-dimensional materials.

4.2 Material and sample preparation

Figure 4.1(a) shows the multiple noncovalent interactions in the molecule responsible for the 2D sheet morphology. As illustrated, the urea-based aromatic rings are connected to two hydrophobic alkyl chains. At the end of each alkyl chain there is an ionic head group. Figure 4.1(b) is the corresponding chemical structure of the molecule. Such design incorporates four complimentary intermolecular interactions. The attractive forces among molecules come from the hydrogen bonding interactions provided by the urea unit, π-π stacking interactions between aromatic rings and the hydrophobic interactions due to the alkyl chain. On the other hand, the repulsive forces originate from the electrostatic repulsions owing to the ionic head groups at the termini. As illustrated in Figure 4.1(c), due to the subtle balance of four interactions, aqueous assembly can be achieved under appropriate conditions. The role of each of these component has been studied extensively through building up structures that provide specific cues about each of them in detail [83].

To prepare the sample, we followed the general procedure describe in [83]. Firstly, 1 mg of bola-amphiphilic molecules (synthesized by T. M. K. Yehiya in Thayumanavan's group) were added to 200 μL of dimethyl sulfoxide (DMSO). Since those molecules have a poor solubility, an ultrasonic bath (Branson 3510 ultrasonic cleaner) was used to further disperse them in DMSO for 90 min. If not dissolved properly, large amounts of aggregates would form in later steps, which we confirmed by imaging with an optical microscope. The mixture was then slowly injected to the bottom of a 20-mL glass vial containing 5 mL of de-ionized (DI) water. The inverse addition method has also been tested, but it did not improve the formation of sheets in terms of their size and the amount of aggregates as well. Finally, the obtained suspensions were kept at room temperature without stirring to allow the assembly of molecules in water. We found

that it took at least 72 hours to form sheets which were large enough to be seen under optical microscope. Once formed, those sheets are stable for at least four months at room temperature, but no noticeable growth was observed during that period of time.

Another factor that might affect the formation of 2D sheets is the pH value. We prepared samples with pH values of 4, 6, 7, 8 and 10 respectively. Although 2D structures were found in all cases, large sheets that have a size of tens of microns were only available in pH 7 suspensions.

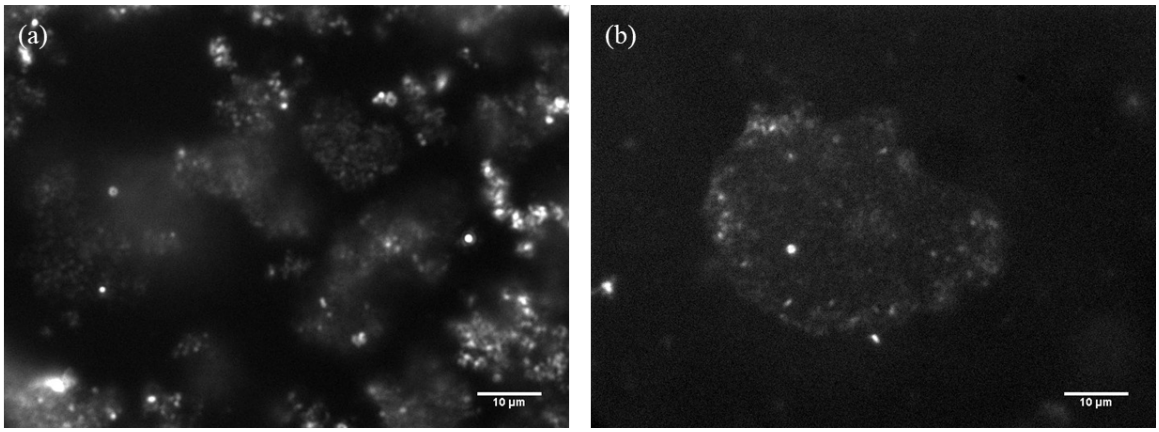

Figure 0.2 (a) Dark field image of a typical sample before heating. (b) The same sample under microscope after heating at 80C° for 3 minutes.

In a typical sample, there exists a large amount of aggregates, which makes it difficult to find sheets under optical microscope. In order to reduce the amount of aggregates, in some experiments, the sample was heated on a hot plate (Corning 6795-220 stirring hot plate) at $80C°$ for 3 minutes, and then cooled down to room temperature. We found that under these conditions aggregates would break down, while the 2D structures remained stable (Figure 4.2).

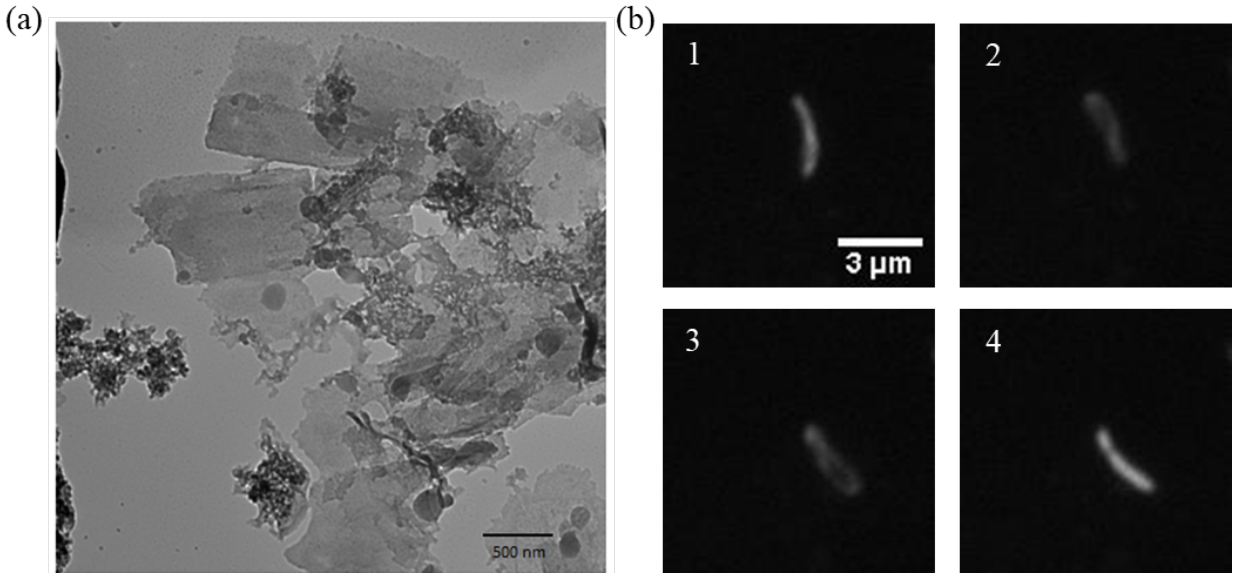

Figure 0.3 (a) TEM image of the dry sample taken by T. M. K. Yehiya. (b) A piece of sheet peeled off from the TEM grid by rehydrating.

4.3 Direction observation under optical microscopy

Once the sample was ready, TEM images were first used to verify the existence of 2D sheets. After that the sample was further characterized by an optical microscope. Since these sheets are extremely thin, they are almost transparent under traditional optical microscope. In order to increase contrast, dark-field illumination was used as the main imaging method. Under dark-field mode, directly transmitted light is excluded from the objective, which results in a dark background; meanwhile scattered light is collected and displayed as bright spots. This gives us extra contrast on edges, which enables us to catch possible 2D sheets. However the cost we need to pay is that the internal details might be lost. In dark-field images, aggregates are usually shown as bright clusters, because of their rough surface. On the contrary, smooth 2D structures should only have bright edges with its center region being almost as dark as the background.

Figure 4.3(a) is the TEM image of a typical sample taken by T. M. K. Yehiya using an FEI TECNAI 12 transmission electron microscope operating at 200 kV. It shows that 2D sheets

have been formed by bola-amphiphilic molecules. The same TEM grid was then transferred to a glass coverslip (#11/2, 22×50 mm rectangle, VWR cat. no. 48393-194), and rehydrated by adding a droplet of DI water on top of it for further analysis with optical microscope.

An optical microscope (Zeiss Axiovert 200) equipped with a dark-field condenser (Carl Zeiss Dry dark-field condenser 0.8/0.95 (0.6-0.75) WD=6.0mm # 445323) was used to characterize the rehydrated sample. Since 2D sheets were extremely thin, even with enhanced contrast under dark-field mode, it was difficult to locate them in solution. An empirical strategy is to stay close to the top of the bottom coverslip and scan very slowly waiting for the rotation of tiny sheets. In the rehydrated sample, small sheets which have a size of a few microns were found by using a 100x objective (Zeiss 100x oil iris 1031-173) with an aperture of 0.7. Figure 4.4(b) shows four different moments of a single piece of sheet in aqueous phase, undergoing Brownian motion. When it was parallel to the substrate (2 and 3), it looked like an oval; but when it was perpendicular to the objective, we only saw a bright curve whose width was limited by the diffraction limit of the microscope. Although we could not measure the absolute thickness of the sheet, which could still be way beyond the molecular level, such behavior suggests that its third dimension is much smaller than the other two, and we call such structures 2D sheets in a broad sense. Furthermore, the fact that we imaged these sheets just after they were seen in the TEM indicates that they are the same structures, and also that they can be resuspended in water after being dried in a vacuum.

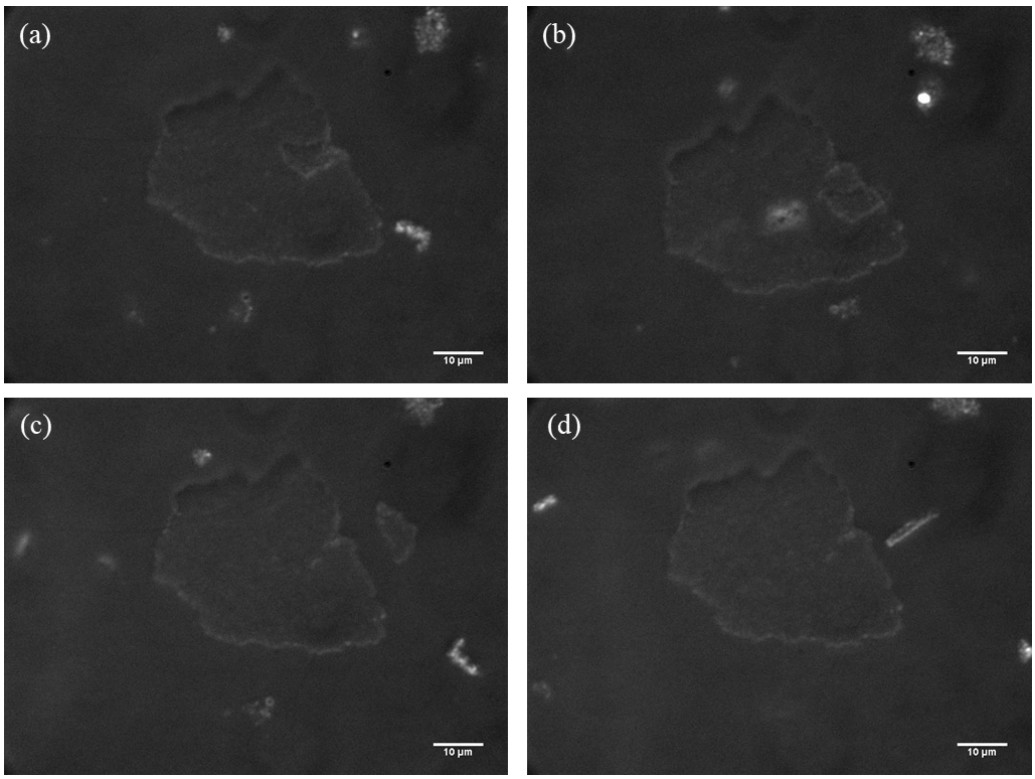

Figure 0.4 Observed 2D structures in microscope under dark field illumination. (a) and (b) A small 2D sheet sitting on top of a large one. (c) and (d) The rotation of the small piece.

In the process of rehydrating a dry sample, only sheets of a few microns were observed. However, large sheets with a size of tens of microns were also found in other experiments, in which suspensions were injected into a chamber (CoverWell Perfusion Chambers 3mm×32mm×0.6mm, #622503) for further characterization. In Figure 4.4 (a), we can see that there were two sheets laying parallel to each other, but they did not stick together. As time passed by, the small sheet drifted away from the large one (by Brownian motion), and never came back after that (Figure 4.4 (b) and (c)). It indicates that stacking was not preferred by sheets because of the likely electrostatic repulsion provided by the ionic head groups. The existence of charge repulsion was further supported by a pilot wrapping experiment, in which negatively charged silica particles with a diameter of $1.4\,\mu m$ were added to the sample. However, no attractive interaction was observed in all cases.

Further, similar to the rehydrating experiment, the rotation of small sheet was observed in Figure 4.4(d). The rod-like shape next to the large sheet was the small one in its vertical orientation. And it is clear that its width was much larger than the thickness. However, the rotation or bending of the large sheet was never detected in experiment.

4.4 Summary

In summary, we optimized the condition for the formation of two dimensional sheets in aqueous media. We directly observed 2D structures under optical microscope with dark-field illumination, and found stacking was not preferred by sheets. By using these sheets, a pilot experiment of wrapping has been conducted. But no attractive interaction was found between sheets and negatively charged silica particles with an average size of $1.4\mu m$. As for positively charged particles, emulsions or vesicles, it remains an area for future investigation.

APPENDIX A

DETERMINE THE SLOPE OF FORCE CURVES IN LOWER LINEAR REGION

The goal of this step is to extract slopes of force curves from different experiments consistently. We used the following algorithm to determine the range of the lower linear region, and hence the slope can be obtained by a linear fit of corresponding data points.

1. Pick the first a few data points and fit a linear model
2. Predict the force for next indentation and calculate its prediction interval by using the model obtained in first step
3. If the measured force is in the prediction interval, then include this data point in the dataset, refit the linear model and repeat step 2; if not, stop

All those data points used to fit the last linear model are considered to be in the lower linear region. And the slope of the force curve is the coefficient of the regression.

APPENDIX B

EXAMPLE OF STRAIN FIELD FOR A PARTICLE RAFT

The calculation of strain field is based on the displacement of particles. The two plots below show the strains for a PTFE particle raft at water-air interface in radial and azimuthal directions respectively. In the plots, blue indicates compression, while red corresponds to the stretching.

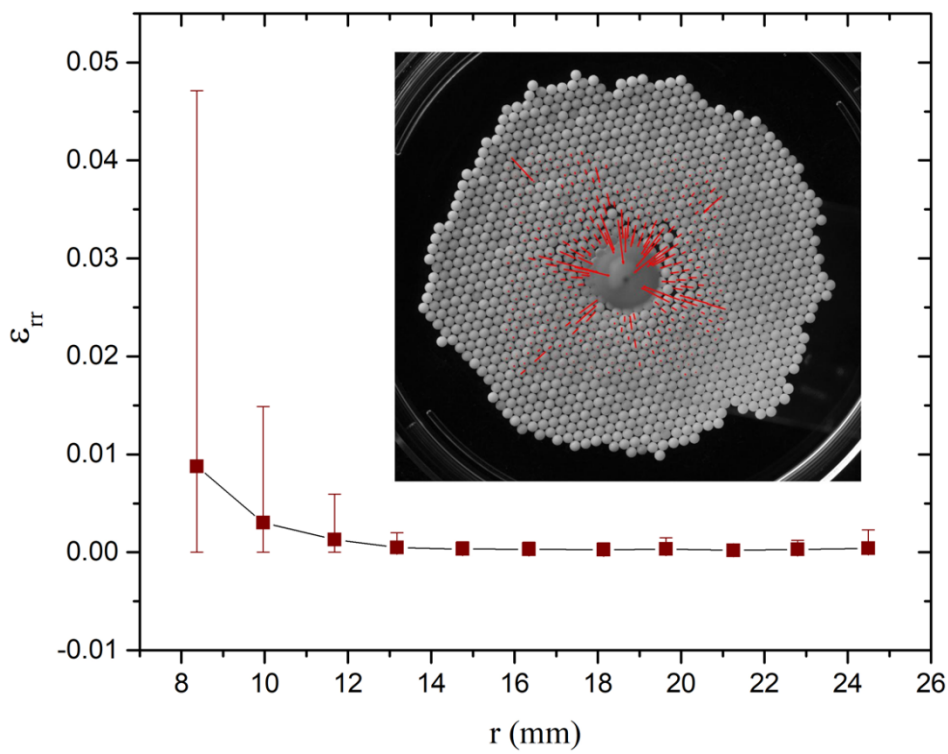

Figure B.1 Radial strain, ε_{rr}, magnified by a factor of 50 as a function of radial distance, r, for a PTFE raft. The inset plots the strain on top of particles.

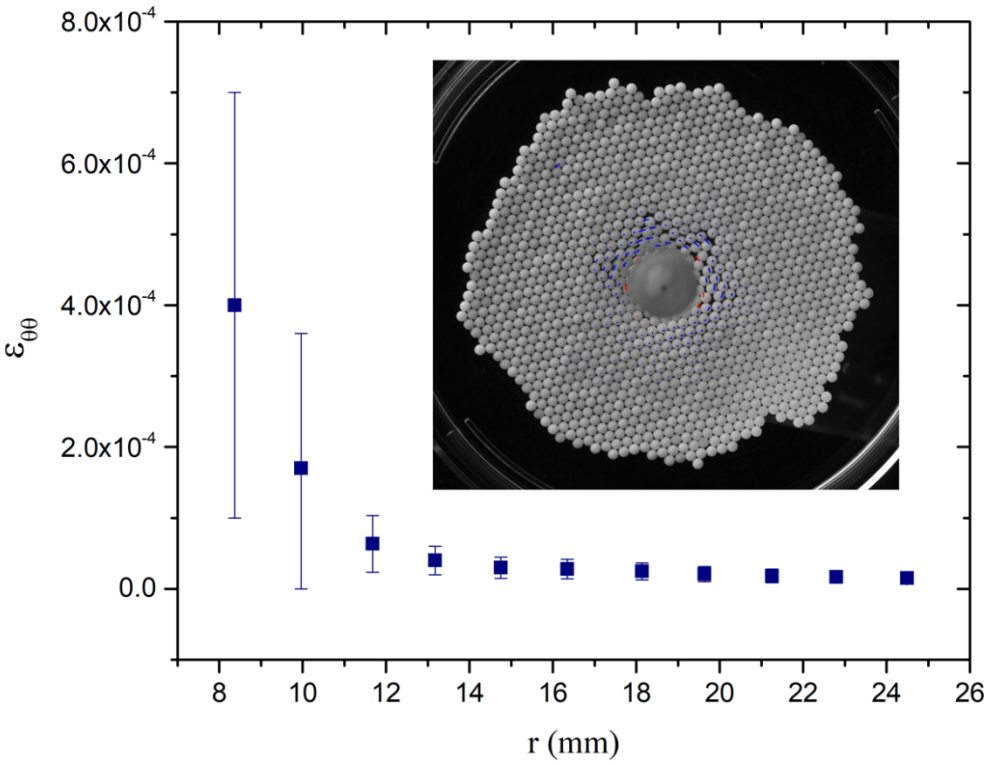

Figure B.2 Azimuthal strain, $\varepsilon_{\theta\theta}$, magnified by a factor of 50 as a function of radial distance, r, for a PTFE raft. The inset plots the strain on top of particles.

APPENDIX C

WRAPPING OF A SPHERICAL INDENTER BY USING PARTICLE RAFTS

Material

Polymer spheres were used to form rafts at water/air interfaces. These particles were all purchased from McMaster-Carr and Engineering Laboratories INC.: acrylic (R = 1/16" radius, cat. no. 1383K42), high-impact polystyrene (R = 1/16", cat. no. 9374K21), chemical-resistant polypropylene (R = 1/16" radius, cat. no. 1974K2) and polytetrafluoroethylene (R = 1/32").

For indenters, polytetrafluoroethylene and polypropylene spheres ranging from 2.38 mm to 31.75 mm were used in most experiments. Occasionally, hydrophilic spheres such as acrylic ones also served as indenters. We find that the hydrophobicity of the indenter does not affect the result much, while the hydrophobicity of floating particles plays an important role in determining whether the indenter can be fully wrapped or not.

The liquids used in the experiments were deionized water (Milli-Q plus) with a tabulated surface tension of 72 mN/m and squalane with density of 0.81 g/mL (Sigma-Aldrich, cat. no. 234311). Fluids were held in glass crystallizing dishes (KIMAX, cat. no. 23000 or PYREX, cat. no. 3140).

Procedure

In all experiments, solid particles were first placed on water/air interface by hand. Then, we manually rearranged them to form a defect free lattice with a shape as circular as possible. The indenter was initially hanging above the particle raft. We gradually lowered it in vertical

direction via a translation stage. The increment per step varied from 0.2 mm to 0.5 mm, which depends on how large the indenter is. The experiment continued until the indenter was either fully wrapped by particles or wetted by water. Throughout the process both top-view and side-view images were taken by two digital cameras.

Preliminary results and future experiments

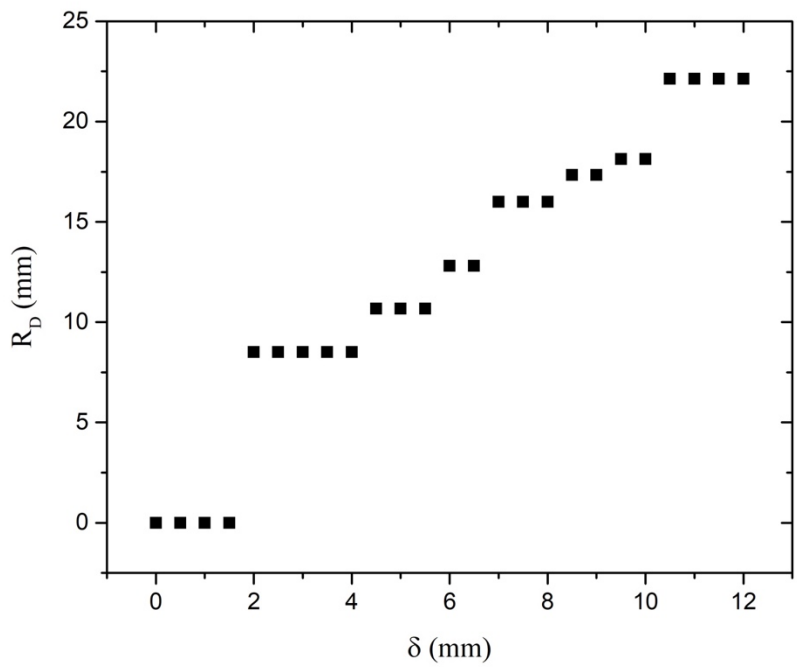

Figure C.3 R_D as a function of δ for a Teflon particle raft floating on the surface of water.

The main question we would like to address is under what conditions it is possible to fully wrap a spherical indenter by a particle raft. Based on the results of previous indentation tests, we know that only particles in a small star-shaped region near the indenter would be pulled towards the center. Therefore, whether wrapping can be achieved or not depends on the size of the star-shaped pattern, R_D. This naturally leads to the question that what sets the limit of R_D in a typical experiment.

Figure C.3 plots R_D as a function of δ for an experiment performed on a water/air interface. The indenter was an acrylic sphere with a radius of 6.5 mm, while the particle raft was made up of Teflon particles with radius of 0.8 mm. It is clear that R_D increased as δ got larger, however, the results look like step functions rather than a continuous one due to the discrete natural of the system. Although R_D has a dependence on δ, a proper scaling law has not been discovered yet. To further explore the wrapping process in the future, more experiments with different combinations of parameters are needed. Those parameters include particles/indenter size, raft radius, capillary length and hydrophobicity of particles. In designing experiments, we suggest to use hydrophobic particles as floating ones, and set the raft size to be at least one order of magnitude larger than the radius of the indenter.

BIBLIOGRAPHY

1. Zeng, C., H. Bissig, and A.D. Dinsmore, *Particles on droplets: From fundamental physics to novel materials.* Solid State Commun., 2006. **139**: p. 547-556.

2. McGorty, R., et al., *Colloidal self-assembly at an interface.* Mater. Today, 2010. **13**: p. 34-42.

3. Binks, B.P., *Particles as surfactants -- similarities and differences.* Current Opinion in Colloid and Interface Science, 2002. **7**: p. 21-41.

4. Binks, B.P. and T.S. Horozov, *Colloidal Particles at Liquid Interfaces*. 2006, Cambridge: Cambridge University Press.

5. Lin, Y., et al., *Nanoparticle Assembly and Transport at Liquid−Liquid Interfaces.* Science, 2003. **299**: p. 226.

6. Pieranski, P., *Two-Dimensional Interfacial Colloidal Crystals.* Phys. Rev. Lett., 1980. **45**: p. 569.

7. Binks, B.P. and R. Murakami, *Phase inversion of particle-stabilized materials from foams to dry water.* Nat. Mater., 2006. **5**: p. 865-869.

8. Koretsky, A.F. and P.M.I. Kruglyakov, *Emulsifying effects of solid particles and the energetics of putting them at the water-oil interface.* Izv. Sib. Otd. Akad. Nauk. SSSR Ser. Khim. Nauk, 1971. **2**: p. 139-141.

9. Pickering, S.U., *Emulsions.* J. Chem. Soc., 1907. **91**: p. 2001.

10. Pike, N., et al., *How aphids lose their marbles.* Proc. R. Soc. Lond. B, 2002. **269**: p. 1211-1215.

11. de Gennes, P.G., F. Brochard-Wyart, and d. Quéré, *Capillarity and Wetting Phenomena: Drops, Bubbles, Pearls, Waves*. 2004, New York: Springer.

12. Eral, H.B., D.J.C.M.t. Mannetje, and J.M. Oh, *Contact angle hysteresis: a review of fundamentals and applications.* Colloid. Polym. Sci. , 2013. **291**: p. 247-260.

13. Du, K., et al., *Adsoption energy of nano and microparticles at liquid-liquid interfaces.* Langmuir, 2010. **26**: p. 12518-12522.

14. Chan, D.Y.C., J.D. Henry, and L.R. White, *The interaction of colloidal particles collected at fluid interfaces.* J. Colloid Interface Sci. , 1981. **79**: p. 410.

15. Kralchevsky, P.A. and K. Nagayama, *Capillary forces between colloidal particles.* Langmuir, 1994. **10**: p. 23.

16. Kralchevsky, P.A., et al., *Capillary image forces: I. Theory.* J. Colloid Interface Sci., 1994. **167**: p. 47.

17. Paunov, V.N., et al., *Lateral capillary forces between floating submillimeter particles.* J. Colloid Interface Sci., 1993. **157**: p. 100.

18. Kralchevsky, P.A., N.D. Denkov, and K.D. Danov, *Particles with an undulated contact line at a fluid interface: Interaction between capillary quadrupoles and rheology of particulate monolayers.* Langmuir, 2001. **17**: p. 7694-7705.

19. Danov, K.D., et al., *Interactions between particles with an undulated contact line at a fluid interface: Capillary multipoles of arbitrary order.* Langmuir, 2005. **287**: p. 121-134.

20. Dinsmore, A.D., et al., *Self-assembled, selectively-permeable capsules composed of colloidal particles.* Science, 2002. **298**: p. 1006.

21. Aveyard, R., B.P. Binks, and J.H. Clint, *Emulsions stabilised solely by colloidal particles.* Adv. Colloid Interface Sci., 2003. **100**: p. 503.

22. Velev, O.D. and S. Gupta, *Materials fabricated by micro- and nanoparticle assembly—the challenging path from science to engineering.* Advanced Materials, 2009. **21**: p. 1897-1905.

23. Vella, D., P. Aussillous, and L. Mahadevan, *Elasticity of an interfacial particle raft.* Europhysics Letters, 2004. **68**: p. 212.

24. Aveyard, R., et al., *Structure and collapse of particle monolayers under lateral pressure at the octane/aqueous surfactant solution interface.* Langmuir, 2000. **16**: p. 8820-8828.

25. Razavi, S., et al., *Collapse of particle-laden interfaces under compression: Buckling vs particle expulsion.* Langmuir, 2015. **31**: p. 7764-7775.

26. Kassuga, T.D. and J.P. Rothstein, *Buckling of particle-laden interfaces.* J. Colloid Interface Sci., 2015. **448**: p. 287-296.

27. Planchette, C., E. Lorenceau, and A.L. Biance, *Surface wave on a particle raft.* Soft Matter, 2012. **8**: p. 2444-2451.

28. Jambon-Puillet, E., C. Josserand, and S. Protière, *Wrinkles, folds, and plasticity in granular rafts.* Phys. Rev. Materials, 2017. **1**: p. 042601(R).

29. Kleman, M. and O.D. Lavrentovich, *Soft matter physics: an introduction*. 2003: Springer.

30. Keesom, W.H., *The second viral coefficient for rigid spherical molecules, whose mutual attraction is equivalent to that of a quadruplet placed at their centre.* KNAW Proceedings, 1915. **18**: p. 636-646.

31. Steiner, T., *The Hydrogen Bond in the Solid State.* Angew. Chem. Int. Ed., 2002. **41**: p. 48-76.

32. Chandler, D., *Interfaces and the driving force of hydrophobic assembly.* Nature, 2005. **437**: p. 640.

33. Hamley, I.W., *Introduction to soft matter: polymers, colloids, amphiphiles and liquid crystals*. 2003: John Wiley & Sons Ltd.

34. Sun, J. and X.L. Zheng, *A review of oil-suspended particulate matter aggregation – a natural process of cleansing spilled oil in the aquatic environment.* J. Environ. Monit, 2009. **11**: p. 1801.

35. Katepalli, H., V.T. John, and A. Bose, *The Response of Carbon Black Stabilized Oil-in-Water Emulsions to the Addition of Surfactant Solutions.* Langmuir, 2013. **29**: p. 6790.

36. Saha, A., et al., *Oil Emulsification Using Surface-Tunable Carbon Black Particles.* ACS Appl. Mater. Interfaces, 2013. **5**: p. 3094.

37. Kruglyakov, A.F.K.a.P.M.I., *Emulsifying Effects of Solid Particles and the Energetics of Putting them at the Water – Oil Interface.* Izv. Sib. Otd. Akad. Nauk SSSR, Ser. Khim. Nauk, 1971. **2**: p. 139.

38. Chaudhuri, P., et al., *Equilibrium glassy phase in a polydisperse hard-sphere system.* Phys. Rev. Lett., 2005. **95**: p. 248301.

39. Madivala, B., et al., *Exploiting particle shape in solid stabilized emulsions.* Soft Matter, 2009. **5**: p. 1717.

40. Stocco, A., et al., *Aqueous foams stabilized solely by particles.* Soft Matter, 2011. **7**: p. 1260.

41. Chatterjee, N. and M. Flury, *Effect of Particle Shape on Capillary Forces Acting on Particles at the Air – Water Interface.* Langmuir, 2013. **29**: p. 7903.

42. Chatterjee, N., S. Lapin, and M. Flury, *Capillary Forces between Sediment Particles and an Air – Water Interface.* Environ. Sci. Technol., 2012. **46**: p. 4411.

43. Pitois, O. and X. Chateau, *Small particle at a fluid interface: effect of contact angle hysteresis on force and work of detachment.* Langmuir, 2002. **18**: p. 9751.

44. Yarnold, G.D., *The Hysteresis of the Angle of Contact of Mercury.* Proc. Phys. Soc., 1946. **58**: p. 120.

45. Scheludko, A.D. and A.D. Nikolov, *Measurement of Surface-Tension by Pulling a Sphere from a Liquid.* Colloid Polym. Sci., 1975. **253**: p. 396.

46. Huh, C. and S.G. Mason, *Sphere Tensiometry – Evaluation and Critique.* Can. J. Chem., 1976. **54**: p. 969.

47. Zhang, L., L. Ren, and S. Hartland, *More convenient and suitable methods for sphere tensiometry.* J. Colloid Interface Sci., 1996. **180**: p. 493.

48. Zhang, L., L. Ren, and S. Hartland, *Detailed analysis of determination of contact angle using sphere tensiometry.* J. Colloid Interface Sci., 1997. **192**: p. 306.

49. Preuss, M. and H.J. Butt, *Measuring the contact angle of individual colloidal particles.* J. Colloid Interface Sci., 1998. **208**: p. 468.

50. Gillies, G., M. Kappl, and H.J. Butt, *Direct measurements of particle－bubble interactions.* Adv. Colloid Interface Sci., 2005. **114**: p. 165.

51. Krumpfer, J.W. and T.J. McCarthy, *Contact angle hysteresis: a different view and a trivial recipe for low hysteresis hydrophobic surfaces.* Faraday Discuss., 2010. **146**: p. 103.

52. Rasband, W.S., *ImageJ*, in *U.S. National Institutes of Health*. 1997-2014: USA.

53. Vella, D. and L. Mahadevan, *The Cheerios Effect.* Am. J. Phys., 2005. **73**: p. 817.

54. Nicolson, M.M., *The Interaction Between Floating Particles.* Proc. Cambridge Philos. Soc., 1949. **45**: p. 288.

55. Senbil, N., et al., *Effect of interface shape on advancing and receding fluid-contact angles around spherical particles.* Soft Matter, 2015. **11**: p. 4999-5003.

56. Berton-Carabin, C.C. and K. Schroen, *Pickering Emulsions for Food Applications: Background, Trends, and Challenges*, in *Annu. Rev. Food Sci. Technol., Vol 6*, M.P. Doyle and T.R. Klaenhammer, Editors. 2015, Annual Reviews: Palo Alto. p. 263-297.

57. Bhargava, A., A.V. Francis, and A.K. Biswas, *Interfacial Studies Related to Recovery of Mineral Slimes in a Water-Hydrocarbon Liquid-Collector System.* J. Colloid Interface Sci., 1978. **64**(2): p. 214-227.

58. A. D. Dinsmore, M.F.H., M. G. Nikolaides, M. Marquez, A. R. Bausch and D. A. Weitz, *Colloidosomes: Self-Assembled, Selectively-Permeable Capsules Composed of Colloidal Particles.* Science, 2002. **298**: p. 1006.

59. Howard, B.C., *Why Did L.A. Drop 96 Million ‘Shade Balls’ Into Its Water?*, in *National Geographic*. 2015.

60. Aussillous, P. and D. Quere, *Liquid marbles.* Nature, 2001. **411**: p. 924-927.

61. Zoueshtiagh, F., M. Baudoin, and D. Guerrin, *Capillary tube wetting induced by particles: towards armoured bubbles tailoring.* Soft Matter, 2014. **10**: p. 9403.

62. Lee, G., et al., *Properites and intrinsic strength of monolayer graphene.* Science, 2008. **321**: p. 385.

63. Pelling, A.E., et al., *Local nanomechanical motion of the cell wall of saccharomyces cerevisiae.* Science, 2004. **305**: p. 1147.

64. Huang, J., et al., *Capillary wrinkling of floating thin polymer films.* Science, 2007. **317**: p. 650.

65. Davidovitch, B., et al., *Prototypical model for tensional wrinkling in thin sheets.* Proc. Natl. Acad. Sci., 2011. **108**: p. 18227.

66. Bordacs, S.A., A. and Z. Horvolgyi, *Compression of Langmuir films composed of fine particles: Collapse mechanism and wettability.* Langmuir, 2006. **22**: p. 6944-6950.

67. Xu, H., et al., *Shape and buckling transitions in solid-stabilized drops.* Langmuir, 2005. **21**: p. 10016-10020.

68. Zuo, P., J. Liu, and S. Li, *The load-bearing ability of a particle raft under the transverse compression of a slender rod.* Soft Matter, 2017. **13**: p. 2315.

69. Kumar, D., et al., *Wrapping with a splash: High-speed encapsulation with ultrathin sheets.* Science, 2018. **359**: p. 775-778.

70. Paulsen, J.D., et al., *Optimal wrapping of liquid droplets with ultrathin sheets.* Nat. Mater., 2015. **14**: p. 1206-1210.

71. Amstad, E., *Capsules made from prefabricated thin films.* Science, 2018. **359**: p. 743-743.

72. Zhuang, X., et al., *Two-dimensional soft nanomaterials: a fascinating world of materials.* Adv. Mater. , 2015. **27**: p. 403-427.

73. Ajayan, P., P. Kim, and K. Banerjee, *Two-dimensional van der Waals materials.* Phys. Today, 2016. **69**: p. 46.

74. Novoselov, K.S., et al., *Electric field effect in atomically thin carbon films.* Science, 2004. **306**: p. 666-669.

75. Gupta, A., T. Sakthivel, and S. Seal, *Recent development in 2D materials beyond graphene.* Mater. Sci. , 2015. **73**: p. 44-126.

76. Govindaraju, T. and M.B. Avinash, *Two-dimensional nanoarchitectonics: organic and hybrid materials.* Nanoscale, 2012. **4**: p. 6102.

77. Huo, C., et al., *2D materials via liquid exfoliation: a review on fabrication and applications.* Sci. Bull. , 2015. **60**: p. 1994-2008.

78. Chen, Y., A. Star, and S. Vidal, *Sweet carbon nanostructures: carbohydrate conjugates with carbon nanotubes and graphene and their applications.* Chem. Soc. Rev., 2013. **42**: p. 4532.

79. Kim, K., et al., *A role for graphene in silicon-based semiconductor devices.* Nature, 2011. **479**: p. 338.

80. Chimene, D., D.L. Alge, and A.K. Gaharwar, *Two-Dimensional Nanomaterials for Biomedical Applications: Emerging Trends and Future Prospects.* Adv. Mater., 2015. **27**: p. 7261-2926.

81. Vybornyi, M., A. Rudnev, and R. Haner, *Assembly of extra-large nanosheets by supramolecular polymerization of amphiphilic pyrene oligomers in aqueous solution.* Chem. Mater. , 2015. **27**: p. 1426-1431.

82. Shin, S., et al., *Supramolecular Switching between Flat Sheets and Helical Tubules Triggered by Coordination Interaction.* Am. Chem. Soc., 2013. **135**: p. 2156-2159.

83. Bai, W., et al., *Smart organic two-dimensional materials based on a rational combination of non-covalent interactions.* Angew. Chem. Int. Ed., 2016. **55**: p. 10707.